

Silicon Photonic Waveguide Bragg Gratings

by

Xu Wang

B.Sc., Huazhong University of Science and Technology, 2007

M.A.Sc., Huazhong University of Science and Technology, 2009

A THESIS SUBMITTED IN PARTIAL FULFILLMENT
OF THE REQUIREMENTS FOR THE DEGREE OF

Doctor of Philosophy

in

THE FACULTY OF GRADUATE AND POSTDOCTORAL
STUDIES

(Electrical and Computer Engineering)

The University Of British Columbia
(Vancouver)

December 2013

© Xu Wang, 2013

Abstract

Silicon is the most ubiquitous material in the electronics industry, and is now expected to revolutionize photonics. In just over ten years, silicon photonics has become a key technology for photonic integrated circuits. By taking advantage of silicon-on-insulator (SOI) wafers and the existing complementary metal-oxide semiconductor (CMOS) fabrication infrastructure, silicon photonic chips are now being delivered with low cost and rapidly increasing functionality.

This thesis presents the integration of a fundamental optical device - Bragg grating - into SOI waveguides. Various types of waveguides and grating structures have been investigated. All designs are fabricated using CMOS foundry services. We have also explored various applications using the fabricated devices.

From the beginning, we focused on strip waveguide uniform gratings, as these are the most simple to design and fabricate. We have studied many design variations, supported by experimental results. In parallel, we have provided insight into practical issues and challenges involved with the design, fabrication, and measurement, such as the lithography effects, thermal sensitivity, and wafer-scale nonuniformity. We then introduce phase-shifted gratings that can achieve very high quality factors and be employed in various applications. We have also demonstrated sampled gratings and the Vernier effect in strip waveguides.

To obtain narrow-band gratings, we propose the use of a rib waveguide. We also propose a multi-period grating concept by taking advantage of the multiple sidewalls of the rib waveguide, to increases the design flexibility for custom optical filters. The wafer-scale data shows that rib waveguide gratings have better performance uniformity than strip waveguide gratings, and that the wafer thickness variation is critical. Additionally, we have demonstrated very compact Bragg

gratings using a spiral rib waveguide.

Finally, we demonstrate slot waveguide Bragg gratings and resonators, which has great potential for sensing, modulation, and nonlinear optics. We have also developed a novel biosensor using a slot waveguide phase-shifted grating that has a high sensitivity, a high quality factor, a low limit of detection, and can interrogate specific biomolecular interactions.

Preface

This thesis is mostly based on the publications listed below, which resulted from collaborations with other researchers. Note that only publications directly arising from the work presented in this thesis are listed here. A complete list of publications is given in Appendix A. It should also be noted that many experimental results have been redone on a single fabrication run in order to yield more meaningful comparisons. Hence, many of the figures are original figures and do not reference the original similar figures that were previously published.

Book Chapter

1. X. Wang, W. Shi, and L. Chrostowski, “Silicon photonic Bragg gratings,” in *High-Speed Photonics Interconnects*, L. Chrostowski and K. Iniewski, Ed. CRC Press, 2013, pp. 51-85.

I wrote Page 51–66 of the book chapter, which is closely related to Chapter 2 and Chapter 3 in this thesis. W. Shi wrote the other parts of the book chapter. L. Chrostowski supervised the project and assembled and edited the manuscript.

Journal Publications

1. X. Wang, S. Grist, J. Flueckiger, N. A. F. Jaeger, and L. Chrostowski, “Silicon photonic slot waveguide Bragg gratings and resonators,” *Opt. Express*, vol. 21, no. 16, pp. 19029-19039, 2013.

I conceived the idea, conducted the device design, performed the measurements and data analysis, and wrote the manuscript. S. Grist contributed to

the conception of the idea and took the SEM images. J. Flueckiger assisted with the measurements. L. Chrostowski and N. A. F. Jaeger supervised the project. All authors commented on the manuscript.

Location: Chapter 4.

2. X. Wang, J. Flueckiger, S. Schmidt, S. Grist, S. T. Fard, J. Kirk, M. Doerfler, K. C. Cheung, D. M. Ratner, and L. Chrostowski, “A silicon photonic biosensor using phase-shifted Bragg gratings in slot waveguide,” *J. Biophotonics*, vol. 6, no. 10, pp. 821-828, 2013.

I conceived the idea, conducted the device design, and wrote the manuscript. J. Flueckiger and S. Schmidt coordinated the project. S. Grist contributed to the conception of the idea and took the SEM images. S. T. Fard helped with the data analysis. S. Schmidt, J. Flueckiger, S. Grist, J. Kirk, and M. Doerfler performed the measurements and contributed to the data analysis. K. C. Cheung, D. M. Ratner, and L. Chrostowski supervised the project. All authors commented on the manuscript.

Location: Section 4.4.

3. X. Wang, W. Shi, H. Yun, S. Grist, N. A. F. Jaeger, and L. Chrostowski, “Narrow-band waveguide Bragg gratings on SOI wafers with CMOS compatible fabrication process,” *Optics Express*, vol. 20, no. 14, pp. 15547-15558, 2012.

I conceived the idea, conducted the device design, performed the measurements and data analysis, and wrote the manuscript. W. Shi contributed to the conception of the idea. H. Yun assisted with the measurements. S. Grist took the SEM images. L. Chrostowski and N. A. F. Jaeger supervised the project. All authors commented on the manuscript.

Location: Chapter 2 and Chapter 3.

4. X. Wang, W. Shi, R. Vafaei, N. A. F. Jaeger, and L. Chrostowski, “Uniform and sampled Bragg gratings in SOI strip waveguides with sidewall corrugations,” *IEEE Photonics Technology Letters*, vol. 23, no. 5, pp. 290-292, 2011.

I conceived the idea, conducted the device design, performed the measurements, and wrote the manuscript. W. Shi and L. Chrostowski contributed to the device design. R. Vafaei assisted with the measurements. L. Chrostowski and N. A. F. Jaeger gave many advices during the course of the project and assisted in editing the manuscript. This work was done as the course project for EECE 571U.

Location: Chapter 2.

Conference Proceedings

1. X. Wang, H. Yun, N. A. F. Jaeger, and L. Chrostowski, “Multi-period Bragg gratings in silicon waveguides,” in *IEEE Photonics Conference 2013*, Bellevue, WA, September 2013, paper WD2.5.

N. A. F. Jaeger and I conceived the idea. I conducted the device design, performed the measurements, and wrote the manuscript. H. Yun assisted with the measurements. N. A. F. Jaeger and L. Chrostowski supervised the project. All authors commented on the manuscript.

Location: Section 3.3.1.

2. X. Wang, H. Yun, and L. Chrostowski, “Integrated Bragg gratings in spiral waveguides,” in *CLEO 2013*, San Jose, CA, June 2013, paper CTh4F.8.

I conceived the idea, conducted the device design, and wrote the manuscript. H. Yun performed the measurements. L. Chrostowski supervised the project. All authors commented on the manuscript.

Location: Section 3.6.

3. S. T. Fard, S. M. Grist, V. Donzella, S. A. Schmidt, J. Flueckiger, X. Wang, W. Shi, A. Millspaugh, M. Webb, D. M. Ratner, K. C. Cheung, and L. Chrostowski, “Label-free silicon photonic biosensors for use in clinical diagnostics,” in *SPIE Photonics West*, San Francisco, CA, February 2013, paper 862909.

I conducted the design of the grating device and wrote the corresponding section in the manuscript. S. T. Fard led the writing of the whole manuscript.

S. M. Grist, V. Donzella, S. A. Schmidt, J. Flueckiger, W. Shi, A. Millspaugh, and M. Webb contributed to the design, measurements, and data analysis during the course of the project. D. M. Ratner, K. C. Cheung, and L. Chrostowski supervised the project. All authors commented on the manuscript.

Location: Section 2.6.3.

4. X. Wang, W. Shi, M. Hochberg, K. Adams, E. Schelew, J. Young, N. Jaeger, and L. Chrostowski, "Lithography simulation for the fabrication of silicon photonic devices with deep-ultraviolet lithography," in *Group IV Photonics*, San Diego, CA, August 2012, pp. 288-290.

I conceived the idea, conducted the design, measurements and numerical simulations, and wrote the manuscript. W. Shi, M. Hochberg, and K. Adams contributed to the project through discussions. E. Schelew assisted with the numerical simulations. J. Young, N. Jaeger, and L. Chrostowski supervised the project. All authors commented on the manuscript.

Location: Section 2.3.

5. X. Wang, W. Shi, S. Grist, H. Yun, N. A. F. Jaeger, and L. Chrostowski, "Narrow-band transmission filter using phase-shifted Bragg gratings in SOI waveguide," in *IEEE Photonics Conference*, Arlington, VA, October 2011, pp. 869-870.

I conceived the idea, conducted the device design, performed the measurements, and wrote the manuscript. W. Shi contributed to the project through discussions. S. Grist took the SEM images. H. Yun assisted with the measurements. N. A. F. Jaeger, and L. Chrostowski supervised the project. All authors commented on the manuscript.

Location: Section 2.6.2.

Table of Contents

Abstract	ii
Preface	iv
Table of Contents	viii
List of Tables	xi
List of Figures	xii
List of Abbreviations	xxv
Acknowledgments	xxvii
1 Introduction	1
1.1 Silicon Photonics	1
1.1.1 Motivation and Application	1
1.1.2 State of the Art and Challenges	4
1.2 Bragg Gratings	8
1.3 Silicon Photonic Bragg Gratings	12
1.3.1 Objectives	13
1.3.2 Thesis Organization	15
2 Strip Waveguide Bragg Gratings	16
2.1 Strip Waveguide	16
2.2 Uniform Gratings	20

2.2.1	Design	20
2.2.2	Layout	22
2.2.3	Fabrication	24
2.2.4	Measurement	25
2.2.5	Design Variations	35
2.3	Lithography Effects	46
2.4	Thermal Sensitivity	51
2.5	Wafer-Scale Performance	52
2.6	Phase-shifted Gratings	58
2.6.1	Basics	58
2.6.2	Design Variations	62
2.6.3	Applications	70
2.7	Sampled Gratings	73
2.8	Summary	77
3	Rib Waveguide Bragg Gratings	78
3.1	Rib Waveguide	79
3.2	Uniform Gratings	80
3.2.1	Design and Fabrication	80
3.2.2	Measurement Results	82
3.3	Multi-period Gratings	86
3.3.1	Dual-Period Grating	86
3.3.2	Four-Period Grating	87
3.4	Thermal Sensitivity	90
3.5	Wafer-Scale Performance	92
3.6	Spiral Gratings	99
3.6.1	Design	100
3.6.2	Results and Discussion	103
3.7	Summary	105
4	Slot Waveguide Bragg Gratings	106
4.1	Slot Waveguide	107
4.2	Uniform Gratings	109

4.2.1	Design and Fabrication	109
4.2.2	Measurement Results	112
4.3	Phase-Shifted Gratings	114
4.3.1	Design and Fabrication	114
4.3.2	Measurement Results	116
4.4	Biosensing Applications	118
4.4.1	Silicon Photonic Biosensors	119
4.4.2	Design and Fabrication	121
4.4.3	Experiments and Discussion	122
4.5	Summary	128
5	Conclusion and Future Work	129
5.1	Conclusion	129
5.2	Future Work	132
Bibliography	135	
A Publications	150	
A.1	Book Chapters	150
A.2	Journal Publications	150
A.3	Conference Proceedings	152

List of Tables

Table 2.1	Maximum output power (continuous power during sweep) of Agilent 81600B Option 201 [1].	34
Table 3.1	Statistics of strip and rib waveguide Bragg gratings (WBG). . .	99
Table 3.2	Mode mismatch loss between two bent waveguides (WG). . . .	103
Table 4.1	Design variations for uniform slot waveguide Bragg gratings. .	109

List of Figures

Figure 1.1	Common waveguide geometries in silicon-on-insulator.	4
Figure 1.2	Longitudinal effective index profile of a uniform grating (z is the propagation direction, Λ is the grating period, n_{eff1} is the low effective refractive index and n_{eff2} is the high effective refractive index).	8
Figure 1.3	Typical spectral responses of a uniform Bragg grating.	9
Figure 1.4	A typical silicon photonic chip and a Canadian dime.	14
Figure 2.1	Schematic of a strip waveguide cross section (not to scale). . .	17
Figure 2.2	Simulated electric field of the fundamental modes in 500 nm strip waveguides: (a) TE mode with air cladding, (b) TM mode with air cladding, (c) TE mode with oxide cladding, and (d) TM mode with oxide cladding.	18
Figure 2.3	SEM image of a 500 nm strip waveguide. The waveguide was milled using a focused ion beam (FIB) to expose the cross section.	19
Figure 2.4	Schematic of a uniform strip waveguide grating.	20

Figure 2.5	Typical design flow for a uniform Bragg grating: 1) choose a certain waveguide cross section, 2) calculate the mode profile and effective refractive index, then calculate the grating period based on the Bragg condition, 3) calculate the coupling coefficient for a particular bandwidth (assuming the grating is sufficiently long and a high reflectivity is needed), 4) calculate the corrugation width with the assistance of mode simulation and lithography simulation, 5) calculate the grating length.	21
Figure 2.6	Simulated electric field of the second TE mode in a 500 nm strip waveguide with oxide cladding. The majority of the electric field is on the sidewalls, resulting in a much lower effective index and a much higher propagation loss than the fundamental TE mode.	21
Figure 2.7	Schematic diagram of the device layout (not to scale): (a) individual fiber configuration, (b) fiber array configuration.	24
Figure 2.8	An approach to increase the device packing efficiency using the fiber array configuration. The grating devices are located in the bundle on the right side, and the routing waveguides run between the grating couplers.	25
Figure 2.9	Top view SEM image of a fabricated strip waveguide grating with design parameters: $W = 500$ nm, $\Delta W = 80$ nm. Note that the rectangular corrugations we used in the design were rounded due to the lithography.	26
Figure 2.10	Tilted view SEM image of a fabricated Y-branch as illustrated in Figure 2.7(a).	26
Figure 2.11	Top view SEM image of a fabricated grating coupler (GC). The layout of the GC was illustrated in Figure 2.8, and the square tiles were added around the GC to meet the density rule.	27
Figure 2.12	Part of a fabricated chip showing the compact routing approach illustrated in Figure 2.8.	27
Figure 2.13	A measurement setup using two individual fibers.	28

Figure 2.14	Block diagram of the advanced experimental setup. PD: photodetector, EDFA: erbium-doped fiber amplifier, TEC: thermoelectric cooler.	29
Figure 2.15	An advanced measurement setup using a fiber array.	30
Figure 2.16	Full view of the advanced measurement setup.	31
Figure 2.17	Captured image during experiment. The chip uses a layout similar to Figure 2.8, and the grating couplers are aligned with the fibers in the array.	32
Figure 2.18	Measured transmission spectra of a straight waveguide (WG) and a Bragg grating using: (a) the low SSE option, and (b) the high power option. Comparison between the low SSE option and the high power option for: (c) the spectra of the straight waveguide, and (d) the normalized response of the grating by subtracting the spectra of the straight waveguide . Note that the laser output power was set to be 0 dBm (i.e., 1 mW).	33
Figure 2.19	Measured transmission spectra of a Bragg grating using the high power option under various sweeping conditions. Inset shows the zoom-in view around the Bragg wavelength. The small ripples out of the stop band are due to the FP effects in the measurement system.	35
Figure 2.20	Measured transmission spectra for gratings with different grating periods, showing the red shift with increasing grating period. Fixed parameters: air cladding, $W = 500$ nm, $\Delta W = 20$ nm, $N = 1000$	36
Figure 2.21	Bragg wavelength extracted from Figure 2.20 versus grating period. The slope of the linear curve fit is 2.53, which is in good agreement with the calculation using Eq. 2.1.	37
Figure 2.22	Measured transmission spectra for various corrugation widths, showing the bandwidth increases with increasing corrugation width. Fixed parameters: air cladding, $W = 500$ nm, $\Lambda = 325$ nm, and $N = 3000$	38

Figure 2.23	Measured bandwidth versus corrugation widths on 500 nm strip waveguide with air cladding. The data points for 10 nm, 40 nm, 80 nm, and 160 nm corrugations correspond to the spectra in Figure 2.22. The linear fit shows that the coupling coefficient (i.e., grating index contrast) is approximately proportional to the corrugation width.	38
Figure 2.24	Measured transmission spectra for gratings with 20 nm corrugation on a 500 nm waveguide and on a 450 nm waveguide. Fixed parameters: air cladding, $\Delta W = 20$ nm and $N = 1000$. The period for the 500 nm waveguide and the 450 nm waveguide is 325 nm and 340 nm, respectively.	39
Figure 2.25	Simulated electric field of the fundamental TE mode in a 500 nm (top) and a 450 nm (bottom) strip waveguide, both with air cladding. The field intensity around the sidewall of the 450 nm waveguide is stronger than that of the 500 nm waveguide.	40
Figure 2.26	Measured bandwidth as a function of corrugation width on 500 nm (blue) and 450 nm (red) strip waveguides with air cladding. The gratings on narrower waveguide show larger bandwidths and a larger slope in the linear fit, due to increased modal overlap with the sidewalls.	40
Figure 2.27	Measured transmission spectra for gratings with air cladding (blue) and with oxide cladding (green). For the oxide-clad device, the wavelength is longer due to the larger average effective index and the bandwidth is smaller due to the reduced index contrast. Fixed parameters: $W=500$ nm, $\Delta W=160$ nm, $\Lambda=325$ nm, $N=3000$	41
Figure 2.28	Measured bandwidth as a function of corrugation width on 500 nm strip waveguide with air cladding (blue) and with oxide cladding (green). The gratings with oxide cladding show smaller bandwidths and a smaller slope in the linear fit, due to the reduced index contrast.	41

Figure 2.29	Measured out-of-band transmission spectra for gratings with various corrugation widths and lengths. Fixed parameters: air cladding, $W = 500$ nm, $\Lambda = 325$ nm. The propagation loss is within the range of 2.5–4.5 dB/cm and is independent of the corrugation width.	42
Figure 2.30	Measured transmission spectra of gratings with 20 nm corrugation width for various lengths, showing bandwidth broadening effect with increasing N and wavelength variations due to fabrication variations. Fixed parameters: air cladding, $W = 500$ nm, $\Lambda = 325$ nm.	43
Figure 2.31	Measured transmission spectra of gratings with (a) 10 nm and (b) 80 nm corrugation width for various lengths, showing similar trends as Figure 2.30. Fixed parameters: air cladding, $W = 500$ nm, $\Lambda = 325$ nm.	44
Figure 2.32	Schematic illustration of corrugation shapes (not to scale). . .	45
Figure 2.33	Measured bandwidth as a function of corrugation width for different shapes. Fixed parameters: oxide cladding, $W = 500$ nm, $\Lambda = 320$ nm, $N = 2000$. The bandwidth and the slope of the linear fit become smaller as the shape goes from rectangular to trapezoidal to triangular, due to the reduced Fourier component and coupling coefficient.	46
Figure 2.34	Lithography simulation for device A: (a) original design, (b) simulation result.	48
Figure 2.35	Spectral comparison (transmission) for device A. Original design: FDTD simulation using the structure in Figure 2.34(a), post-litho simulation: FDTD simulation using the structure in Figure 2.34(b).	48
Figure 2.36	Bandwidth versus corrugation width on 500 nm strip waveguides with air cladding. The post-litho simulation agrees well with the measurement result, while the original designs show bandwidths of about three times larger.	49

Figure 2.37	Lithography simulation for a photonic crystal cavity with three missing holes in the centre. XOR: Boolean operation of XOR (exclusive or) between the original and simulated layouts. The two cavity side holes (H1 and H2) are displaced in order to achieve a high Q-factor.	50
Figure 2.38	Measured transmission spectra of a strip waveguide grating at different temperatures, showing the red shift with increasing temperature. The design parameters are: air cladding, $W = 500$ nm, $\Delta W = 20$ nm, $\Lambda = 330$ nm, and $N = 1000$	51
Figure 2.39	Bragg wavelength versus temperature corresponding to the measured spectra in Figure 2.38, showing a thermal sensitivity of about 84 pm/ $^{\circ}\text{C}$	52
Figure 2.40	Wafer map (available chips are listed in the legend).	54
Figure 2.41	Performance nonuniformity of the strip waveguide grating on Wafer A.	55
Figure 2.42	Performance nonuniformity of the strip waveguide grating on Wafer B.	56
Figure 2.43	Performance nonuniformity of the strip waveguide grating as a function of the column number. Each error bar is symmetric and the length is two standard deviations (within each column). The general trend of the decrease in wavelength and the increase in bandwidth is due to the intentional increase in exposure dose from left to right columns.	57
Figure 2.44	Schematic of a phase-shifted strip waveguide grating.	58
Figure 2.45	Spectral responses of a uniform and a phase-shifted grating. Note that the only difference between the two devices is the inclusion of the phase shift.	59
Figure 2.46	Top view SEM image of a fabricated strip waveguide phase-shifted grating. Design parameters: $W = 500$ nm, $\Delta W = 80$ nm, $\Lambda = 320$ nm. Note that the phase shift in the central region can be identified by measuring the spacing between the grating grooves. Here, the spacing with the phase shift is 480 nm, corresponding to 1.5 times the grating period (320 nm).	60

Figure 2.47	Transmission spectra for phase-shifted gratings with different phase-shift length. Multiple resonance peaks occur for long cavity length due to the reduced free spectral range.	61
Figure 2.48	Transmission spectra for phase-shifted gratings with different N . Fixed parameters: oxide cladding, $W = 500$ nm, $\Delta W = 60$ nm, $\Lambda = 320$ nm. As N is increased, the stop band becomes deeper due to the increasing reflectivity, and the resonant peak becomes sharper due to the reduced coupling loss and higher Q factor.	63
Figure 2.49	Transmission spectra for phase-shifted gratings with different ΔW . Fixed parameters: oxide cladding, $W = 500$ nm, $N = 200$, $\Lambda = 320$ nm. As ΔW is increased, the stop band becomes wider and deeper due to the increasing coupling coefficient, and the resonant peak becomes sharper due to the reduced coupling loss and higher Q factor.	63
Figure 2.50	Contour plot of the Q factor as a function of ΔW and N . Fixed parameters: oxide cladding, $W = 500$ nm, $\Lambda = 320$ nm. The Q factor increases towards the top-right corner of the contour, i.e., large N and/or ΔW (essentially a high mirror reflectivity).	64
Figure 2.51	Measured Q factor as a function of (a) ΔW (corresponding to the top boundary of the contour plot in Figure 2.50) and (b) N (corresponding to the right boundary of the contour plot in Figure 2.50).	65
Figure 2.52	Transmission spectra (unnormalized) for phase-shifted gratings with different N . Fixed parameters: air cladding, $W = 500$ nm, $\Delta W = 60$ nm, and $\Lambda = 330$ nm. The peak amplitude drops significantly after $N=200$, as it goes beyond the critical coupling condition.	66
Figure 2.53	Maximum transmission and Q factor of an FP cavity as a function of R . Simulation parameters: $\alpha = 3$ dB/cm, $L = 100 \mu\text{m}$, $G = 0.9931$. The maximum transmission decreases dramatically after the critical coupling condition, when the coupling loss equals the waveguide loss: $R=\sqrt{G}=0.9965$	67

Figure 2.54 Maximum Q factor experimentally observed. Design parameters: air cladding, $W = 500$ nm, $\Delta W = 40$ nm, $N = 300$, and $\Lambda = 330$ nm.	67
Figure 2.55 Measured transmission spectra (raw) of a high-Q phase-shifted grating at various input power levels. At 0 dBm input power, the resonance becomes asymmetric and the peak wavelength is skewed to the right.	68
Figure 2.56 Measurement setup for biosensing. Reagents were introduced to the sensor using a reversibly bonded PDMS flow cell and Chemyx Nexus 3000 Syringe Pump at 10 $\mu\text{L}/\text{min}$. Note that the input/output grating couplers are placed far away from the sensor on the chip.	71
Figure 2.57 Top: transmission spectra for various concentrations of NaCl (note: 1 M=1 mol/L=1000 mol/m ³). Bottom: peak wavelength shift versus bulk refractive index, showing a sensitivity of 58.52 nm/RIU.	72
Figure 2.58 Schematic of a sampled grating.	73
Figure 2.59 Measured transmission and reflection spectra of two sampled gratings. Design parameters: air cladding, $W = 500$ nm, $\Delta W = 20$ nm, $Z_1 = 6.4 \mu\text{m}$. Each device includes 20 sampling periods (i.e., total length is 20 Z_0). The peak spacing for $Z_0/Z_1 = 4$ is 1.5 times larger than that for $Z_0/Z_1 = 6$, in agreement with Eq. 2.17.	74
Figure 2.60 Layout for the Vernier effect using two sampled gratings with slightly mismatched sampling periods.	75
Figure 2.61 Measured reflection spectra of two individual sampled gratings (top) and the Vernier effect (bottom). The only major peak for the Vernier effect occurs where the peaks of individual sampled gratings are well aligned (at 1530 nm).	76
Figure 3.1 Schematic of the rib waveguide cross section (not to scale): $W_{rib} = 500$ nm, and $W_{slab} = 1 \mu\text{m}$	79

Figure 3.2	Simulated electric field of the fundamental TE mode in the rib waveguide with air cladding. The field intensity is low around the sidewalls, allowing for weak perturbations to the mode using relatively large sidewall corrugations.	80
Figure 3.3	Cross-sectional SEM image of a rib waveguide with gratings on the slab.	81
Figure 3.4	Top view SEM images of fabricated rib waveguide gratings designed with 60 nm corrugations on the rib (left) and 80 nm corrugations on the slab (right).	82
Figure 3.5	Top view SEM image of the transition from the strip waveguide to the rib waveguide grating using a linear taper.	82
Figure 3.6	Measured transmission responses of two rib waveguide gratings with corrugations on the slab, each showing only one dip in a wide wavelength range without higher-order leaky modes.	83
Figure 3.7	Zoomed-in view of Figure 3.6 around the Bragg wavelength. The dots are the measured values, and the solid curves are the fits using the analytical expression in Eq. 1.9. As expected, the grating with larger corrugations shows a slightly larger bandwidth and a higher reflectivity.	84
Figure 3.8	Extracted coupling coefficient versus designed corrugation width for various grating structures on a chip with oxide cladding. The strip waveguide is 500 nm wide and has the largest coupling coefficient, while the grating-on-slab configuration has the smallest coupling coefficient.	85
Figure 3.9	Schematic diagram of a dual-period rib waveguide grating (not to scale). Design parameters: $\Lambda_1 = 290$ nm, $\Lambda_2 = 295$ nm, $\Delta W_{rib} = 80$ nm, $\Delta W_{slab} = 100$ nm, and the grating length is 580 μ m.	87
Figure 3.10	(a) Measured (unnormalized) transmission spectrum of the dual-period grating: λ_1 and λ_2 correspond to Λ_1 and Λ_2 , respectively. (b) Normalized response around the two Bragg wavelengths.	88

Figure 3.11 Dual-period grating: simulation vs. measurement. In the top graph, the solid blue curve shows the simulated effective index of the fundamental TE mode; the green and red dashed curves corresponds to the effective indices that are needed using Λ_1 and Λ_2 , respectively; thus, the intersection points correspond to the two Bragg wavelengths.	89
Figure 3.12 Schematic diagram of the 4-period rib waveguide grating (not to scale). Design parameters: $\Lambda_1 = 285$ nm, $\Lambda_2 = 290$ nm, $\Lambda_3 = 295$ nm, $\Lambda_4 = 300$ nm, $\Delta W_{rib} = 80$ nm, $\Delta W_{slab} = 100$ nm, and the grating length is 580 μ m.	89
Figure 3.13 Measured spectral responses of a 4-period grating. λ_1 , λ_2 , λ_3 , and λ_4 correspond to Λ_1 , Λ_2 , Λ_3 , and Λ_4 , respectively.	90
Figure 3.14 Bragg wavelength shift of a dual-period rib waveguide grating at different temperatures: (a) plot around λ_2 , (b) plot around λ_1	91
Figure 3.15 Bragg wavelengths versus temperature corresponding to the spectra in Figure 3.14, showing thermal sensitivities of about 85 pm/ $^{\circ}$ C.	92
Figure 3.16 Wavelength nonuniformity of the dual-period grating on Wafer A.	94
Figure 3.17 Bandwidth nonuniformity of the dual-period grating on Wafer A.	95
Figure 3.18 Wavelength nonuniformity of the dual-period grating on Wafer B.	96
Figure 3.19 Bandwidth nonuniformity of the dual-period grating on Wafer B.	97
Figure 3.20 Performance nonuniformity of the dual-period grating as a function the column number. Each error bar is symmetric and the length is two standard deviations (within each column). All variations are random except the bandwidth variations for $\Delta\lambda_2$, which show that the bandwidth increases from left to right columns due to the intentional exposure dose variation.	98
Figure 3.21 Top view of the spiral grating design.	100

Figure 3.22	Optical microscope images of the fabricated device with $N=10$. (a) Whole layout. (b) Enlarged image of center region of the spiral.	101
Figure 3.23	Effective index change of the rib waveguide versus bending radius for device with $N_R=10$. The index change from $R = 10 \mu\text{m}$ to $R = 22.5 \mu\text{m}$ is remarkable, while for R larger than $22.5 \mu\text{m}$, the index change is very small.	102
Figure 3.24	SEM image of the fabricated spiral gratings.	103
Figure 3.25	(a) Measured transmission spectra of the two spiral gratings. (b) Enlarged plot around the Bragg wavelength.	104
Figure 4.1	Schematic of a slot waveguide cross section (not to scale).	107
Figure 4.2	Simulated electric field of the fundamental TE mode in a slot waveguide with the following design parameters: oxide cladding, $W_{arm} = 270 \text{ nm}$, and $W_{slot} = 150 \text{ nm}$. The field intensity is strongly confined inside the slot region.	108
Figure 4.3	SEM image of the focused ion beam (FIB) milled cross section of a fabricated device (the small hole in the centre was due to the incomplete coating of platinum deposited to protect the waveguides during the FIB milling). Design parameters: $W_{arm} = 270 \text{ nm}$, and $W_{slot} = 150 \text{ nm}$	108
Figure 4.4	Schematic diagrams (not to scale) of the slot waveguide Bragg gratings with corrugations (a) inside and (b) outside.	109
Figure 4.5	Top view SEM images of the fabricated slot waveguide Bragg gratings: (a) corrugation inside for $W_{slot} = 150 \text{ nm}$, $W_{arm} = 270 \text{ nm}$, and $\Delta W_{in} = 20 \text{ nm}$. (b) corrugations outside for $W_{slot} = 150 \text{ nm}$, $W_{arm} = 270 \text{ nm}$, and $\Delta W_{out} = 40 \text{ nm}$	110
Figure 4.6	Schematic of the strip-to-slot mode converter (not to scale).	111
Figure 4.7	SEM image of a strip-to-slot mode converter as illustrated in Figure 4.6.	111
Figure 4.8	Measured raw spectra of a uniform grating designed on WG1 with $\Delta W_{out} = 10 \text{ nm}$, showing a deep notch with an extinction ratio greater than 40 dB at about 1550 nm.	112

Figure 4.9	Measured transmission spectra of the uniform gratings designed on WG1. (a) corrugations inside, (b) corrugations outside. For both configurations, the stop-band becomes broader with increasing corrugation width.	113
Figure 4.10	Measured bandwidth versus designed corrugation width on WG1 and WG2. WG1 with inside corrugations shows the largest bandwidth due to the strongest perturbation.	113
Figure 4.11	Phase-shifted Bragg gratings with corrugations on the outside of the slot waveguide: (a) schematic diagram (not to scale), (b) SEM image showing the phase shift region of a fabricated device, (c) transmission spectrum simulated by FDTD with the following geometric parameters: WG1, $\Delta W_{out} = 40$ nm, and $N = 50$	115
Figure 4.12	Electric field distributions for light incident from the left at (a) 1543 nm and (b) 1550 nm. The simulation parameters are the same as in Figure 4.11(c). The field was recorded at the middle of the silicon waveguide in the vertical direction (i.e., corresponding to the plane of $y=110$ nm in Figure 4.2).	116
Figure 4.13	Measured raw spectra of a phase-shifted grating designed on WG1 with $\Delta W_{out} = 40$ nm and $N = 300$	117
Figure 4.14	(a) Measured transmission spectra for phase-shifted gratings designed on WG1 with $\Delta W_{out} = 40$ nm and various lengths, (b) Q factor as a function of N	117
Figure 4.15	Schematic diagram of the sensor integrated with the microfluidic channel.	121
Figure 4.16	SEM image of the fabricated device. Note that the phase shift in the central region can be identified by measuring the spacing between the grating grooves. Here, the spacing with the phase shift is 660 nm, corresponding to 1.5 times the grating period.	122
Figure 4.17	Measured transmission spectrum of the sensor immersed in deionized water.	123

Figure 4.18 Measurement results for various NaCl concentrations: (a) transmission spectra for all the measurements, (b) peak wavelength shift during the salt steps. Each color represents a NaCl concentration. Steps 1 and 6 correspond to 0 mM, and Steps 2 to 5 correspond to 62.5 mM, 125 mM, 250 mM, and 500 mM solutions, respectively.	124
Figure 4.19 Measured and simulated peak wavelength shift as a function of the refractive index of the salt solution. For the experimental data, the symmetric error bars are two standard deviation units in length.	125
Figure 4.20 Biosensing experimental results: (a) depicts the resonance wavelength shifts as the experiment progressed while (b) illustrates reagent sequencing corresponding to regions [A-E] in (a). Reagent A = Protein-A (1 mg/mL), B = anti-streptavidin (SA) (125 µg/mL), C = Bovine Serum Albumen (BSA) (2 mg/mL), D = streptavidin (SA) (1.8 µM), E = Biotin-BSA (2.5 mg/mL). Introduction of reagent in each region was followed by a PBS-wash, as shown by the short, black-dashed line mid-way through each region.	126
Figure 5.1 A proposed active grating device – high-speed modulator based on a p-n junction: (a) mask layout and (b) schematic of the cross section of the p-n junction.	134

List of Abbreviations

CMOS	Complementary Metal-Oxide-Semiconductor
DBR	Distributed Bragg Reflector
DFB	Distributed Feedback Laser
DRC	Design Rule Checker
DUV	Deep Ultraviolet
EDA	Electronic Design Automation
EDFA	Erbium-Doped Fiber Amplifier
FBG	Fiber Bragg Grating
FCA	Free-Carrier Absorption
FCD	Free-Carrier Dispersion
FDTD	Finite-Difference Time-Domain
FIB	Focused Ion Beam
FP	Fabry-Perot
FSR	Free Spectral Range
FWHM	Full Width at Half Maximum
GaAs	Gallium Arsenide
GC	Grating Coupler
Ge	Germanium
ICP	Inductively Coupled Plasma
InP	Indium Phosphide
LiNbO_3	Lithium Niobate
LOD	Limit of Detection
MPW	Multi-Project Wafer
MZI	Mach-Zehnder Interferometer

NA	Numerical Aperture
OSA	Optical Spectrum Analyzer
PD	Photodetector
PDMS	Polydimethylsiloxane
PDK	Process Design Kit
RIE	Reactive-Ion Etching
RIU	Refractive Index Unit
SDL	Schematic Driven Layout
SEM	Scanning Electron Beam
Si	Silicon
SiO ₂	Silicon Oxide
SOI	Silicon-on-Insulator
SSE	Source Spontaneous Emission
TE	Transverse Electric
TM	Transverse Magnetic
TPA	Two-Photon Absorption
UV	Ultraviolet
WDM	Wavelength Division Multiplexing

Acknowledgments

To begin with, I am deeply grateful to my supervisor Prof. Lukas Chrostowski, who has been a tremendous source of support and guidance over the past few years. I have truly enjoyed working with Lukas and appreciated the opportunities that were made possible by him. His passion and diligence have been an important influence on me. This thesis would also not have been possible without Prof. Nicolas A. F. Jaeger, who has been an unofficial co-supervisor and in whose lab most of my experiments were performed. I also thank Prof. Shahriar Mirabbasi for serving on my supervisory committee and for his helpful comments on my work.

I would like to thank many students (including former students) in our research group: Wei Shi, Behnam Faraji, Raha Vafaei, Jonas Flueckiger, Samantha Grist, Han Yun, Charlie Lin, Yun Wang, Michael Caverley, Miguel A. Guillen-Torres, Robert Boeck, and Sahba T. Fard. They contributed to this work in various ways over the years and also made my time in the lab a lot of fun. I enjoyed the countless hours of brainstorming and discussion, and fixing every little problem just got much easier with their help. Our visiting students, Gwen Yu and Mengyu Weng, who collected lots of data for this thesis, certainly deserve my thanks. I also want to thank Yiheng Lin for helping me take good pictures using the microscope in Prof. Guangrui Xia's lab.

I gratefully acknowledge the NSERC Si-EPIC program for the financial support and training in the past two years. I also acknowledge CMC Microsystems for enabling the fabrication of most of our chips and for organizing the Canada-wide silicon photonics workshops. In particular, I want to thank Dr. Dan Deptuck and Dr. Jessica Zhang for their assistance. I would like to thank Lumerical Solutions and Mentor Graphics for their software and excellent technical support, as well as

our collaborations. My special thanks would go to the foundries where our devices were actually fabricated: IMEC (Belgium), IME (Singapore), and BAE (United States), and to the two major MPW service providers: ePIXfab and OpSIS.

One of the wonderful things about my PhD has been collaborating with many researchers in other fields. These include bioengineers at the University of Washington (particularly Shon Schmidt and Prof. Daniel M. Ratner); and microwave photonic experts at INRS (particularly Dr. Maurizio Burla and Prof. Jose Azana) and Chinese Academy of Sciences (Prof. Ming Li). Our collaborations have been very exciting and productive, and I greatly appreciate their efforts and help. I also enjoyed the fruitful discussions with the nanophotonics group at the University of Delaware led by Prof. Michael Hochberg.

It is a pleasure to recall my internship at TeraXion, which not only gave me valuable industrial experience but also allowed me to know Quebec City. In particular, I would like to thank Dr. Yves Painchaud and Dr. Michel Poulin for their help throughout the course of the internship.

Finally, to acknowledge debts that have accumulated over years, I thank my family, for their love, understanding, and endless support.

Chapter 1

Introduction

Silicon photonics has great potential to bring together two technological areas that have transformed the last century – electronics and photonics, and is gaining tremendous momentum in both academia and industry. The Bragg grating is a fundamental component in various optical devices and has applications in areas as diverse as communications, lasers, and sensors. In this thesis, we will present the integration of Bragg gratings in silicon photonic waveguides, using a wide variety of waveguide geometries and grating profiles, and explore their applications.

1.1 Silicon Photonics

Silicon photonics is currently one of the most active disciplines within the field of optics and photonics [2–4]. Over the past decade, the silicon photonics community has made spectacular progress in developing a wide variety of photonic devices on silicon. Recently, the move to commercial products, as well as large-scale system integration, has just begun. In this section, we will briefly discuss the motivations and applications for silicon photonics, and then give a short overview of the state of the art and some challenges in this area.

1.1.1 Motivation and Application

Integration is a major driving force behind today’s rapid development of silicon photonics. It allows photonic devices to be made cheaply and in large quantities

using standard semiconductor fabrication techniques, and offers the possibility of integration with electronic circuits to provide increased functionality. It is well known that silicon wafers have the lowest cost (per unit area) and the highest crystal quality of any semiconductor materials [3]. In the mature microelectronics industry, it is able to fabricate millions of transistors in a single integrated circuit (IC), and offer them at such a low price that they have become ubiquitous in our daily lives. There is no doubt that, the integration of a large number of photonic functions onto a single chip can bring similar advantages to photonics as what silicon integration has done for electronics: compactness, dramatic cost reductions, enhanced performance, large-scale system with increased functionality, etc. But then the question is: which material or platform is appropriate for such integration? Silicon is definitely the most successful material for electronics, but is it a good choice for photonics?

Currently, the photonics market is shared by several material systems, including compound semiconductors such as indium phosphide (InP) and gallium arsenide (GaAs), elementary semiconductors such as silicon (Si) and germanium (Ge), silica and rare-earth-doped glasses, lithium niobate (LiNbO_3), and polymers [5]. Each material is selected for particular applications and devices. On the system level, it is common to find more than one of these materials used in different components. A typical example is the optical fiber communication system, where almost all of the above materials are used (e.g., InP for lasers, silica for fibres, LiNbO_3 for modulators, erbium-doped glass for optical amplifiers, Si for control circuits made with CMOS, InGaAs/Ge for detectors, etc). This makes the device manufacturing industry fragmented, and more importantly, the discrete photonic components are packaged separately, which eventually results in very high packaging cost, low yield, and large size of the final product.

Silicon is optically transparent at key wavelengths (1310 nm and 1550 nm) used for telecommunications, so it could be used to create waveguides and other passive devices. An ideal platform for creating waveguides is silicon-on-insulator (SOI), which consists of a top (active) silicon layer supported by a buried oxide layer with a bottom silicon substrate. The strong optical confinement offered by the high refractive index contrast between Si ($n = 3.48$) and air ($n = 1$) or SiO_2 ($n = 1.44$) makes it possible to shrink the waveguide cross section to submicron

levels. For example, 500 nm in width and 220 nm in height are typical dimensions for an SOI strip waveguide that can support single-mode operation. In contrast, a single-mode optical fibre for telecommunication wavelengths (1.55 μm) usually has a core diameter of about 8 μm . The strong optical confinement also allows for very tight bends (bend radius can be on the order of a few microns) and functional waveguide elements of ten to a few hundred microns. Therefore, large-scale integration of many functional elements on a single chip is within reach. Currently, the number of components integrated on silicon photonic chips is still very small (Sun et al. reported 4096 in [6]), but there is no doubt that this number, as well as the circuit complexity, will be increasing rapidly in the next few years.

Another key value of using silicon for photonics is to make most, and ideally all, of the devices using the existing fabrication facilities used to build advanced electronic chips. In the microelectronics industry, integrated circuit production facilities are expensive to build and maintain, but the foundry model separates the operation of the fabrication plant (also known as “fab”) from the design: fabless companies avoid costs by not owning such facilities and concentrate on the design, while pure-play foundries focus on fabricating ICs for other companies and keeping their fabs at full utilization. This CMOS fabrication infrastructure opens the door for commercialization and large-scale production of silicon photonic ICs [7]. The recent development of multi-project-wafer (MPW) services [8, 9] has already made advanced CMOS-compatible processes [10, 11] widely available to the community at modest cost, and will help promote the growth of fabless photonic companies. Note that “CMOS-compatibility” means photonic devices can be fabricated using CMOS process tools (e.g., lithography and etching) and materials (e.g., silicon), however, it does not mean using the tools and materials in exactly the same way as for traditional CMOS. There is wide agreement in the silicon photonics community that a device fabricated in a commercial CMOS fab (e.g., 200 mm or 300 mm pilot line) is supposed to be “CMOS-compatible”.

In terms of applications, a lot of research effort has been focused on short-reach optical interconnects, such as data centres and high-performance computing. In this digital age, data explosion is happening at every level from scalable cloud computing centres to new powerful consumer devices. In order to meet the demand for rapidly increasing data transfer rate, the widespread adoption of optical

interconnects is inevitable, owing to their inherent advantages over their electrical counterparts in terms of bandwidth, distance, and power consumption [12]. Silicon photonics is one of the leading candidate technologies for optical interconnects [13], due to its unique combination of low fabrication costs, performance enhancements resulting from electronic – photonic integration, and CMOS compatibility. Apart from data communications, there are many other applications being explored, including biosensors [14, 15], gas sensors [16], optomechanics [17, 18], quantum optics [19–22] nonlinear optics [23], mid-infrared optics [24], integrated microwave photonics [25–27], coherent communications [28], and so on.

1.1.2 State of the Art and Challenges

To date, all of the essential components to build an optical interconnect on silicon [29] – including lasers [5], modulators [13], detectors [30], waveguides [31], and various passive components [32] – have already been demonstrated.

Silicon waveguides, the earliest to attract the attention of researchers [33], have been studied extensively over the past two decades. There are a number of waveguide geometries that have been developed in silicon. The most common are strip waveguides, rib waveguides, and slot waveguides, as illustrated in Figure 1.1. Strip

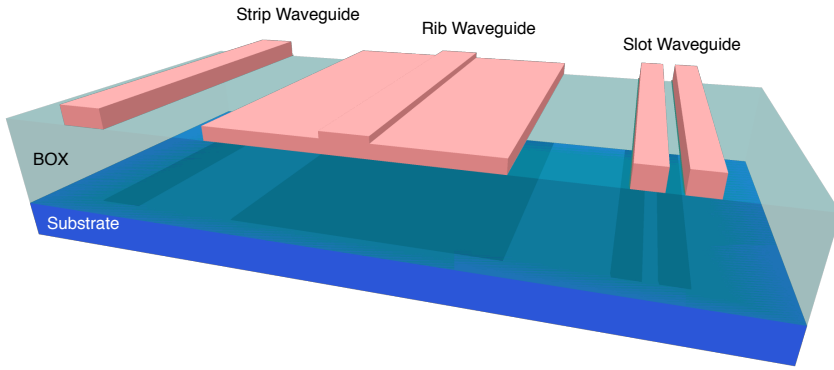


Figure 1.1: Common waveguide geometries in silicon-on-insulator.

waveguides often have small cross sections for single-mode operation and are often used to build compact and efficient devices. However, the strong optical confinement comes with some drawbacks: relatively low fabrication tolerance and high

scattering loss due to sidewall roughness. Typical reported propagation losses for strip waveguides are currently in the 2–3 dB/cm range using commercial processes [8, 9]. Rib waveguides have larger cross sections and the propagation loss can be effectively reduced (e.g. 0.27 dB/cm [34, 35]) because of the reduced overlap between the optical mode and the waveguide sidewalls. However, sharp bends are no longer possible due to the much weaker optical confinement. Therefore, a good solution is to use rib waveguides for long-distance straight connections and to use strip waveguides for where bends are needed. While the optical mode is already tightly confined in strip waveguides, the mode size can be further reduced by using a slot waveguide. A typical slot waveguide consists of two arms of silicon separated by a narrow trench filled with a lower index material [36]. The electric field is highly concentrated in the slot due to the dielectric discontinuity. This property allows for much stronger interactions between the optical mode and the surrounding materials. Therefore, slot waveguides are very promising for sensing applications [16], as well as electro-optical modulators [37], and nonlinear optics [38]. The connection between these different types of waveguides can be realized using tapers [35, 39].

A silicon laser – arguably the most important active photonic device among all – is actually the most challenging to realize [40]. Currently, due to the lack of an efficient on-chip light source, most silicon photonic chips couple light from an external laser using edge [41] or grating couplers [42–44]. Although the coupling efficiency has been significantly improved, the potential of an on-chip laser source is invaluable. Traditional semiconductor lasers use direct bandgap compound semiconductors, such as GaAs or InP. As an indirect bandgap material, silicon is not naturally capable of efficient photon emission. However, due to the intense interest in silicon photonics, a number of breakthroughs have been accomplished in the past decade [5]. Successful examples of realizing lasers on silicon include: silicon Raman lasers [45], germanium-on-silicon lasers [46] with bandgap engineering techniques, and hybrid silicon lasers [47] in which the silicon is bonded to compound semiconductors (such as InP). The last approach is of great interest, because it can combine the superior gain characteristics of compound semiconductors with the superior passive waveguide characteristics of silicon. As a result, many structures for hybrid silicon lasers have been demonstrated: Fabry-Perot (FP) lasers [48], dis-

tributed feedback (DFB) lasers [49], distributed Bragg reflector (DBR) lasers [50], sampled gratings DBR (SGDBR) lasers [51], microring [52] and microdisk lasers [53]. In many of these hybrid lasers, specifically DBR, DFB, and SGDBR lasers, Bragg gratings are used as the basic elements to select only one cavity mode to lase. However, the incompatibility of III-V materials with standard CMOS process is still an open issue.

Another crucial device is the silicon optical modulator, which has also been improved dramatically in recent years [13]. When applying an electric field to a material, electro-optic effects occur: a change in the refractive index is known as electro-refraction (e.g., the Pockels effect and the Kerr effect), whereas a change in the absorption coefficient is known as electro-absorption (e.g., the Franz–Keldysh effect and the quantum-confined Stark effect). However, these traditional effects are very weak in pure silicon at wavelengths of $1.3 - 1.55 \mu\text{m}$ [54]. The most common method to achieve modulation in silicon so far has been to exploit the plasma dispersion effect, where a change in free carrier density results in a change in the refractive index. The control of free carrier density can be achieved through mechanisms such as carrier injection, accumulation or depletion [13]. The refractive index change can be converted to intensity modulation by using a Mach–Zehnder interferometer (MZI) in which the refractive index change is used to shift the relative phase of two propagating waves such that they interfere either constructively or destructively [55], or using a resonant structure in which the resonant condition is controlled by the refractive index [56]. Several figures of merit are usually used to characterize a modulator, including modulation speed (bandwidth) and depth (extinction ratio), optical bandwidth, insertion loss, area efficiency (footprint) and power consumption. Ideally, silicon optical modulators will need to have high modulation speed and extinction ratio, large optical bandwidth, small footprints, low insertion loss and ultra-low power consumption. They must also be CMOS-compatible. However, these requirements often contradict each other, and therefore an innovative engineering solution is necessary to achieve an optimal trade-off [13]. In general, MZI-based modulators have a large working spectrum ($>20 \text{ nm}$) [57], whereas typical resonator-based modulators can only work within $\sim 0.1 \text{ nm}$ [58]. However, the use of resonant structures has demonstrated more advantages over MZI, including much smaller footprint, much lower modulation voltage and power

consumption, lower insertion loss, higher extinction ratio with comparable modulation speed [59, 60], etc. In addition to conventional resonant structures such as micro-rings and micro-disks, Bragg gratings can also be used to form micro-cavities, and therefore, can join in the development of silicon modulators.

Again, due to its inherently large bandgap, silicon itself is not efficient for photon detection at wavelengths of $1.3 - 1.55 \mu\text{m}$. Currently, most research on integrated photodetectors (PD) is focused on using Ge as the absorption material, due to its much higher absorption coefficient and its CMOS-compatibility. Waveguide-coupled Ge photodetectors are of particular interest as they enable direct integration with silicon waveguides, and they also have better performance than normal-incidence photodetectors. As the state of the art, a responsivity of 0.95 A/W at 1550 nm with 36 GHz 3-dB bandwidth has been demonstrated [61].

Another exciting trend in silicon photonics is the transition from device development to system-level integration. Although device improvement will continue to be important, it is expected that over the next few years, the number of system designers will grow much faster than that of device engineers [62]. A typical system example is an on-chip wavelength division multiplexing (WDM) architecture [63]. Intel, the world's largest semiconductor chip maker, has demonstrated a 50G silicon photonics link in 2011, which has hybrid silicon lasers, modulators, multiplexers, demultiplexers, and photodetectors all integrated on chip [64].

Silicon photonics is also beginning to be a significant industry in its own right [62]. Electronics giants such as Intel, IBM, Samsung, Oracle, Cisco, and many others have been very active in the development of this technology. Luxtera, a fabless startup founded in 2001, is one of the earliest on the commercialization path. They have shipped a million 10G active optical cables enabled by silicon photonics [65], and are now moving towards 100G. Teraxion, a Canadian optical component company, has been developing silicon photonic coherent receivers in the past few years and reported the smallest integrated receiver in the industry for coherent detection [28]. There are a number of other startups, not only in the communication sector, but also in other sectors, such as Genalyte that makes silicon photonic biosensor chips [66].

There are many challenges still remaining to be addressed. To name a few, silicon photonic devices are very sensitive to temperature variations on the chip, due

to the large thermo-optic coefficient of silicon. Owing to the electronic-photonic integration, it is possible to integrate thermal feedback mechanisms, but the system complexity and power consumption will definitely be higher. The polarization independence is also an important issue for many applications. In terms of fabrication, although the fabrication facilities are the same as for CMOS electronics, this does not mean that the processes are exactly the same; on the contrary, the process flows for fabricating electronic-photonic integrated circuits are very different from those of electronics alone. Such processes are complicated and expensive to develop, and significant effort will be required to keep them stable [7]. Moreover, yield management will be critical in the near future.

1.2 Bragg Gratings

In the simplest configuration, a Bragg grating is a structure with periodic modulation of the effective refractive index (n_{eff}) in the propagation direction of the optical mode, as shown in Figure 1.2. This modulation is commonly achieved by

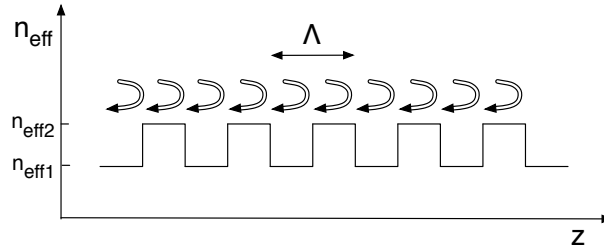


Figure 1.2: Longitudinal effective index profile of a uniform grating (z is the propagation direction, Λ is the grating period, n_{eff1} is the low effective refractive index and n_{eff2} is the high effective refractive index).

varying the refractive index (e.g., alternating material) or the physical dimensions of the waveguide. At each boundary, a reflection of the travelling light occurs, and the relative phase of the reflected signal is determined by the grating period and the wavelength. The repeated modulation of the effective index results in multiple and distributed reflections. The reflected signals only interfere constructively in a narrow band around one particular wavelength, namely the Bragg wavelength. Within this range, light is strongly reflected. At other wavelengths, the multiple

reflections interfere destructively and cancel each other out, and as a result, light is transmitted through the grating. Figure 1.3 shows the typical spectral response of

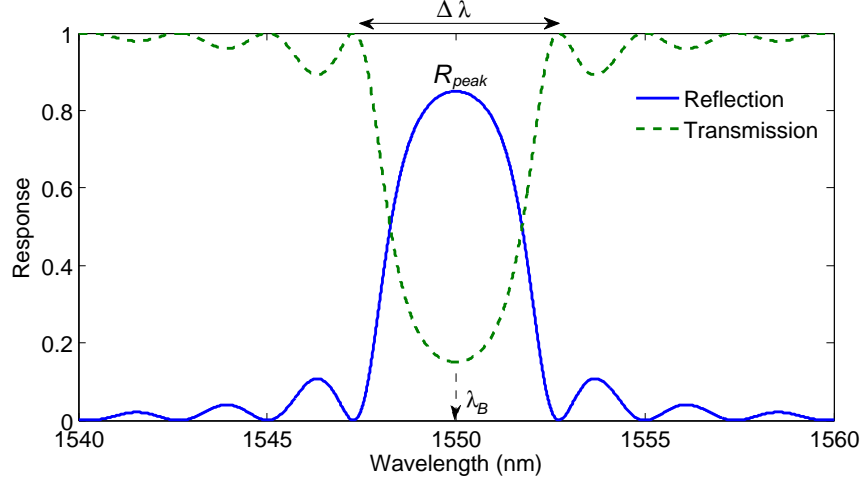


Figure 1.3: Typical spectral responses of a uniform Bragg grating.

a uniform Bragg grating. The Bragg wavelength is given as:

$$\lambda_B = 2\Lambda n_{eff} \quad (1.1)$$

where Λ is the grating period, and n_{eff} is the effective index of the structure without the grating. Based on coupled-mode theory [67], the effect of the periodic structure is to couple forward-going and backward-going waves in the grating. We can write the electric field as a sum of forward (S) and backward (R) propagating waves:

$$E(z) = R(z) \exp(-j\beta_0 z) + S(z) \exp(j\beta_0 z) \quad (1.2)$$

where β_0 is the Bragg propagation constant:

$$\beta_0 = \frac{2\pi}{\lambda_B} n_{eff} \quad (1.3)$$

Following the derivation in [67], we obtain the coupled-mode equations:

$$\frac{dR}{dz} + j\Delta\beta R = -j\kappa S \quad (1.4)$$

$$\frac{dS}{dz} - j\Delta\beta S = j\kappa R \quad (1.5)$$

Here, κ is often defined as the coupling coefficient of the grating and can be interpreted as the amount of reflection per unit length. For a stepwise effective index variation as shown in Figure 1.2 ($\Delta n = n_{eff2} - n_{eff1}$), the reflection at each interface can be written as $\Delta n / 2n_{eff}$ according to the Fresnel equations. Each grating period contributes two reflections, therefore the coupling coefficient is:

$$\kappa = 2 \frac{\Delta n}{2n_{eff}} \frac{1}{\Lambda} = \frac{2\Delta n}{\lambda_B} \quad (1.6)$$

For a sinusoidal effective index variation $n(z) = n_{eff} + \Delta n / 2 \cdot \cos(2\beta_0 z)$, the coupling coefficient is reduced by a factor of $\pi/4$ [67]:

$$\kappa = \frac{\pi \Delta n}{2\lambda_B} \quad (1.7)$$

Similarly, for other effective index variations, we can take the Fourier expansions: $n(z) = n_{eff} + \sum_i \Delta n_i / 2 \cdot \cos(i \cdot 2\beta_0 z)$, and the coupling coefficient can be derived from the first-order Fourier component: $\kappa = \pi \Delta n_1 / (2\lambda_B)$. For example, the coupling coefficient of a triangular grating is reduced by a factor of $2/\pi$ compared to the square case (Eq. 1.6):

$$\kappa = \frac{4\Delta n}{\pi\lambda_B} \quad (1.8)$$

The solutions of the coupled-mode equations are given in [67] with details. The reflection coefficient for a uniform grating with a length of L can be described by:

$$r = \frac{-i\kappa \sinh(\gamma L)}{\gamma \cosh(\gamma L) + i\Delta\beta \sinh(\gamma L)} \quad (1.9)$$

with

$$\gamma^2 = \kappa^2 - \Delta\beta^2 \quad (1.10)$$

Here, $\Delta\beta$ is the propagation constant deviation from the Bragg wavelength:

$$\Delta\beta = \beta - \beta_0 = \frac{2\pi n_{eff}(\lambda)}{\lambda} - \frac{2\pi n_{eff}(\lambda_B)}{\lambda_B} \approx -\frac{2\pi n_g}{\lambda_B^2} \Delta\lambda \quad (1.11)$$

with $\Delta\beta \ll \beta_0$. In this expression, the wavelength dependence of the effective index is considered, hence the group index n_g appears:

$$n_g = n_{eff} - \lambda \frac{dn_{eff}}{d\lambda} \quad (1.12)$$

For the case where $\Delta\beta = 0$, Eq. 1.9 is written as $r = -i \tanh(\kappa L)$, therefore, the peak power reflectivity at the Bragg wavelength is:

$$R_{peak} = \tanh^2(\kappa L) \quad (1.13)$$

and the reflection has a $\pi/2$ phase at the Bragg wavelength.

The bandwidth is another critical figure of merit for Bragg gratings. There are several definitions of bandwidth, however, the most easily identifiable one is the bandwidth between the first nulls around the main reflection peak. Using Eq. 1.9 and Eq. 1.10, we can easily obtain the condition for zero reflectivity:

$$-\gamma^2 = \Delta\beta^2 - \kappa^2 = \left(\frac{M\pi}{L} \right)^2, \quad M = 1, 2, 3, \dots \quad (1.14)$$

Next, we will explain this in a relatively intuitive manner. Using the coupled-mode equations (Eq. 1.4 and Eq. 1.5), we can also write the forward propagation wave as:

$$\frac{d^2S}{dz^2} + (\Delta\beta^2 - \kappa^2)S = 0 \quad (1.15)$$

When $\Delta\beta$ is smaller than κ , i.e., the wavelength is very close to the Bragg wavelength, we can see that S resembles a wave with exponentially decaying amplitude. This is easy to understand because the light is strongly reflected. As the wavelength

gets closer to the Bragg wavelength (i.e., $\Delta\beta$ becomes smaller), the decay will be faster because the reflection becomes stronger (i.e., the interference is more constructive). This also means that the penetration depth becomes shorter for smaller $\Delta\beta$. When $\Delta\beta$ is larger than κ , i.e., the wavelength is outside of the main reflection band, S resembles a wave with a propagation constant of $\sqrt{\Delta\beta^2 - \kappa^2}$. In this case, the boundaries of the grating will act like abrupt interfaces, thus forming a FP-like cavity. The nulls in the reflection spectrum are analogous to the FP resonances ($L\sqrt{\Delta\beta^2 - \kappa^2} = M\pi$). At these wavelengths, light is transmitted through the cavity, thus resulting in zero reflectivity. Using $M = 1$, the bandwidth between the first nulls around the main reflection peak can be determined by [67]:

$$\Delta\lambda = \frac{\lambda_B^2}{\pi n_g} \sqrt{\kappa^2 + (\pi/L)^2} \quad (1.16)$$

From Eq. 1.16, we can see that the bandwidth is determined by both κ and L . However, for sufficient long gratings ($\pi L \ll \kappa$), the bandwidth is primarily determined by κ (i.e., the grating index contrast). Note that this bandwidth is larger than the 3-dB bandwidth, which is also often used for the characterization of Bragg gratings. It should also be noted that, for the sake of simplicity, the analysis above assumes that the grating is lossless. However, losses can be accounted for by replacing $\Delta\beta$ by $\Delta\beta - j\alpha_0$ in Eq. 1.10, where α_0 is the loss coefficient for the field (the loss coefficient for the intensity is $2\alpha_0$).

1.3 Silicon Photonic Bragg Gratings

Recent advances in silicon photonics have led to the integration of Bragg gratings on the SOI platform, with the first demonstration in 2001 by Murphy et al. [68]. Generally, an integrated Bragg grating is formed in a waveguide with physical corrugations that lead to the modulation of the effective refractive index in the waveguide. This is in contrast to the manufacture of fiber Bragg gratings (FBG), where the fiber is photosensitive and exposed to intense ultraviolet (UV) light so that the material refractive index is modulated in the fiber core. Other than using physical corrugations, there are a few other approaches to make gratings in silicon, such as amorphous silicon gratings [69], ion implanted Bragg gratings [70, 71],

carrier-induced gratings with a p-i-n junction [72]; however, these approaches are much less common and are beyond the scope of this discussion.

1.3.1 Objectives

Integrated Bragg gratings will be an essential building block for silicon photonics. Although the research in this area has been making steady progress in recent years, much more effort is still needed to improve the grating performance, especially when using CMOS fabrication techniques. Furthermore, there are many potential devices and applications to be explored.

First, the demonstration of integrated Bragg gratings has been mostly based on SOI rib waveguides with large cross sections [68, 73–75]. However, the current trend in silicon photonic circuits requires smaller devices for improved cost efficiency. Therefore, we will focus on the integration of Bragg gratings in silicon waveguides with small cross sections, particularly at the submicron level.

As mentioned earlier, strip waveguides are usually submicron. A small perturbation on the sidewalls can cause a considerable grating coupling coefficient, thus resulting in a large bandwidth. The bandwidths reported by others are generally on the orders of a few tens of nanometers [76, 77]. Tan et al. have demonstrated smaller bandwidths on the orders of a few nanometers, but the grating structures are more complicated, such as using weakly coupled pillars outside of the waveguide [78], or using two coupled waveguides [79, 80]. For many applications such as WDM, even narrower bandwidths (e.g., <100 GHz or 0.8 nm) are required. Simard et al. have demonstrated strip waveguide gratings with 3-dB bandwidths smaller than 50 GHz, however, it was achieved at the expense of using a multi-mode waveguide (1200 nm wide) and a third-order grating [81]. Therefore, one of our objectives is to design narrow-band first-order gratings without sacrificing single-mode operation.

Often, uniform gratings exhibit large side-lobes in their reflection spectra, as shown in Fig. 1.3. It is well known that apodization can help with side-lobe suppression (“apodization” refers to gradually increasing and then decreasing the grating coupling coefficient along the waveguide), which makes the gratings nonuniform. Actually, most gratings in practical applications are nonuniform [82]. There-

fore, we will investigate various nonuniform grating structures and study their applications.

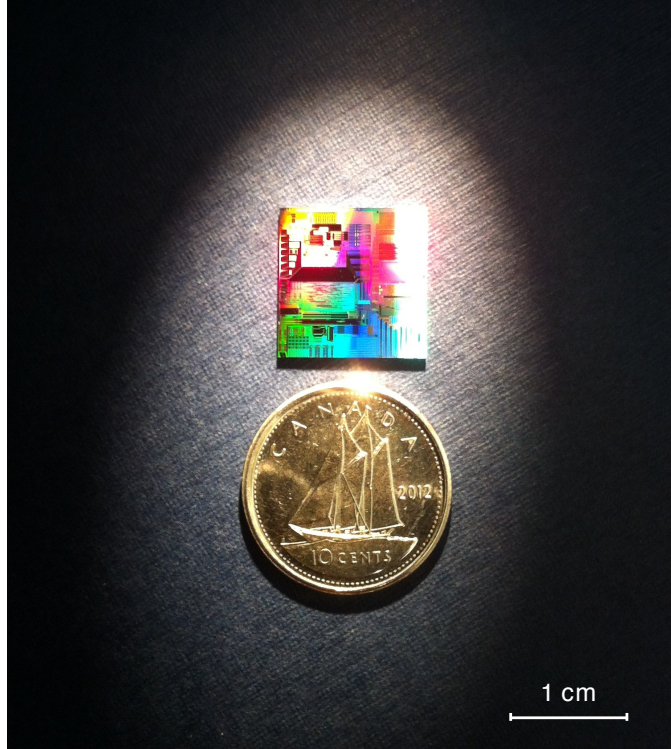


Figure 1.4: A typical silicon photonic chip and a Canadian dime.

In terms of fabrication, electron beam (e-beam) lithography was typically used for the fabrication of SOI Bragg gratings. Although e-beam lithography can make very small features, it is unsuitable for commercial applications [31]. In this thesis, we will explore the possibilities of using CMOS-compatible processes, particularly using MPW services. Unless stated otherwise, all devices in this thesis were fabricated at IMEC, Belgium, using their relatively mature silicon photonic technology with 193 nm deep UV lithography [8]. Figure 1.4 shows one of our silicon photonic chips fabricated at IMEC, compared with a Canadian dime (the smallest Canadian coin in size). This chip has thousands of devices designed by more than 20 students from across Canada. The dimension of the chip is 12.73 mm × 12.95 mm, whereas the diameter of the dime is 18.03 mm [83].

Another major objective of this thesis is to provide insight into practical issues and challenges involved with the design, fabrication, and characterization.

1.3.2 Thesis Organization

This remainder of this thesis is organized into three main chapters, each focusing on a specific waveguide geometry, and a concluding chapter.

In Chapter 2, we focus on strip waveguide Bragg gratings. We will start with the fundamentals: mode profile and simple uniform gratings. Technical details about the design, layout, and measurement are also given in this chapter. We also present a number of design variations. The lithographic effects and a prediction model are then discussed. The thermal sensitivity and the wafer-scale nonuniformity are also investigated. Finally, we will discuss phase-shifted gratings in strip waveguides and their various applications.

In Chapter 3, we focus on rib waveguide Bragg gratings. Again, we will start with the fundamentals: mode profile and simple uniform gratings. We will then present apodized gratings to reduce the side-lobes. We also demonstrate two advanced grating structures: multi-period gratings and spiral gratings. Finally, we will present the thermal sensitivity and the wafer-scale nonuniformity.

In Chapter 4, we focus on slot waveguide Bragg gratings. We demonstrate the design, fabrication, and characterization of both uniform and phase-shifted gratings. We investigate a number of design variations for both types of device. We also show a novel silicon photonic biosensor using a slot waveguide phase-shifted grating.

Finally, the main conclusions and the future work are described in Chapter 5.

Chapter 2

Strip Waveguide Bragg Gratings

In this chapter, we will discuss the simplest type of integrated Bragg grating: a strip waveguide Bragg grating. It is simple because the grating and the waveguide can be defined in a single lithography step. We will briefly discuss the fundamentals of strip waveguides, and then describe how a uniform grating is designed, fabricated, and characterized. We will explore many design variations, such as the corrugation width and the grating period. An important issue with the CMOS fabrication process is that the fabricated corrugations are always rounded due to the lithographic effects; therefore, we propose a prediction model to take into account the lithographic distortions in the design-fabrication-test flow. We also present the thermal sensitivity and the wafer-scale nonuniformity of strip waveguide gratings, which are very important for practical applications. We will also discuss phase-shifted gratings and give a few examples of applications. Finally, we experimentally demonstrate sampled gratings and the Vernier effect.

2.1 Strip Waveguide

The strip waveguide is one of the most common types of silicon photonic waveguides, as illustrated in Figure 2.1. It is basically a thin strip of silicon on top of the buried oxide layer. The buried oxide layer needs to be thick enough to isolate the waveguide from the bottom silicon substrate. Specifically, in Figure 2.1, the thickness of the top silicon layer is only 220 nm, while the buried oxide layer is 2 μm

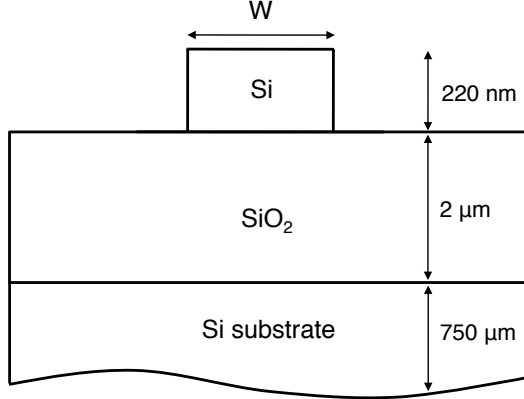


Figure 2.1: Schematic of a strip waveguide cross section (not to scale).

thick. Note that this is a popular SOI wafer currently used for silicon photonics, particularly in CMOS foundries, and we will use it throughout the thesis. In general, there are two options for the top cladding material: air and SiO_2 . However, it can be other low index materials. For example, in biosensing applications, the waveguide is usually immersed in water, which has a refractive index between air and SiO_2 ($n \approx 1.33$).

The strip width (W) is the only dimension to be designed. In general, a single-mode waveguide is preferred for Bragg grating designs. In this thesis, we use a commercial tool, Lumerical MODE Solutions, for all the mode calculations [84]. Figure 2.2 shows the simulated mode profiles for 500 nm strip waveguides: (a) and (b) are with air cladding, (c) and (d) are with oxide cladding. In a rectangular waveguide, there are two families of modes, the transverse electric (TE) modes and the transverse magnetic (TM) modes. TE means the electric field is parallel to the substrate, while TM means the electric field is perpendicular to the substrate. In a more precise manner, the modes in Figure 2.2 are TE-like (or quasi-TE) and TM-like (or quasi-TM) modes, depending on whether they are mostly polarized in the x or y direction. The main field components of the TE-like modes are E_x and H_y , while those of the TM-like modes are E_y and H_x . For simplicity, however, we will use “TE” and “TM” hereafter. Due to the high index contrast between the silicon and the cladding material, the fundamental TE modes are strongly confined

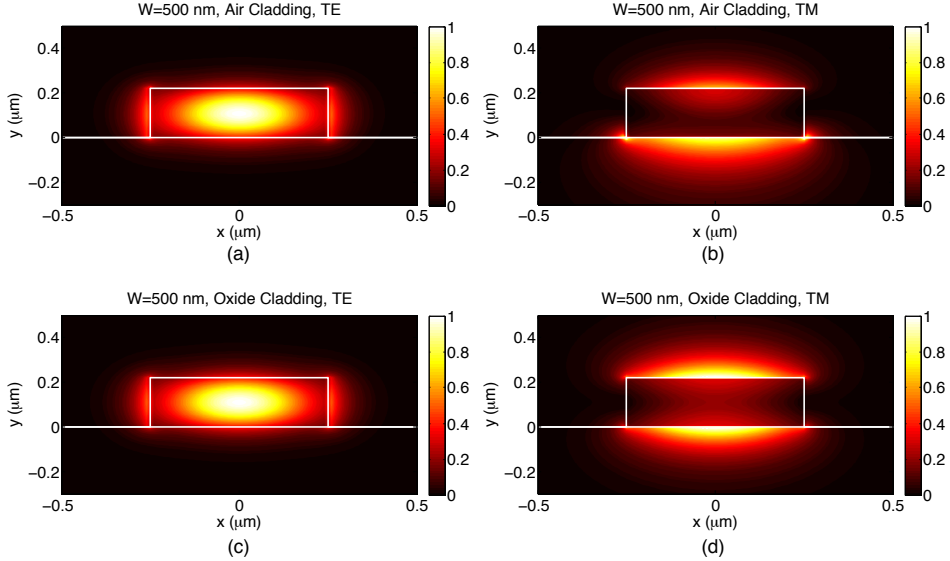


Figure 2.2: Simulated electric field of the fundamental modes in 500 nm strip waveguides: (a) TE mode with air cladding, (b) TM mode with air cladding, (c) TE mode with oxide cladding, and (d) TM mode with oxide cladding.

in the silicon core, as shown in Figure 2.2(a) and (c). The TM modes, however, have relatively low intensities inside the silicon but much higher intensities outside of the top and bottom interfaces. We also see that, in Figure 2.2(b), the intensity distribution above and below silicon is asymmetric, due to the fact that the buried oxide has a higher refractive index than the top air cladding. When the cladding is oxide, the mode profile becomes symmetric, as shown in Figure 2.2(d).

For air cladding, to obtain a single TE mode operation at 1550 nm, the waveguide width is usually larger than 300 nm to support a fundamental mode but smaller than 600 nm to avoid higher-order modes [85]. Again, note that in this regime, the waveguide supports one TE-like mode, as well as one TM-like mode. In this thesis, however, we only focus on TE mode operation. For oxide cladding, the maximum waveguide width to suppress the second TE mode is about 450 nm, smaller than that for air cladding.

The propagation loss of a silicon waveguide is mainly the scattering loss due to the waveguide roughness. The roughness of the sidewalls arises from the lithog-

raphy and etching process, and generally, is higher than the roughness of the top and bottom interfaces. From Figure 2.2(a) and (c), we also see that the TE modes have considerable evanescent field around the sidewalls. Therefore, the propagation loss of TE modes is dominated by the sidewall roughness. At 1550 nm, typical propagation losses of strip waveguides are in the 2–3 dB/cm range [8, 9]. Thermal oxidation is a technique to smooth the sidewalls and thus reduce the waveguide loss, but it could be detrimental to sidewall gratings.

Figure 2.3 shows the scanning electron beam (SEM) image of a fabricated strip waveguide. It can be seen that the cross section is not perfectly rectangular and

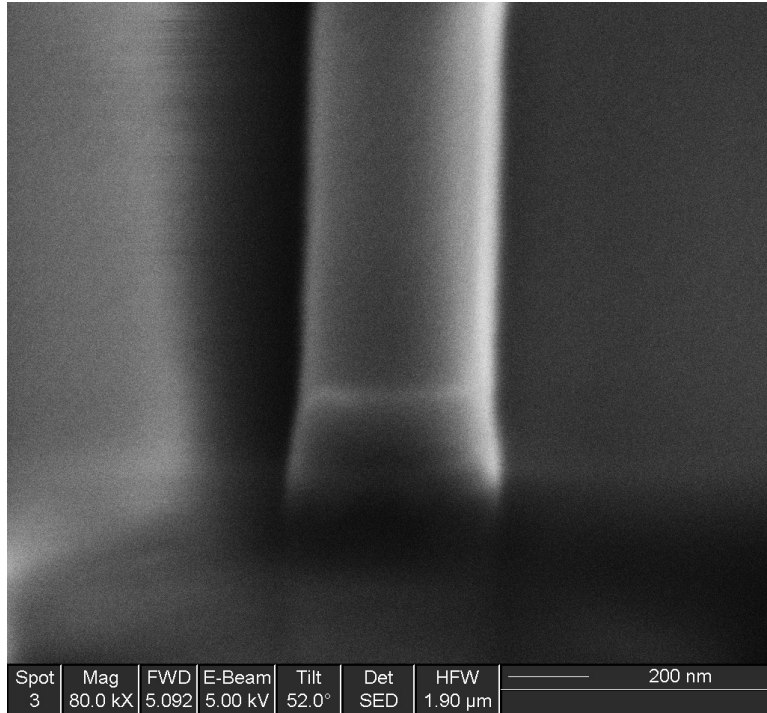


Figure 2.3: SEM image of a 500 nm strip waveguide. The waveguide was milled using a focused ion beam (FIB) to expose the cross section.

that the sidewalls have a small angle (typically 10°). Such geometric imperfections will slightly affect the mode profile and the effective index of the waveguide, and consequently, affect the Bragg gratings on the waveguide.

A main advantage of strip waveguide is that it enables very tight and low-loss bends. There are several loss mechanisms in bends, but the major one is the mode-mismatch loss in strip waveguides [86]. The bending loss depends on the bending radius, increasing sharply for smaller bends. For a 450×220 nm strip waveguide fabricated at IMEC, the bending loss is 0.071 dB, 0.02 dB, and 0.009 dB per 90° bend for a bending radius of 1 μm , 3 μm , and 5 μm respectively [32]. In this thesis, we will use bends larger than 3 μm so that the bending losses are negligible.

2.2 Uniform Gratings

In this section, we will present the design of uniform Bragg gratings in strip waveguides. We will discuss several design variations. Many details about the layout and measurement are also given.

2.2.1 Design

Figure 2.4 shows the schematic of a uniform grating in a strip waveguide using rectangular sidewall corrugations. The corrugation on each sidewall has a width of ΔW and comprises recessed and protruding portions ($\pm \Delta W/2$). We chose this configuration rather than the recessed-only or protruding-only configuration, because for varying corrugation widths, the average effective index is approximately constant so that the Bragg wavelength will not shift dramatically.

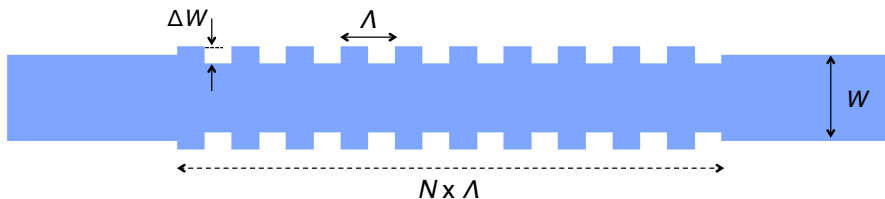


Figure 2.4: Schematic of a uniform strip waveguide grating.

Figure 2.5 shows a typical design flow for a uniform Bragg grating. Usually, we start the design by first choosing a waveguide width. As discussed in Section 2.1, we prefer a single-TE mode waveguide, and this requires a submicron waveguide width (i.e., <600 nm with air cladding, and <450 nm with oxide cladding). How-

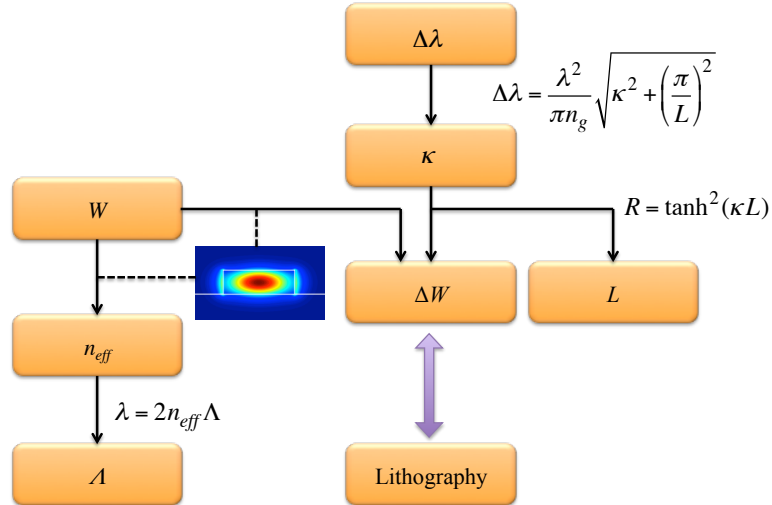


Figure 2.5: Typical design flow for a uniform Bragg grating: 1) choose a certain waveguide cross section, 2) calculate the mode profile and effective refractive index, then calculate the grating period based on the Bragg condition, 3) calculate the coupling coefficient for a particular bandwidth (assuming the grating is sufficiently long and a high reflectivity is needed), 4) calculate the corrugation width with the assistance of mode simulation and lithography simulation, 5) calculate the grating length.

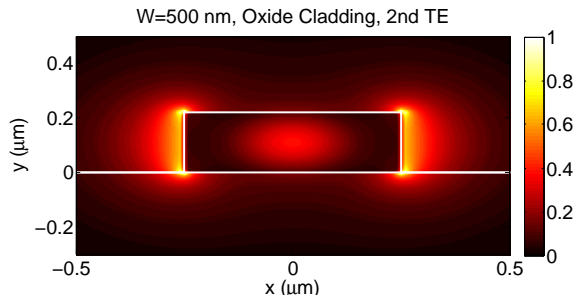


Figure 2.6: Simulated electric field of the second TE mode in a 500 nm strip waveguide with oxide cladding. The majority of the electric field is on the sidewalls, resulting in a much lower effective index and a much higher propagation loss than the fundamental TE mode.

ever, this criterion can be relaxed a bit. For example, in the case of a 500 nm waveguide with oxide cladding, the confinement of the second TE mode is very weak, as shown Figure 2.6. The majority of the electric field is on the sidewalls, thus resulting in a much lower effective index (1.49) than the fundamental TE mode (2.45), as well as a much higher propagation loss. Therefore, in practice, this second TE mode can be neglected in a Bragg grating design.

Once the waveguide width is determined, the effective index of the fundamental TE mode is known from the mode calculation, then the grating period can be calculated using the Bragg condition (i.e., Eq. 1.1). The next parameter to be considered is the corrugation width, which determines the coupling coefficient and the stop bandwidth. Note that the lithography effect should also be taken into account, as will be discussed later. The last parameter to be considered is the grating length, or the number of grating periods (N), which determines the peak reflectivity.

2.2.2 Layout

When the design parameters are ready, the next step is to create the mask layout, generally in a file format called GDSII, which is the de facto industry standard for IC fabrication. To generate a GDSII file, there are many commercial electronic design automation (EDA) software and free GDSII utilities. Here we list a few tools that are used in the work of this thesis:

- KLayout: an excellent and free GDS viewer that also provides basic editing capabilities [87].
- dw-2000: an integrated environment that includes a full-featured layout editor and a comprehensive design rule checker (DRC). It also allows for the use of a technology package (e.g., CMC-IMEC SOI Technology Package) [88].
- Mentor Graphics Pyxis Layout: a full-custom IC design platform that supports an extensive set of functions, especially the AMPLE scripting language, process design kit (PDK), automatic routing (IRoute), schematic driven layout (SDL), and integration with other Mentor Graphics tools such as Calibre nmDRC and Calibre nmLVS [89].

In a GDSII layout, a careful design hierarchy is very important. Typically, the full chip consists of many building block cells replicated and placed in higher level cells. The proper use of cells can greatly minimize the data volume and reduce the time of generating, reading, and editing. This is particularly true for the design of Bragg gratings. For example, to generate a uniform grating, the most efficient approach is to make one grating period as a cell, and then make an array of this cell as a higher-level cell. All the three tools mentioned above support hierarchical operations, but Pyxis Layout is most powerful.

In practice, there are many design constraints, depending on the fabrication process. The first requirement is that the vertices of all objects must also conform to a discrete grid (e.g., 1 nm or 5 nm). For a Bragg grating design, this requires that the grating period is an integer number of grid points. Ideally, the final layout should not violate any design rules before submitted to the foundry, such as the minimum feature sizes (e.g., width, spacing, enclosure) and density rules. This is sometimes a huge obstacle to the design of Bragg gratings. For example, all the sidewall corrugations could be detected as violations to the minimum feature size rule. Yet, it is often possible to waive such DRC errors, as they have little impact on the process yield. However, the density rules are always mandatory because they may affect the yield of other customers on the chip. In order to meet the target density rules, most modern processes need addition of dummy tiles to the layout to ensure the density is consistent (for various reasons such as planarization).

Figure 2.7 shows the schematic of two layout configurations. Each configuration consists of one input port and two output ports (transmission and reflection). Each port is an integrated waveguide-to-fiber grating coupler (GC) designed for TE polarization [42, 43, 90]. We use a Y-branch splitter to collect the reflected light. The first configuration uses two individual fibers, one for input, and the other for transmission or reflection, while the second configuration uses a fiber array (PLC Connections PM fiber array with $127 \mu\text{m}$ pitch, 4 or 8 channels). Although the first configuration may provide more flexibility to the layout, the second configuration has more advantages. First, it allows for the simultaneous measurement of both transmission and reflection. Second, it is easier and faster to perform automatic alignment. Third, the coupling efficiency is more stable.

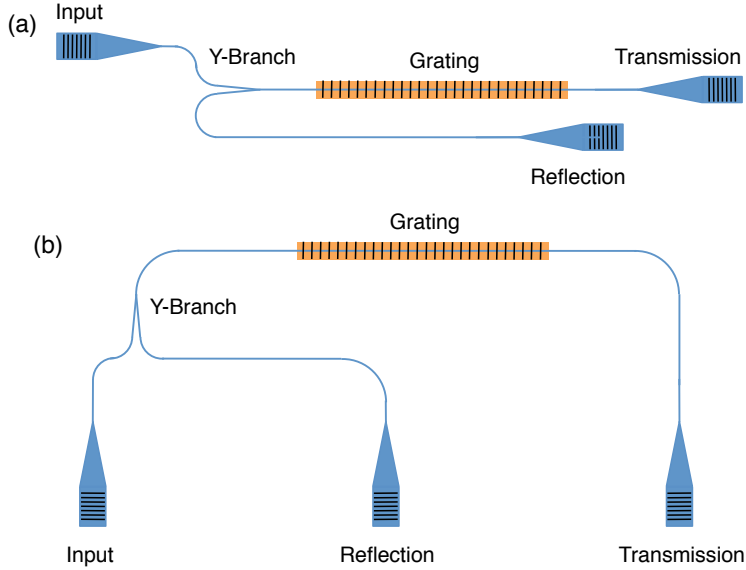


Figure 2.7: Schematic diagram of the device layout (not to scale): (a) individual fiber configuration, (b) fiber array configuration.

Figure 2.8 shows an approach to design a space-efficient layout using the fiber array configuration. On the right side are Bragg grating devices with many design variations. The routing waveguides run between the GCs, with a $4 \mu\text{m}$ center-to-center waveguide spacing, which is sufficient to avoid cross-talk between adjacent waveguides. Note that this routing block is generated using scripts in Pyxis Layout and can be re-used for similar designs.

2.2.3 Fabrication

Figure 2.9 shows the top view SEM image of a fabricated strip waveguide grating. Again, the device was fabricated at IMEC using 193 nm DUV lithography (ASML PAS5500/1100 ArF scanner) and inductively coupled plasma (ICP) reactive-ion etching (RIE) dry etching. Clearly, we can see that the gratings actually fabricated are severely rounded, resembling sinusoidal shapes. This is due to the smoothing effect of the lithography and will reduce the grating coupling coefficient. We will further discuss this effect in Section 2.3.

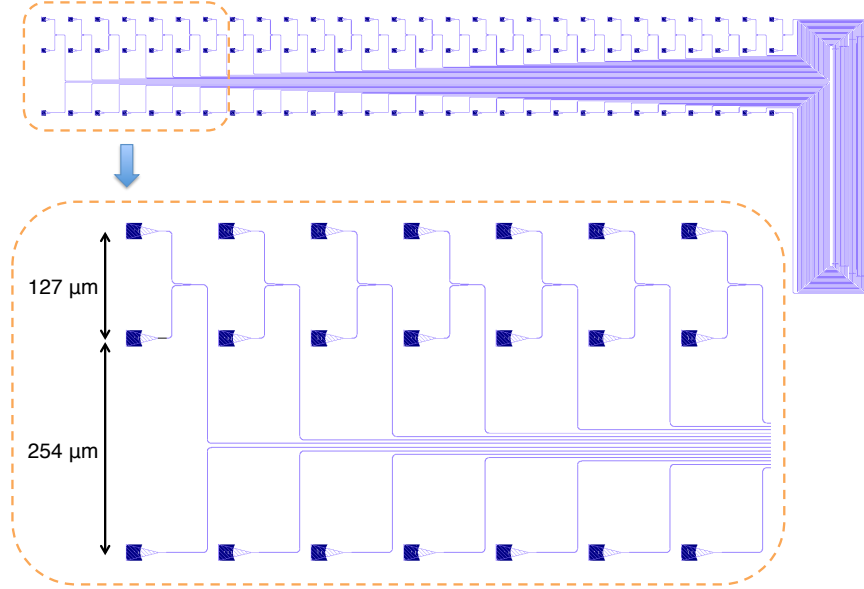


Figure 2.8: An approach to increase the device packing efficiency using the fiber array configuration. The grating devices are located in the bundle on the right side, and the routing waveguides run between the grating couplers.

Figure 2.10 and Figure 2.11 show the SEM images of a Y-branch and a GC, respectively. The small square boxes in Figure 2.11 were the result of tiling, which are necessary to meet the density rules as mentioned above. Figure 2.12 shows a microscope image of a compact layout example using the approach in Figure 2.8.

2.2.4 Measurement

The measurement setup typically consists of a tunable laser source, optical power sensors, fibers, and stages. Depending on the layout configuration, the fibers can be either two individual fibers, or a multi-channel fiber array. Figure 2.13 shows a setup using individual fibers, each of which is motor-controlled; and the software records the received power in real time [91, 92].

We also have an advanced setup using a multi-channel fiber array. Figure 2.14 shows the block diagram of the overall setup. The chip is placed on an automated micro-positioning stage while the fiber array is fixed during the measurement. The

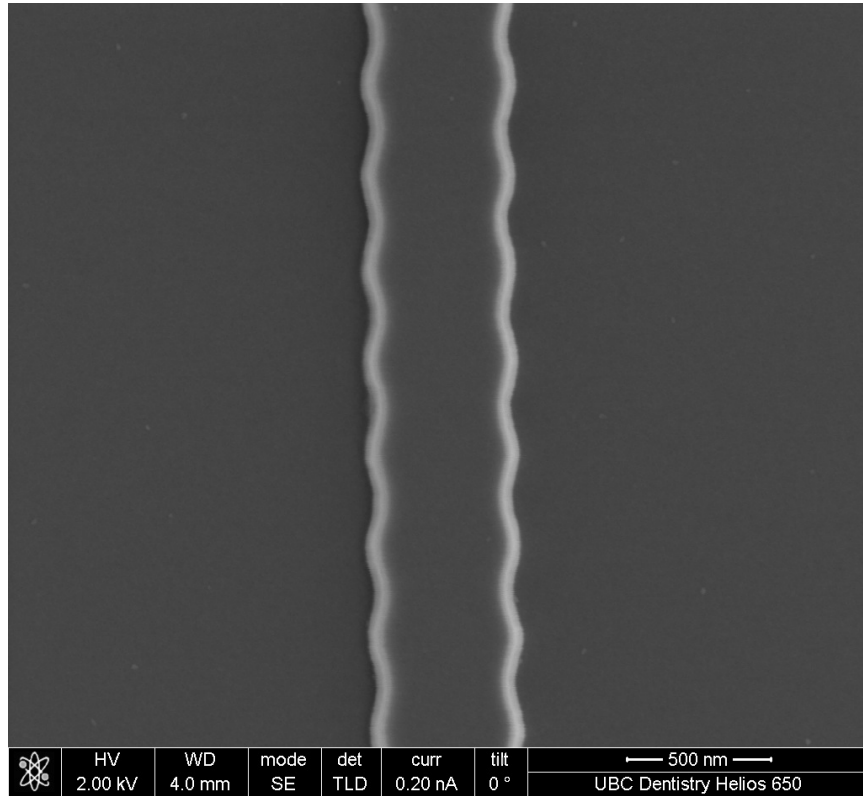


Figure 2.9: Top view SEM image of a fabricated strip waveguide grating with design parameters: $W = 500$ nm, $\Delta W = 80$ nm. Note that the rectangular corrugations we used in the design were rounded due to the lithography.

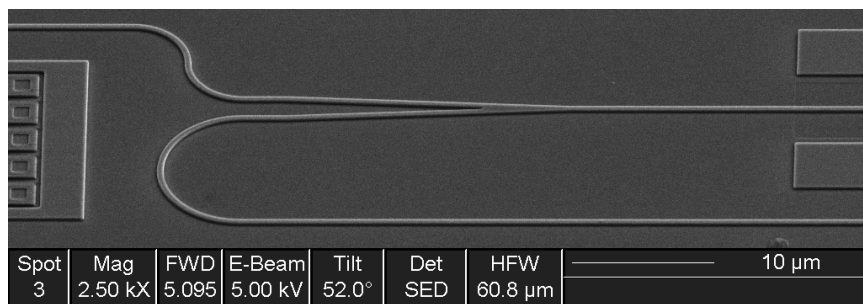


Figure 2.10: Tilted view SEM image of a fabricated Y-branch as illustrated in Figure 2.7(a).

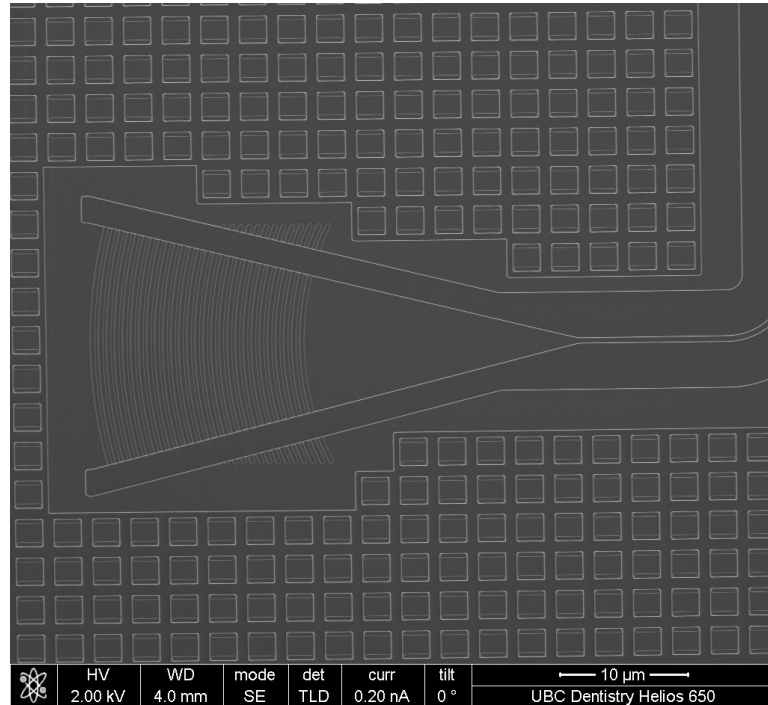


Figure 2.11: Top view SEM image of a fabricated grating coupler (GC). The layout of the GC was illustrated in Figure 2.8, and the square tiles were added around the GC to meet the density rule.

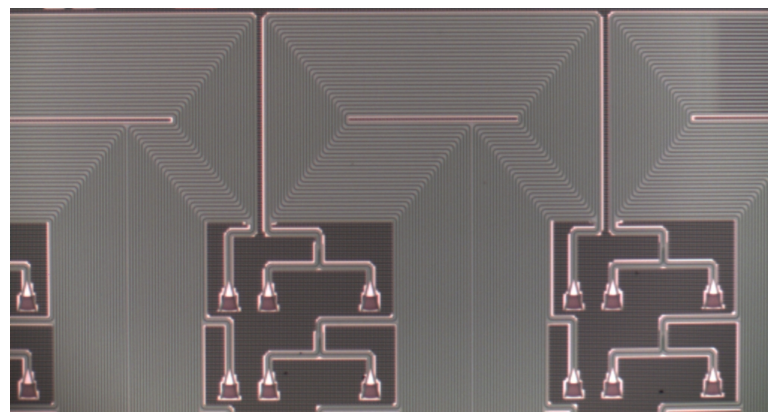


Figure 2.12: Part of a fabricated chip showing the compact routing approach illustrated in Figure 2.8.

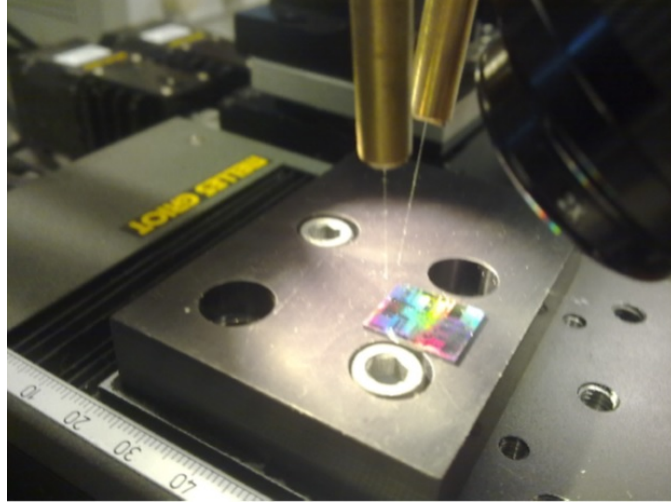


Figure 2.13: A measurement setup using two individual fibers.

measurement is fully automated, i.e., the software loads a file that contains the coordinates of all the GCs, automatically moves the stage to align a particular set of GCs with the fiber array, performs the wavelength sweep, records the data, and proceeds with the next device. The alignment usually takes less than a minute. The time to complete the wavelength sweeping depends on the wavelength range, resolution, sweeping speed of the tunable laser, number of scans, etc. In this thesis, we used a high-end tunable laser (Agilent 81600B opt. 201) that has a wide tuning range (1460 nm – 1640 nm), high wavelength accuracy, and high sweep speeds. For the simultaneous measurement of transmission and reflection, we used a dual-channel optical power sensor (Agilent 81635A). For a full-range sweep using a 0.01 nm resolution, the average measurement time (including the alignment) was about 2.5 minutes per device. With recent software and hardware updates, this setup can now work at about 0.6 minute per device [93]. The minimum resolution of the spectral measurements is 0.1 pm. As shown in Figure 2.15, the setup also has an RF probe that is used for the electrical testing of active devices such as modulators and detectors. A full view of the actual setup is shown in Figure 2.16.

The RF probe is connected to the network analyzer (Agilent PNA E8361A) to perform high-speed measurement of S-parameters. As shown in Figure 2.15,

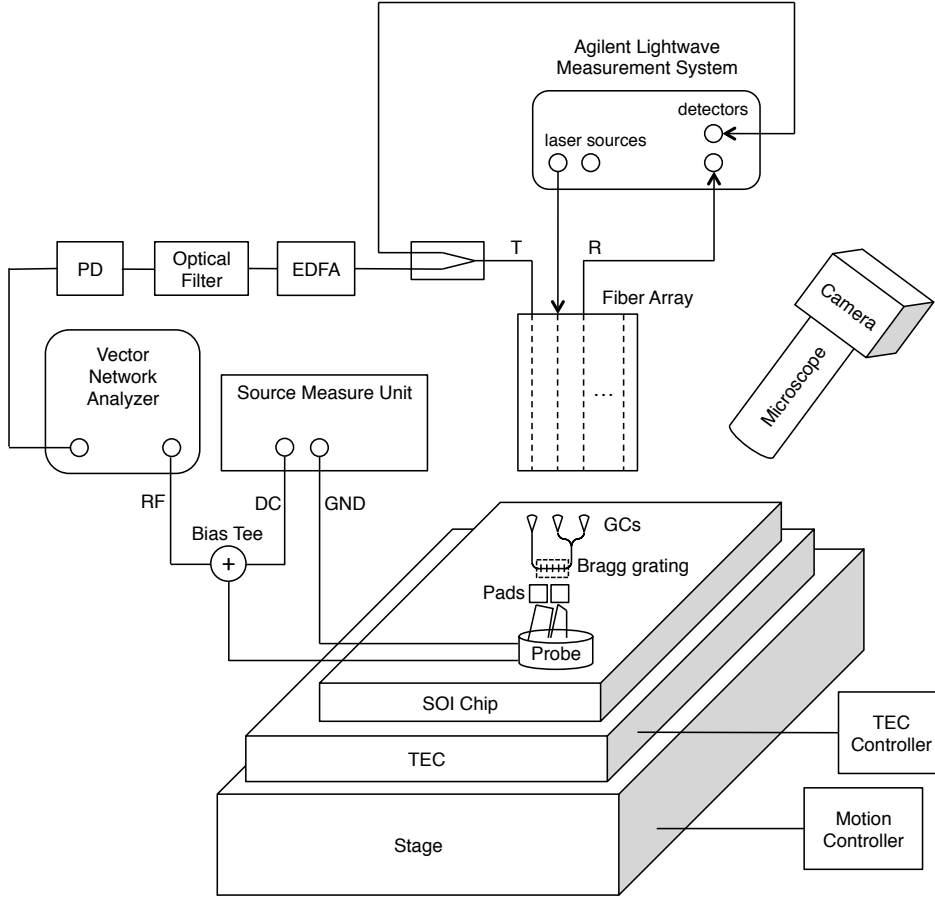


Figure 2.14: Block diagram of the advanced experimental setup. PD: photodetector, EDFA: erbium-doped fiber amplifier, TEC: thermoelectric cooler.

the copper plate under the chip can be thermally controlled; the red and black cables are connected to the temperature controller (SRS LDC501, see part 3 in Figure 2.16). Most of the measurement, however, was performed at room temperature, unless stated otherwise. A camera is affixed to the microscope, and Figure 2.17 shows a captured image during measurement. The multiple channels are clearly seen in the fiber array and are well aligned with the GCs on the chip.

We should point out that the tunable laser (Agilent 81600B) has two outputs: one with a high output power and the other with a low source spontaneous emission

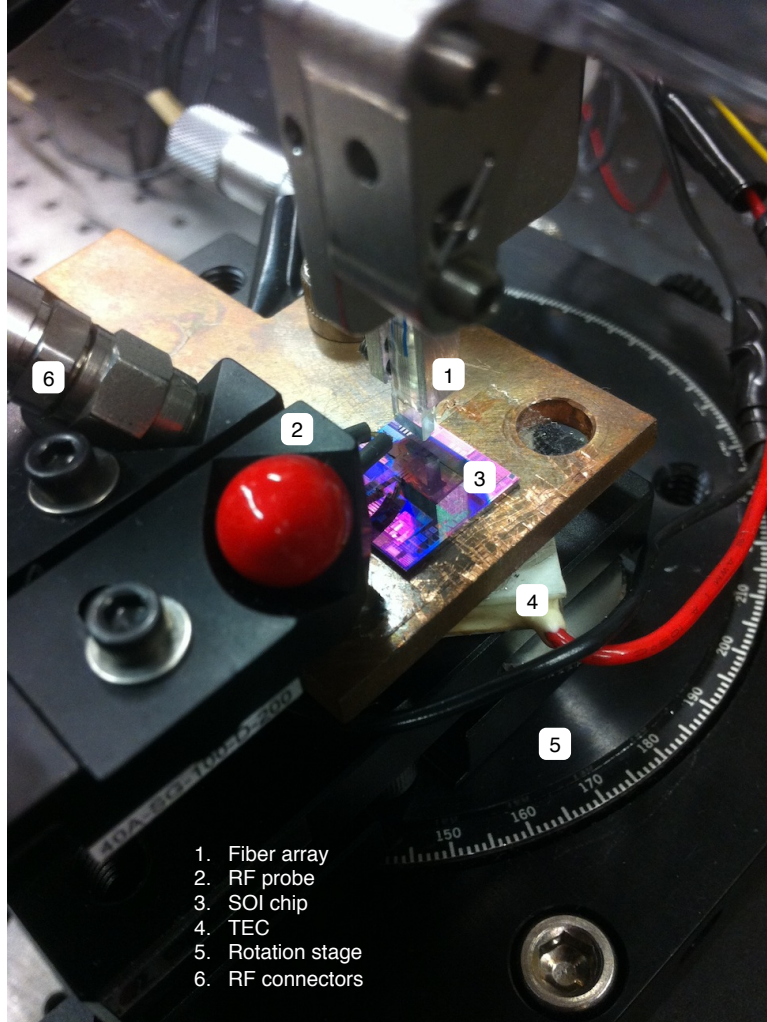
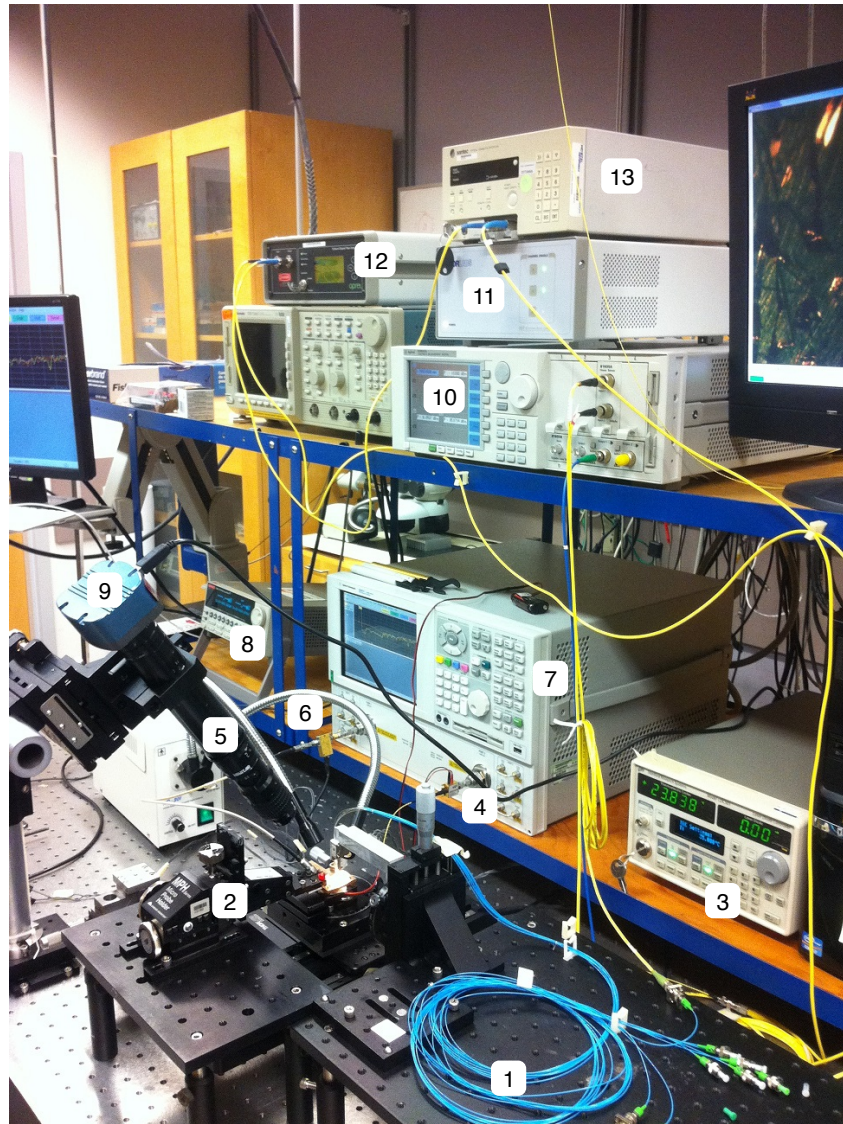


Figure 2.15: An advanced measurement setup using a fiber array.



- | | | |
|-----------------------|------------------------------------------|-----------------------------|
| 1. Fiber array | 6. Bias Tee | 11. Stage motion controller |
| 2. Micro probe holder | 7. Vector network analyzer | 12. EDFA |
| 3. TEC controller | 8. Source measure unit | 13. Optical filter |
| 4. Photodiode | 9. Camera | |
| 5. Microscope | 10. Agilent lightwave measurement system | |

Figure 2.16: Full view of the advanced measurement setup.

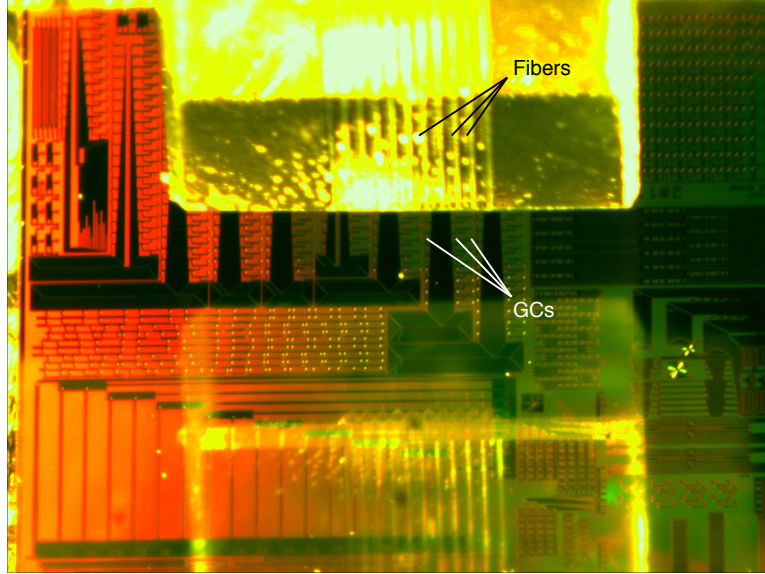


Figure 2.17: Captured image during experiment. The chip uses a layout similar to Figure 2.8, and the grating couplers are aligned with the fibers in the array.

(SSE). Bragg grating devices generally exhibit high extinction ratios. Therefore, it is necessary to choose the low SSE output of the tunable laser, which offers a high signal-to-SSE ratio and the large dynamic range needed to completely characterize the devices [94]. Figure 2.18(a) shows the measured transmission, using the low SSE option, of a straight waveguide without gratings, and a grating device with the following design parameters: $W = 500$ nm, $\Delta W = 80$ nm, $\Lambda = 325$ nm, and $N = 3000$. Note that overall envelope arises from the intrinsic response of the grating couplers [90]. When using the high power option, the stop band of the grating is cut off at around -51 dB, as shown in Figure 2.18(b). It is also surprising that the power slightly decreases versus the wavelength within the stop band, which is contrary to the response of the straight waveguide. Figure 2.18(c) also shows that for the same straight waveguide, the spectra using the two options are substantially different at the short wavelength range. This is because the laser power was set at 0 dBm but the maximum power of the low SSE output is actually less than 0 dBm

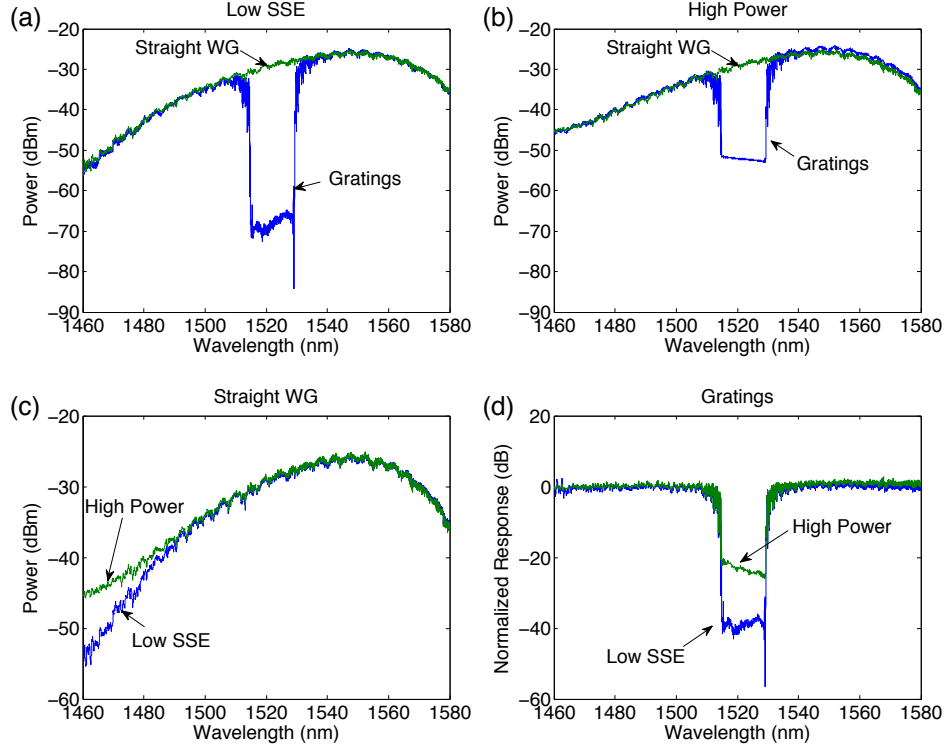


Figure 2.18: Measured transmission spectra of a straight waveguide (WG) and a Bragg grating using: (a) the low SSE option, and (b) the high power option. Comparison between the low SSE option and the high power option for: (c) the spectra of the straight waveguide, and (d) the normalized response of the grating by subtracting the spectra of the straight waveguide . Note that the laser output power was set to be 0 dBm (i.e., 1 mW).

at the short wavelength range, as shown in Table 2.1. The intrinsic response of the grating device is obtained by subtracting the response of the straight waveguide from the measured raw response of the grating, as shown in Figure 2.18(d). We can see that the extinction ratio is limited to only 20 dB by the high power option, whereas the low SSE option shows an extinction ratio of about 40 dB and many small details become uncovered.

Tunable lasers equipped with low SSE outputs are usually expensive. In case they are not available, changing the sweeping settings can help optimize the dy-

Output 1 (low SSE)	Output 2 (high power)
$\geq +3$ dBm peak (typical)	$\geq +9$ dBm peak (typical)
$\geq +2$ dBm peak (1520 nm to 1610 nm)	$\geq +8$ dBm peak (1520 nm to 1610 nm)
≥ -2 dBm peak (1475 nm to 1625 nm)	$\geq +4$ dBm peak (1475 nm to 1625 nm)
≥ -7 dBm peak (1455 nm to 1640 nm)	≥ -1 dBm peak (1455 nm to 1640 nm)

Table 2.1: Maximum output power (continuous power during sweep) of Agilent 81600B Option 201 [1].

namic range of the measurement. Figure 2.19 shows the measured spectra using the high power option of the tunable laser under 4 different sweeping conditions. First, the laser output power was set at 0 dBm. We performed the wavelength sweep using two methods: (1) a full-range continuous sweep and (2) a segmented sweep that consists of 10 segments. We can see that there is little difference between these two measurements. Then we set the laser output power at 10 dBm and re-run the wavelength sweep using the two methods. We observe that the measured power is indeed higher but not as much as 10 dB. This is due to the fact that the maximum output power of the laser is actually 9 dBm and is wavelength dependent, as shown in Table 2.1. For the segmented sweep, we can see that the power is increased by 9 dB around 1550 nm but less than 4 dB at 1470 nm, which agrees with the laser specifications in Table 2.1. For the continuous sweep, the spectrum discontinuity disappears but at the expense of reduced power, because the laser power is almost kept constant at the starting point of the sweep. Finally, the stop band is always cut off at around -51 dB, confirming that the dynamic range is limited by the laser noise. In short, if the integrity of the broad band response is important (e.g., the overall response of the grating coupler), users should choose an output power that can be reached all over the sweep range (in the above case, the setting is 0 dBm). However, if the narrow band dynamic range is more critical (e.g., to reveal the features at the bottom of the stop band of the gratings), one could use the highest output power (in the above case, the setting is 10 dBm).

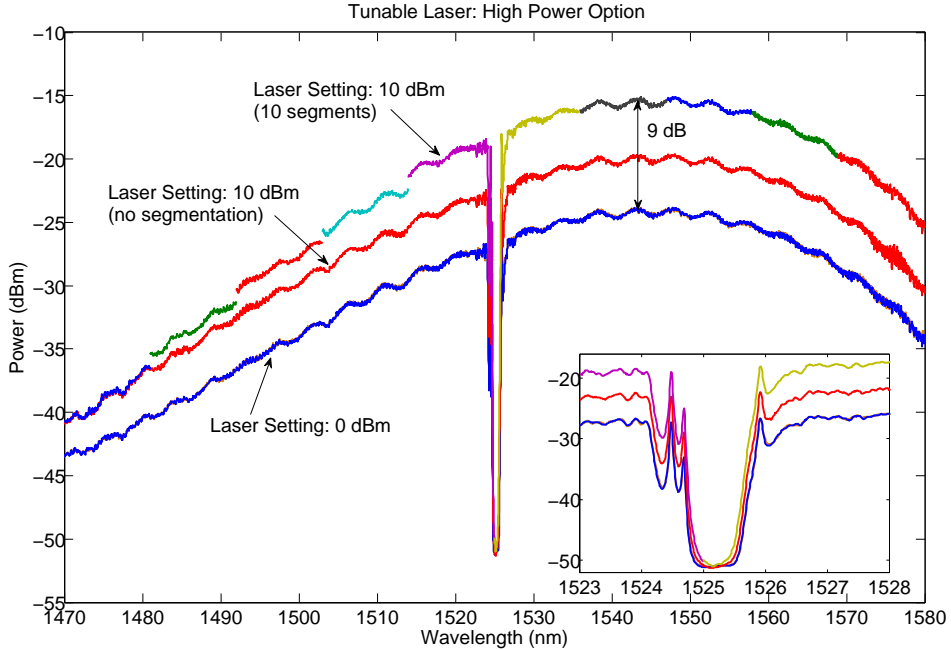


Figure 2.19: Measured transmission spectra of a Bragg grating using the high power option under various sweeping conditions. Inset shows the zoom-in view around the Bragg wavelength. The small ripples out of the stop band are due to the FP effects in the measurement system.

2.2.5 Design Variations

In this section, we discuss a number of variations that are fundamental to a uniform grating design.

2.2.5.1 Grating Period

Based on the Bragg condition (i.e., Eq. 1.1), we expect that the Bragg wavelength would increase with increasing grating period. This was observed experimentally. Figure 2.20 shows the measured transmission spectra for three gratings with different periods: 320 nm, 325 nm, and 330 nm. The increment in the Bragg wavelength is about 12.6 nm. Note that there is a common, but inaccurate, formula to calculate the wavelength shift: $\Delta\lambda = (\Delta\Lambda/\Lambda)\lambda$, which gives a $\Delta\lambda$ of larger than 23 nm in

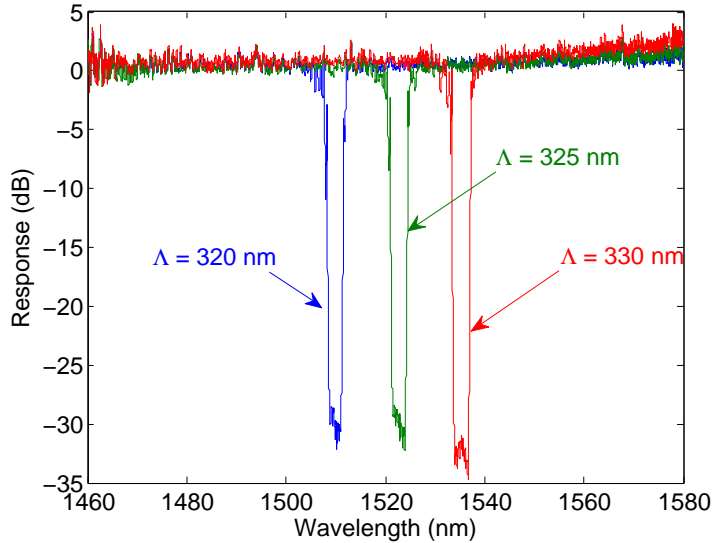


Figure 2.20: Measured transmission spectra for gratings with different grating periods, showing the red shift with increasing grating period. Fixed parameters: air cladding, $W = 500$ nm, $\Delta W = 20$ nm, $N = 1000$.

this case. However, this formula misses the fact that n_{eff} is wavelength dependent, and therefore, the group index should be taken into account somehow. Here is a more accurate approximation:

$$\frac{d\lambda}{d\Lambda} = \frac{\lambda}{\Lambda} \cdot \frac{n_{eff}}{n_g} = \frac{\lambda^2}{2\Lambda^2 n_g} \quad (2.1)$$

which essentially adds another factor of n_{eff}/n_g so that the dispersion effect is taken into account. For a regular strip waveguide, n_{eff} is usually smaller than n_g (for this particular waveguide: $n_g = 4.36$). Based on Eq. 1.12, this indicates that n_{eff} decreases as wavelength increases. Figure 2.21 shows the measured Bragg wavelength as a function of the grating period. The linear curve fitting shows that $d\lambda/d\Lambda$ is 2.53, which closely matches with the calculated value of 2.515 using Eq. 2.1.

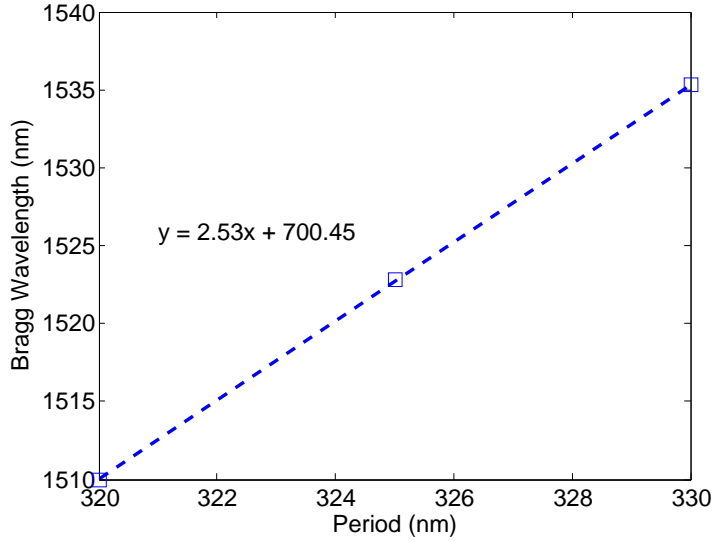


Figure 2.21: Bragg wavelength extracted from Figure 2.20 versus grating period. The slope of the linear curve fit is 2.53, which is in good agreement with the calculation using Eq. 2.1.

2.2.5.2 Corrugation Width

The corrugation width determines the coupling coefficient (κ) and thus the bandwidth of a grating. Figure 2.22 shows the measured transmission spectra for various corrugation sizes from 10 nm to 160 nm on a 500 nm waveguide with air cladding. The bandwidth is plotted versus the corrugation width in Figure 2.23, showing an approximately linear relationship with a slope of about 0.18.

2.2.5.3 Waveguide Width

The coupling coefficient (κ) depends not only on the corrugation width but also on the waveguide width. Figure 2.24 shows the measured transmission spectra of two devices that have the same corrugation width but different waveguide width, one is 500 nm and the other is 450 nm. We can see that the bandwidth is larger on the narrower waveguide, because the interaction between the sidewall corrugation and the optical mode becomes stronger. As can be seen in Figure 2.25, the field intensity around the sidewall of the 450 nm waveguide is stronger than that of the

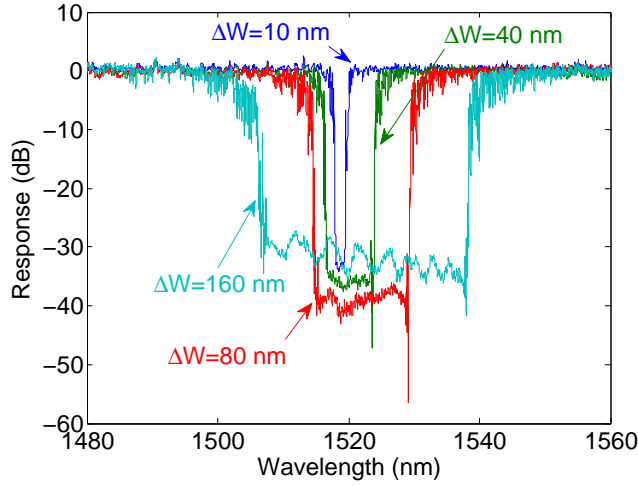


Figure 2.22: Measured transmission spectra for various corrugation widths, showing the bandwidth increases with increasing corrugation width. Fixed parameters: air cladding, $W = 500$ nm, $\Lambda = 325$ nm, and $N = 3000$.

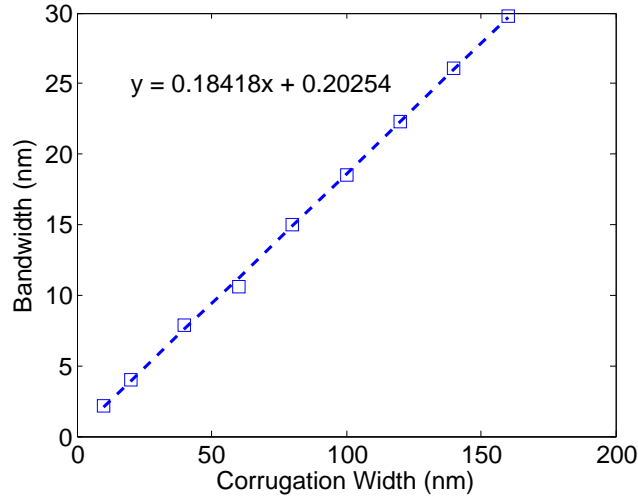


Figure 2.23: Measured bandwidth versus corrugation widths on 500 nm strip waveguide with air cladding. The data points for 10 nm, 40 nm, 80 nm, and 160 nm corrugations correspond to the spectra in Figure 2.22. The linear fit shows that the coupling coefficient (i.e., grating index contrast) is approximately proportional to the corrugation width.

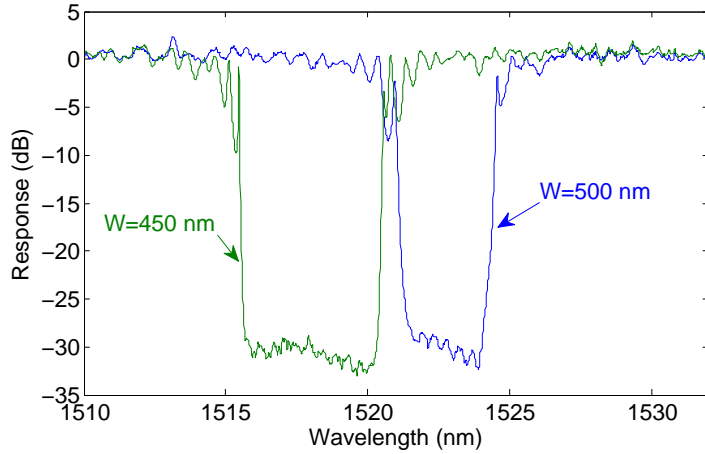


Figure 2.24: Measured transmission spectra for gratings with 20 nm corrugation on a 500 nm waveguide and on a 450 nm waveguide. Fixed parameters: air cladding, $\Delta W = 20$ nm and $N = 1000$. The period for the 500 nm waveguide and the 450 nm waveguide is 325 nm and 340 nm, respectively.

500 nm waveguide.

Figure 2.26 plots the bandwidth versus the corrugation width for gratings on the two waveguides. Again, we see that the bandwidths are larger on the 450 nm waveguide. Also, the linear relationship remains for the 450 nm waveguide, with a larger slope of about 0.25.

2.2.5.4 Cladding

All results in the previous three sections are for devices with air cladding. In this section, we will present more results of devices with oxide cladding. Figure 2.27 shows the spectra for two devices that have exactly the same parameters except for the cladding. We see that the device with oxide cladding has a longer Bragg wavelength due to the increased effective index; meanwhile, its bandwidth is smaller because the index contrast is reduced.

Figure 2.28 shows the measured bandwidth as a function of the corrugation width for oxide-cladding devices, compared with air-cladding devices. The slope for oxide cladding is about 0.12, which is 1.5 times smaller than that for air cladding.

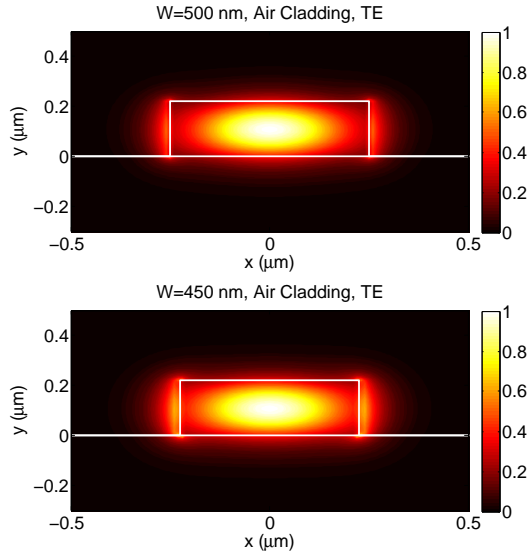


Figure 2.25: Simulated electric field of the fundamental TE mode in a 500 nm (top) and a 450 nm (bottom) strip waveguide, both with air cladding. The field intensity around the sidewall of the 450 nm waveguide is stronger than that of the 500 nm waveguide.

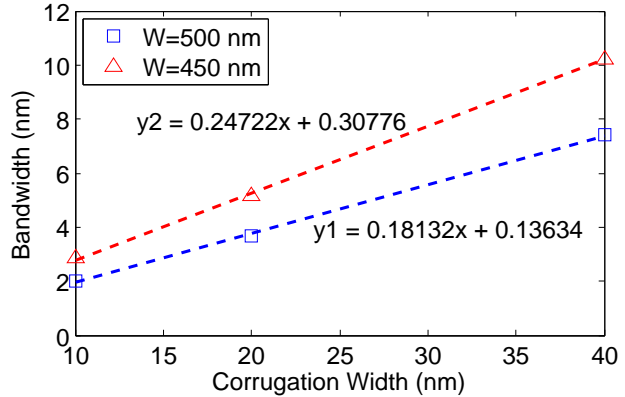


Figure 2.26: Measured bandwidth as a function of corrugation width on 500 nm (blue) and 450 nm (red) strip waveguides with air cladding. The gratings on narrower waveguide show larger bandwidths and a larger slope in the linear fit, due to increased modal overlap with the sidewalls.

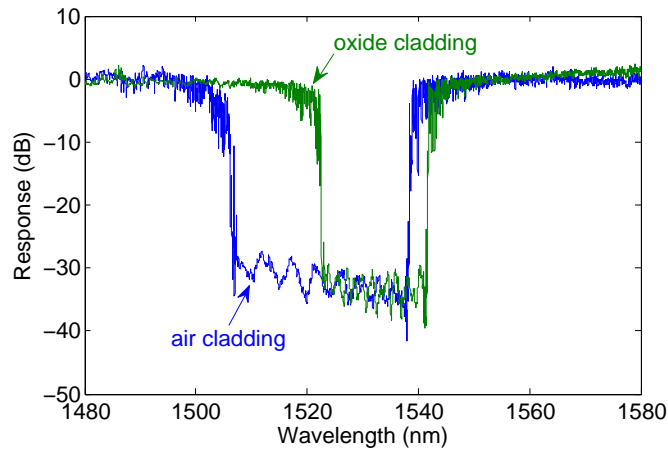


Figure 2.27: Measured transmission spectra for gratings with air cladding (blue) and with oxide cladding (green). For the oxide-clad device, the wavelength is longer due to the larger average effective index and the bandwidth is smaller due to the reduced index contrast. Fixed parameters: $W=500$ nm, $\Delta W=160$ nm, $\Lambda=325$ nm, $N=3000$.

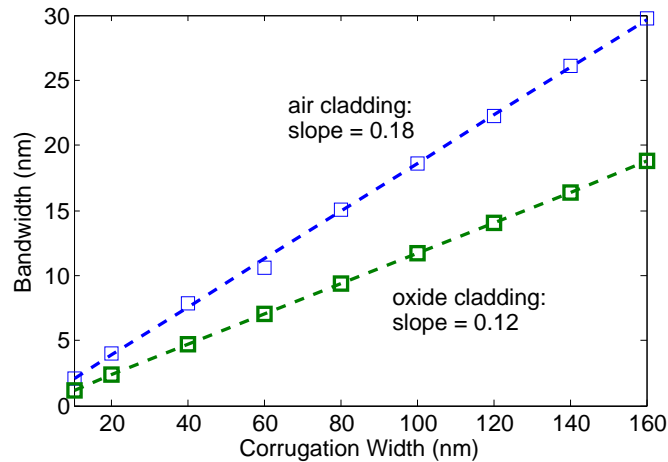


Figure 2.28: Measured bandwidth as a function of corrugation width on 500 nm strip waveguide with air cladding (blue) and with oxide cladding (green). The gratings with oxide cladding show smaller bandwidths and a smaller slope in the linear fit, due to the reduced index contrast.

2.2.5.5 Length

The propagation loss is an important figure-of-merit for a grating waveguide. It not only leads to the insertion loss in the transmission but also limits the maximum reflectivity. As will be discussed in Section 2.6, the propagation loss is also critical for grating cavities. To extract the propagation loss using the cutback method, we designed gratings with various lengths. As shown in Figure 2.29, we do observe a slight decrease of power in the out-of-band transmission when the grating number is increased from 3000 to 15000. However, the decrease is very small (comparable to the alignment error of the measurement) and the noise becomes more significant. Therefore, it is difficult to obtain an accurate propagation loss value from these data. At a rough estimate, the propagation loss is within the range of 2.5–4.5 dB/cm, comparable to that of a straight waveguide without gratings. We also observe that the propagation loss is independent of the corrugation width (at least for the range that we used: 10 nm to 80 nm).

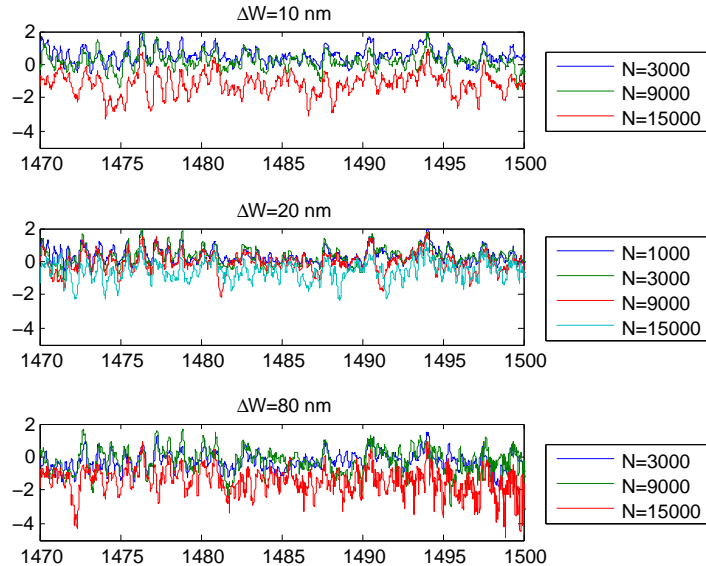


Figure 2.29: Measured out-of-band transmission spectra for gratings with various corrugation widths and lengths. Fixed parameters: air cladding, $W = 500$ nm, $\Lambda = 325$ nm. The propagation loss is within the range of 2.5–4.5 dB/cm and is independent of the corrugation width.

Theoretically, as the length is increased, the bandwidth should not increase, and actually, the bandwidth may decrease if the coupling is very weak, see Eq. 1.16. On the contrary, we experimentally observe that the stop band gets broader when the grating gets longer, as shown in Figure 2.30 and Figure 2.31 .

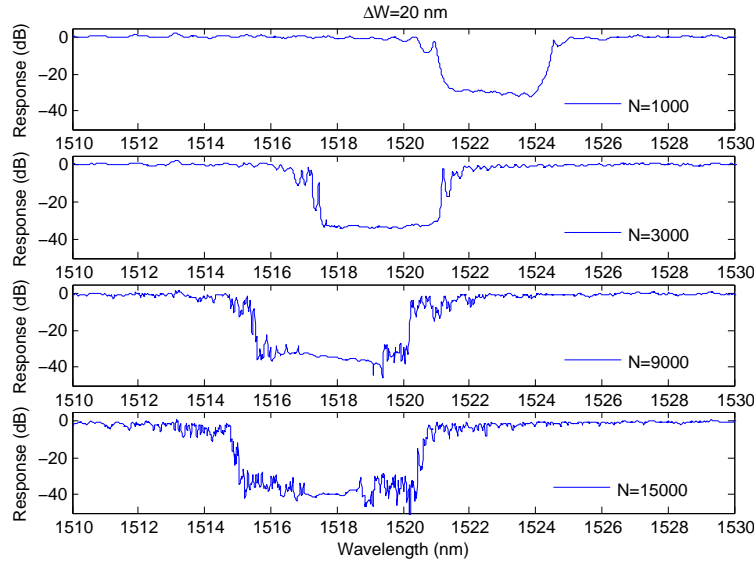


Figure 2.30: Measured transmission spectra of gratings with 20 nm corrugation width for various lengths, showing bandwidth broadening effect with increasing N and wavelength variations due to fabrication variations. Fixed parameters: air cladding, $W = 500 \text{ nm}$, $\Lambda = 325 \text{ nm}$.

For example, as shown in Figure 2.30, when N is 1000, the transmission spectrum is very clean and resembles an ideal grating response. When N is 3000, the stop band begins to have some irregular ripples while the bandwidth is approximately the same. When N is 9000 and above, the noises become significant and the bandwidth becomes larger. This is primarily due to the top Si thickness variations (i.e., the strip thickness varies along the waveguide so that the effective index fluctuate). For simplicity, we consider Si only as the top Si layer later on. Also worth mentioning is that the Bragg wavelength is shifting, again due to the Si thickness variations. Note that for each N , the devices are packed together, whereas for different N , the devices are placed far apart. Presumably, the Si thickness variation

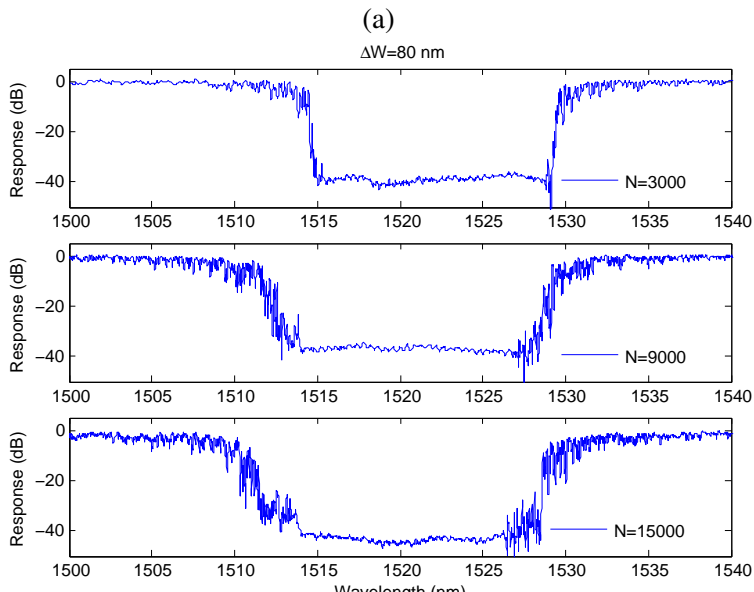
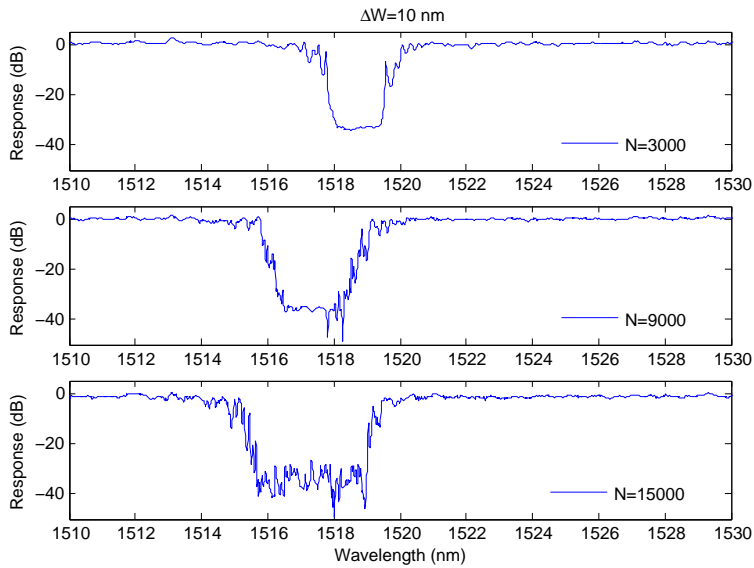


Figure 2.31: Measured transmission spectra of gratings with (a) 10 nm and (b) 80 nm corrugation width for various lengths, showing similar trends as Figure 2.30. Fixed parameters: air cladding, $W = 500 \text{ nm}$, $\Lambda = 325 \text{ nm}$.

is small within a small area, therefore, the Bragg wavelength shifts in a similar manner from N=3000 to N=15000 in Figure 2.30 and Figure 2.31. Keep in mind that the Si thickness variation is random though, as will be further discussed in Section 3.5. The blue shift in Figure 2.30 and Figure 2.31 is just a special case.

2.2.5.6 Shape

So far, we have only discussed gratings that use rectangular corrugations. In addition, we have also designed gratings with trapezoidal and triangular corrugations, as illustrated in Figure 2.32 [95]. As discussed in Section 1.2, the coupling coefficient can be obtained from the first-order Fourier component of the grating profile.

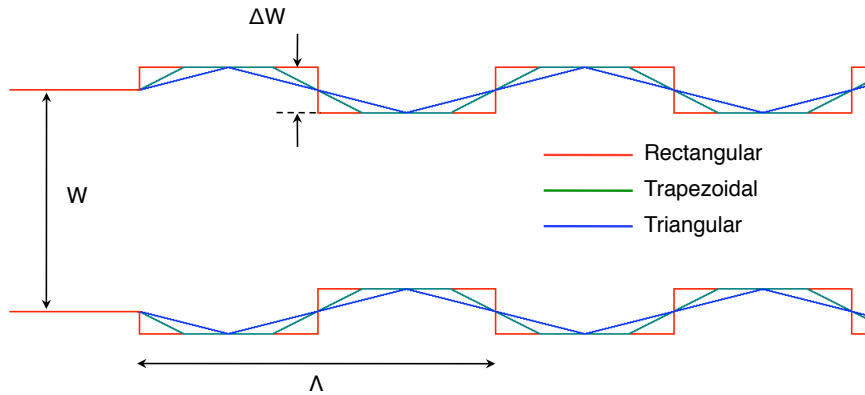


Figure 2.32: Schematic illustration of corrugation shapes (not to scale).

Therefore, for the same corrugation width, we can obtain the following relationships:

$$\kappa_{Tra} = \kappa_{Rec} \cdot \frac{2\sqrt{2}}{\pi} \quad (2.2)$$

$$\kappa_{Tri} = \kappa_{Rec} \cdot \frac{2}{\pi} \quad (2.3)$$

Figure 2.33 shows the measured bandwidth for the three shapes. The ratio between the slopes of the three curves is 1:0.88:0.66, which agrees very well with the above analysis. However, for the sake of simplicity, we will keep using rectangular corrugations in the remainder of this thesis.

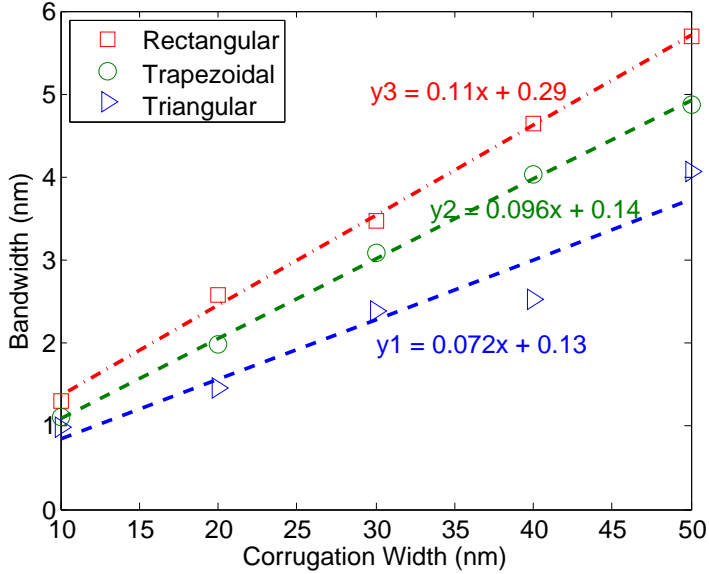


Figure 2.33: Measured bandwidth as a function of corrugation width for different shapes. Fixed parameters: oxide cladding, $W = 500$ nm, $\Lambda = 320$ nm, $N = 2000$. The bandwidth and the slope of the linear fit become smaller as the shape goes from rectangular to trapezoidal to triangular, due to the reduced Fourier component and coupling coefficient.

2.3 Lithography Effects ¹

Due to the high refractive index contrast, most silicon photonic devices are highly sensitive to dimensional variations and require high-resolution fabrication processes. As previously mentioned, electron-beam lithography has been used extensively for fabrication in research, but it is unsuitable for commercial applications. Alternatively, DUV lithography, especially at 193 nm [96], has been proven to be capable of making high-quality photonic devices in silicon, and, more importantly, it is CMOS-compatible and can be used for high-volume production. However, with DUV lithography, it is difficult to optimize the illumination settings

¹A version of Section 2.3 has been published: X. Wang, W. Shi, M. Hochberg, K. Adams, E. Schelew, J. Young, N. Jaeger, and L. Chrostowski, “Lithography simulation for the fabrication of silicon photonic devices with deep-ultraviolet lithography,” in *Group IV Photonics*, San Diego, CA, August 2012, pp. 288-290.

for various types of patterns simultaneously, e.g., the settings that are optimized for isolated structures such as photonic wires are usually not ideal for dense structures such as photonic crystals [96]. Moreover, researchers are developing devices with feature sizes that are even smaller than the resolution limit. In particular, integrated waveguide Bragg gratings suffer from serious lithographic distortions. Therefore, it is important to include the effects of the fabrication process in the design flow so that they are properly accounted for [97]. Image distortions that happen during fabrication of electronic circuits in CMOS advanced processes are routinely corrected, but such corrections may not be compatible with the significantly different and more diverse structures that are encountered in silicon photonics circuits.

In this section, we propose a model to predict the fabrication imperfections of silicon photonic devices during the lithography process. After lithography simulation, we simulate the spectral responses of the virtually fabricated grating devices, and we obtain good matching between the simulation and experimental results.

First, we chose a device to calibrate the lithography model so that the post-lithography simulation fit the experimental data. Then, the model is fixed for all other devices. Here, the device used for calibration is a 500 nm strip waveguide grating designed with 40 nm rectangular corrugations (named as device A). To implement the lithography simulation, we use a commercial tool that has been widely used in the microelectronics industry – Mentor Graphics Calibre [89]. For the optical system, we use a conventional circular illumination source. The numerical aperture (NA) and the partial coherence factor (σ) are the key parameters that determine the corrugation distortions; we use $NA = 0.6$ and $\sigma = 0.6$ in our simulations. Note that these parameters were not provided by the foundry, but were estimated so that the post-lithography simulation fit the experimental data for device A and were then fixed for all other devices. Also, these parameters are within the range defined by the stepper’s technical specifications. Figure 2.34 shows the simulation results for device A. We can see that the corrugations are greatly smoothed, and their effective amplitudes are also reduced.

After lithography simulation, we simulate the spectral responses of the virtually fabricated grating devices using a three-dimensional (3D) finite-difference time-domain (FDTD) method [84], and then compare them with the original design as well as the measurement results of the devices actually fabricated. Figure 2.35

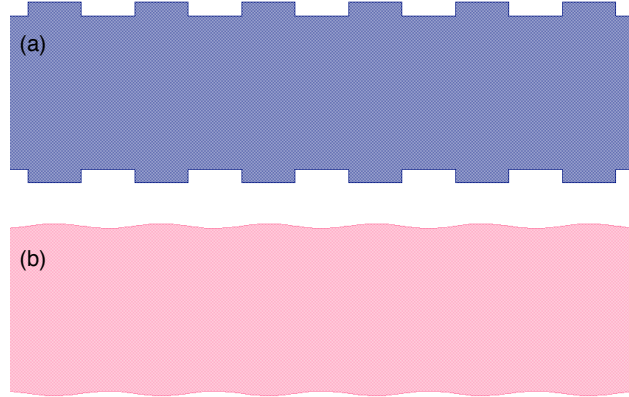


Figure 2.34: Lithography simulation for device A: (a) original design, (b) simulation result.

shows the transmission spectra for device A. It can be seen that the original de-

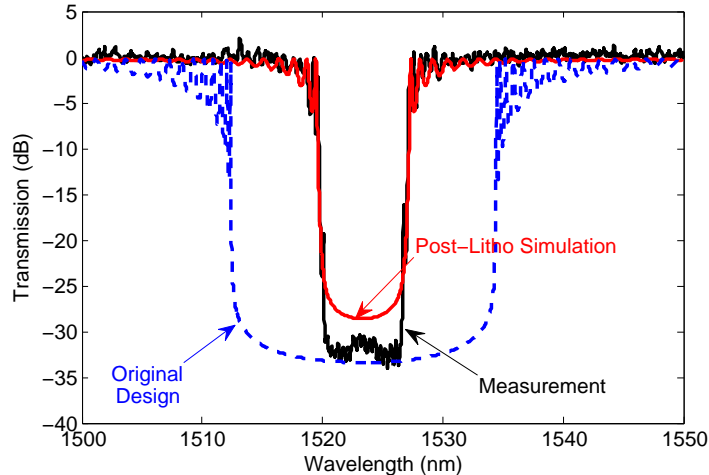


Figure 2.35: Spectral comparison (transmission) for device A. Original design: FDTD simulation using the structure in Figure 2.34(a), post-litho simulation: FDTD simulation using the structure in Figure 2.34(b).

sign has a bandwidth of about 23 nm, in contrast, the post-litho simulation shows a much narrower bandwidth of about 8 nm. Note that the thickness of the waveguide

was slightly reduced by a few nanometers in the simulation in order to match the Bragg wavelength, which has little effect on the bandwidth. The amplitude mismatch between the measurement and post-litho simulation is partially due to the calibration errors (e.g., the ripples in Figure 2.19).

Figure 2.36 plots the simulated and measured bandwidths versus the designed corrugation widths. Again, the post-litho simulation agrees very well with the measurement, whereas the mismatch between the original design and the measurement is very large. As a rule of thumb, the actual bandwidth is about 3x smaller than the original design value.

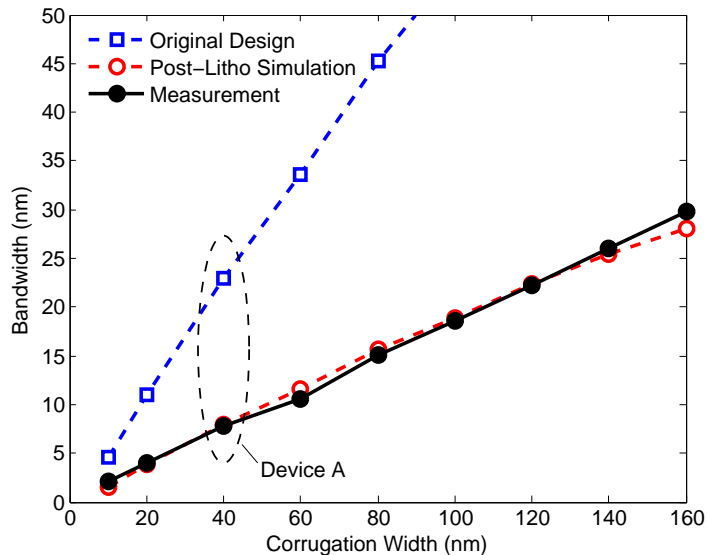


Figure 2.36: Bandwidth versus corrugation width on 500 nm strip waveguides with air cladding. The post-litho simulation agrees well with the measurement result, while the original designs show bandwidths of about three times larger.

This technique can be applied to many other silicon photonic devices, especially ones that are sensitive to lithographic distortions. For example, Figure 2.37 shows the simulation result for a photonic crystal cavity. We can see that the simulated bulk holes are smaller than the designed ones, therefore, a bias should be applied to the bulk holes in the mask to obtain the desired hole sizes. Due to the

optical proximity effect, the edge holes are smaller than the bulk holes [96], and the displacement of the two cavity side holes introduces extra distortions. Therefore, differential bias needs to be applied to the holes next to the cavity, and this cannot be easily done without lithography simulations.

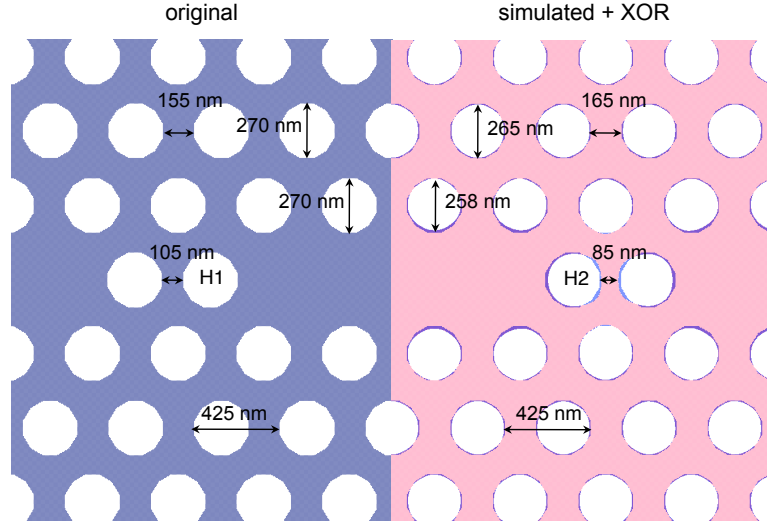


Figure 2.37: Lithography simulation for a photonic crystal cavity with three missing holes in the centre. XOR: Boolean operation of XOR (exclusive or) between the original and simulated layouts. The two cavity side holes (H1 and H2) are displaced in order to achieve a high Q-factor.

We believe that this work is an important step in the direction of design-for-manufacturing in the field of silicon photonics. Note that this work only considers the optical model (the light incident on the photoresist) [98]. There are, of course, many other physical effects that need to be accounted for, e.g., the photoresist model, the etching process, and the Si thickness variations. Fortunately, the development of silicon photonic fabrication can benefit greatly from the vast library of knowledge that already exists in the microelectronics industry, as well as the continued advancements. Specifically, we believe that this model could be improved by using test patterns in EDA tools such as Mentor Graphics Calibre [89].

2.4 Thermal Sensitivity

Most silicon photonic devices are highly sensitive to temperature variations on the chip, due to the large thermo-optic coefficient of silicon. In this section, we study the thermal sensitivity of strip waveguide gratings. As previously shown in Figure 2.15 and Figure 2.16, the silicon chip can be thermally controlled using the temperature controller.

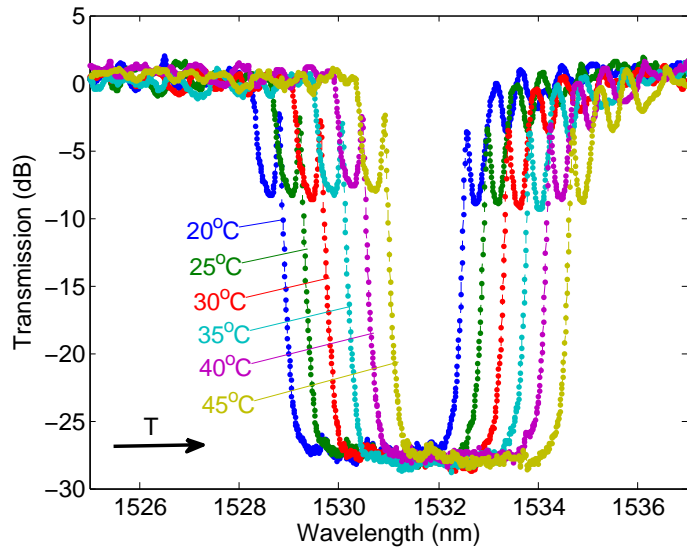


Figure 2.38: Measured transmission spectra of a strip waveguide grating at different temperatures, showing the red shift with increasing temperature. The design parameters are: air cladding, $W = 500$ nm, $\Delta W = 20$ nm, $\Lambda = 330$ nm, and $N = 1000$.

Figure 2.38 shows the transmission spectra of a strip waveguide grating at different temperatures. Clearly, the Bragg wavelength shifts to longer wavelengths as the temperature is increased. Figure 2.39 plots the Bragg wavelength versus the temperature, showing a linear slope of about $84 \text{ pm}^{\circ}\text{C}$.

By taking the derivative of Eq. 1.1 with respect to temperature, we obtain:

$$\frac{d\lambda}{dT} = \frac{\lambda}{n_g} \frac{dn_{eff}}{dT} = \frac{\lambda}{n_g} \frac{dn_{eff}}{dn} \frac{dn}{dT} \quad (2.4)$$

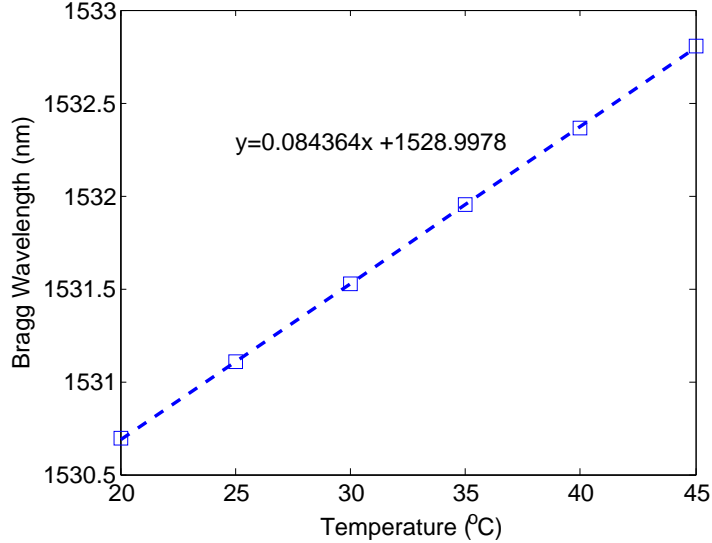


Figure 2.39: Bragg wavelength versus temperature corresponding to the measured spectra in Figure 2.38, showing a thermal sensitivity of about 84 pm/°C.

where the thermo-optic coefficient in silicon is [99]:

$$\frac{dn}{dT} = (1.86 \pm 0.08) \times 10^{-4}/K \quad (2.5)$$

Using Eq. 2.4, the simulated thermo-optic dependence of the Bragg wavelength is about 80 pm/°C, in good agreement with the measurement result.

2.5 Wafer-Scale Performance

One of the major issues with silicon photonics is that most devices are sensitive to dimensional variations, including waveguide width variations caused during the lithography process as well as thickness variations of the top silicon layer caused during the manufacturing of the SOI wafer. These variations can be present either at the device scale (1–100 μm), chip scale (1–20 mm) or wafer scale (150 mm–300 mm). Typically, local variations at the device or chip scale (1 nm) are much smaller than the global variations found across a full wafer (10 nm) [100]. To make

waveguides more robust to dimensional variations, one can increase the waveguide dimensions or use the less confined TM-polarization, however, both approaches require much larger bending radius. Post-fabrication trimming is a technique to compensate the fabrication variations [101], but at the expense of increased fabrication complexity and costs. Alternatively, active components (e.g., thermal tuning) can be used for accurate compensation, however, this approach leads to higher power consumption and increased circuit complexity. Therefore, it is still necessary to improve the uniformity of passive devices to a practical level. Selvaraja et al. demonstrated the nonuniformity of ring resonators, Mach–Zehnder interferometers, and arrayed waveguide gratings, showing a nonuniformity in the spectral response of <0.6 nm within a chip and <2 nm between chips [100]. Zortman et al. used microdisk resonators to extract thickness and width variations from the resonant wavelength deviations, which were within 0.85 nm on a single die and 8 nm across the wafer [102].

In this section, we present the wafer-scale nonuniformity of our strip waveguide grating devices. As a part of a multi-project run, the grating devices are replicated on two 200 mm wafers, one with air cladding (Wafer A) and the other with oxide cladding (Wafer B). Each wafer contains many chips (or dies) arranged in columns and rows, as shown in Figure 2.40. The size of a chip is 12.73×12.95 mm².

There are two etch processes in the fabrication. The first etch is a 70 nm partial (shallow) etch for fiber grating couplers and rib waveguides. The second etch is a 220 nm full etch for strip waveguides, photonic crystals, etc. For the deep etch process, the exposure dose across the wafer is increased from left to right for research purposes [96]. This results in a reduction in width for strip waveguides (and an increase in hole size for photonic crystals) from column -4 to column 2; therefore, this is an intentional fabrication variation. As will be discussed in the next Chapter about rib waveguide gratings, the exposure dose for the partial etch is fixed, so the shallow-etched structures are supposed to be on target everywhere across the wafer.

To evaluate the device nonuniformity across the wafer, we chose a grating sample with the following design parameters: $W = 500$ nm, $\Delta W = 20$ nm, $\Lambda = 330$ nm, and $N = 1000$. Figure 2.41, Figure 2.42, and Figure 2.43 show the performance nonuniformity on Wafer A and Wafer B, respectively.

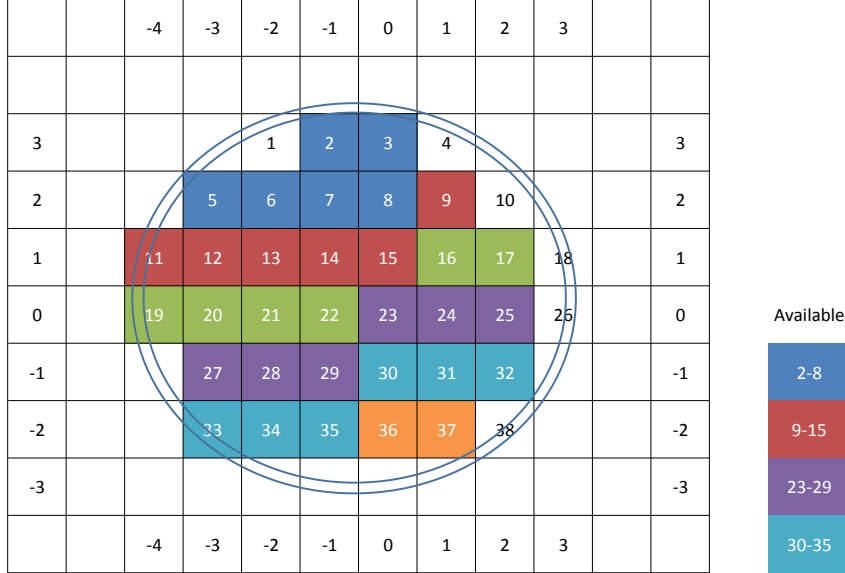


Figure 2.40: Wafer map (available chips are listed in the legend).

We can observe the following:

- Wavelength: The wavelength variation is remarkably large, i.e., >30 nm on both wafers. The average wavelength on Wafer B is about 11 nm larger than that on Wafer A, due to the higher index of the cladding. Moreover, the two wafers show a similar trend that the wavelength decreases from left to right columns. This agrees with the intentional exposure dose variation, i.e., the waveguide width decreases and thus the effective index becomes smaller.
- Bandwidth: The bandwidth variation is also noteworthy. On Wafer A, the average bandwidth is about 4.24 nm and the variation is about 1.17 nm. On Wafer B, the average bandwidth gets smaller to 2.92 nm, due to the weaker index contrast as discussed in Section 2.2.5.4; and the variation also gets smaller to 0.33 nm. Moreover, the two wafers show a similar trend that the bandwidth increases from left to right columns. This also agrees with the intentional exposure dose variation, i.e., the waveguide width decreases and thus the coupling becomes stronger as discussed in Section 2.2.5.3.

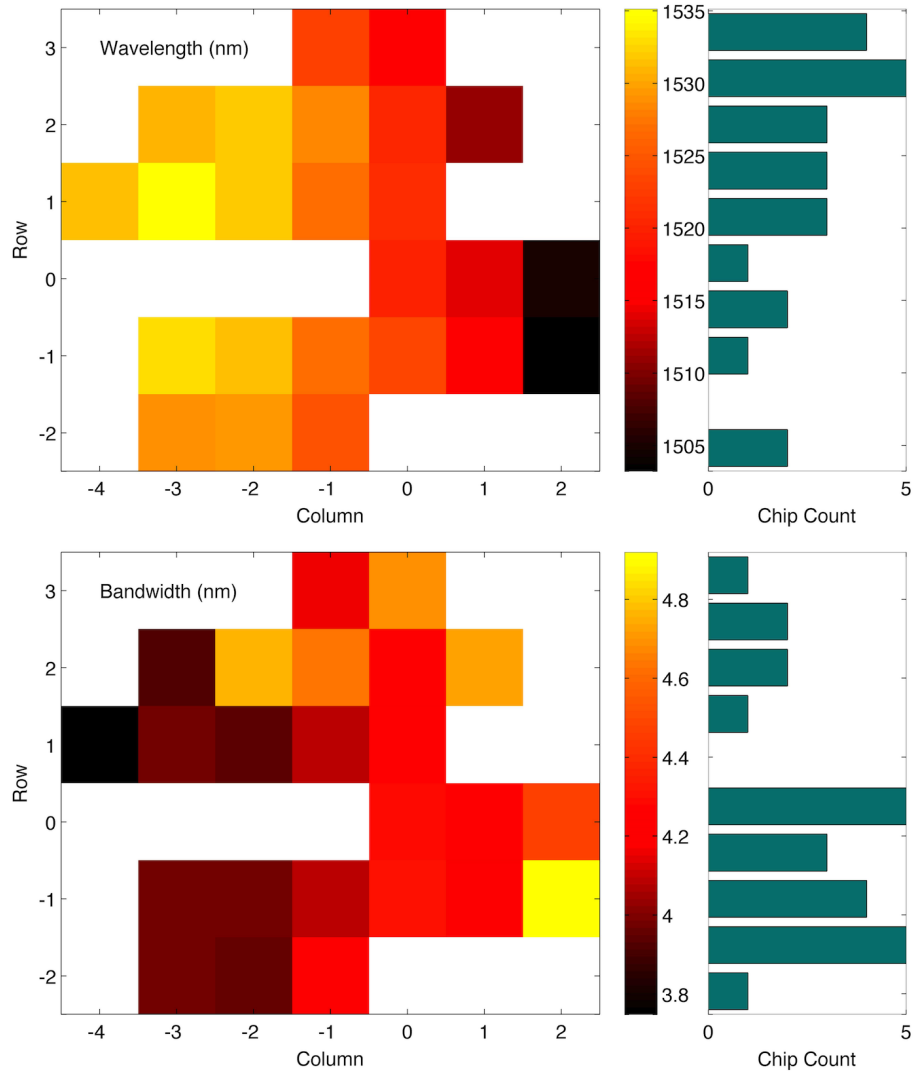


Figure 2.41: Performance nonuniformity of the strip waveguide grating on Wafer A.

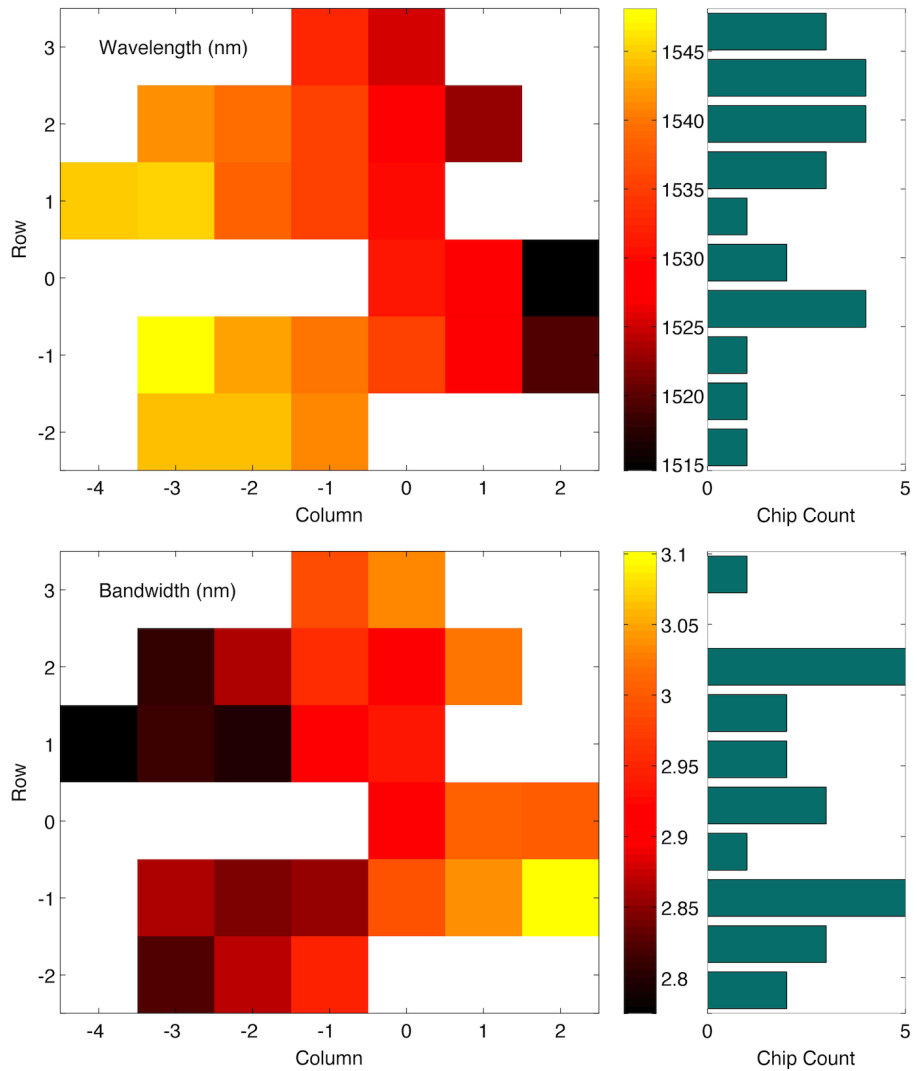


Figure 2.42: Performance nonuniformity of the strip waveguide grating on Wafer B.

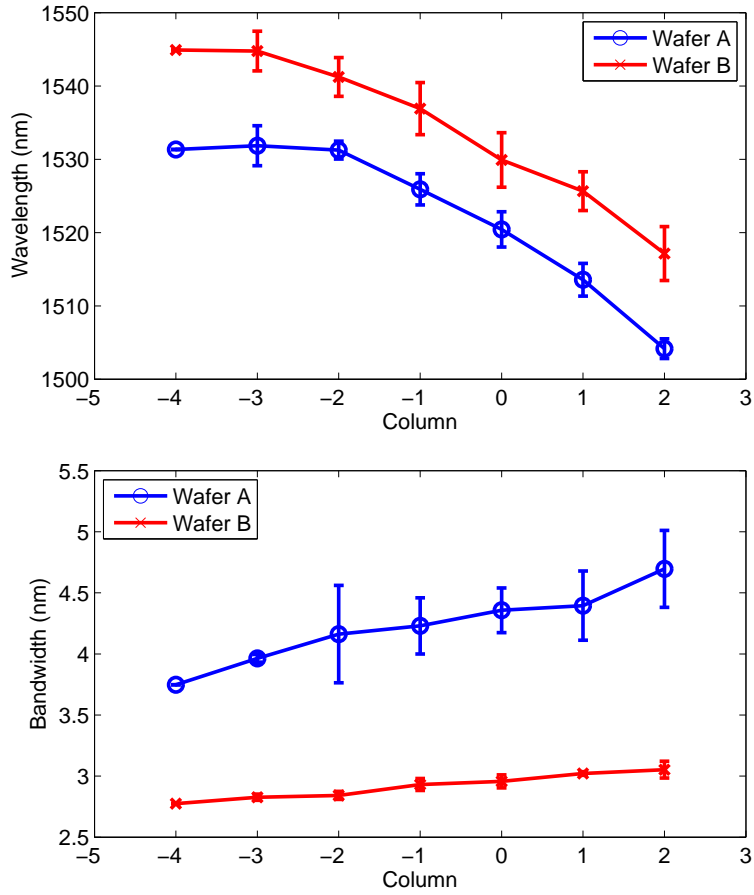


Figure 2.43: Performance nonuniformity of the strip waveguide grating as a function of the column number. Each error bar is symmetric and the length is two standard deviations (within each column). The general trend of the decrease in wavelength and the increase in bandwidth is due to the intentional increase in exposure dose from left to right columns.

In addition to the intentional waveguide width variations, the Si thickness variations also play a key role in the overall uniformity. For example, the devices in the same column also show random wavelength variations that cannot be predicted. We will discuss Si thickness variations in more detail in Chapter 3.

2.6 Phase-shifted Gratings²

2.6.1 Basics

We know that a uniform grating has a stop band around the Bragg wavelength in the transmission spectrum. If a phase shift is introduced in the middle of the gratings, as illustrated in Figure 2.44, a narrow resonant transmission window will

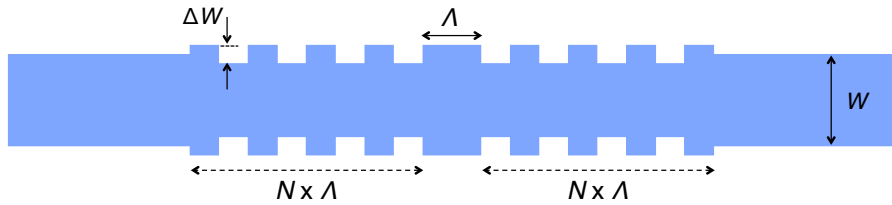


Figure 2.44: Schematic of a phase-shifted strip waveguide grating.

appear within the stop band, as shown in Figure 2.45. This structure can also be viewed as an FP cavity – the etalon is as thin as the phase shift, and the front grating section and the rear grating section act as mirrors of the FP etalon [103]. Figure 2.46 shows a fabricated strip waveguide phase-shifted grating. This grating can be used as a simple band-pass transmission filter, or in semiconductor lasers to enable single frequency operation [67]. The transmission window has a very narrow Lorentzian line shape. The position and the size of the phase shift determine the center wavelength and the sharpness of transmission window. In general, the phase shift is placed in the exact center so that the resonance peak is the sharpest, and the length of the phase shift is equal to a grating period so that there is always

²Parts of Section 2.6 have been published: X. Wang, W. Shi, S. Grist, H. Yun, N. A. F. Jaeger, and L. Chrostowski, “Narrow-band transmission filter using phase-shifted Bragg gratings in SOI waveguide,” in *IEEE Photonics Conference*, Arlington, VA, October 2011, pp. 869-870.

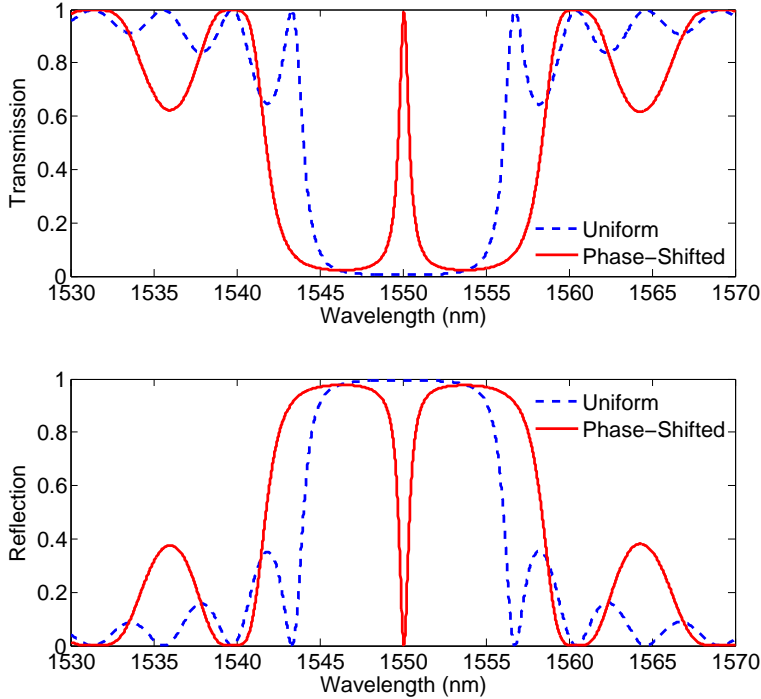


Figure 2.45: Spectral responses of a uniform and a phase-shifted grating. Note that the only difference between the two devices is the inclusion of the phase shift.

one resonance peak around the center of the stop band.

If the length of the phase shift is very long (e.g., 500Λ), it is possible to generate multiple resonance peaks within the stop band, as shown in Figure 2.47. Again, this can be interpreted as a Fabry-Perot (FP) cavity, where the two grating sections act as wavelength-selective mirrors separated by the phase shift. There are many longitudinal modes in the FP cavity, but only those within the reflection band are supported. As the cavity length is increased, the mode spacing becomes narrower, so the number of supported modes increases [104].

To evaluate the sharpness of the resonance peak, we introduce an important parameter: quality (Q) factor. In the context of resonators, Q factor is defined as

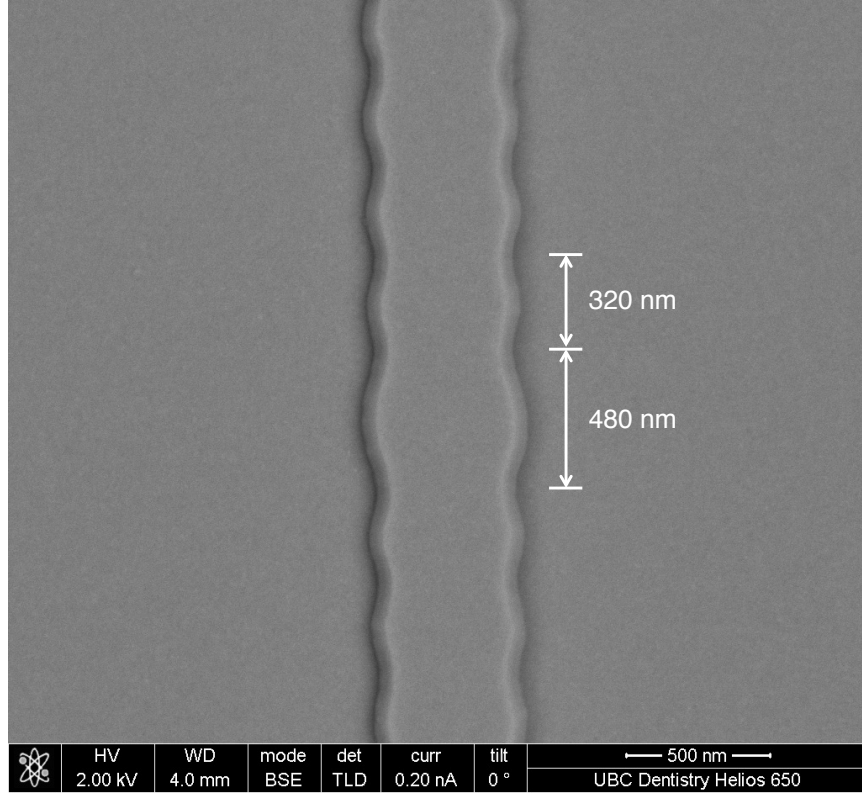


Figure 2.46: Top view SEM image of a fabricated strip waveguide phase-shifted grating. Design parameters: $W = 500 \text{ nm}$, $\Delta W = 80 \text{ nm}$, $\Lambda = 320 \text{ nm}$. Note that the phase shift in the central region can be identified by measuring the spacing between the grating grooves. Here, the spacing with the phase shift is 480 nm, corresponding to 1.5 times the grating period (320 nm).

2π times the ratio of the stored energy to the energy dissipated per oscillation cycle:

$$Q = 2\pi f_0 \times \frac{\mathcal{E}}{d\mathcal{E}/dt} = \omega_0 \tau_p \quad (2.6)$$

where f_0 is the resonant frequency, \mathcal{E} is the stored energy, ω_0 is the angular frequency, and τ_p is the photon lifetime. For high values of Q , the following definition

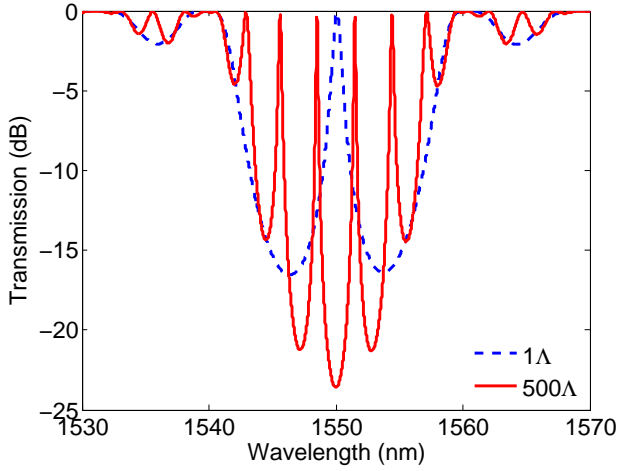


Figure 2.47: Transmission spectra for phase-shifted gratings with different phase-shift length. Multiple resonance peaks occur for long cavity length due to the reduced free spectral range.

is also mathematically accurate and commonly used:

$$Q = \frac{f_0}{\Delta f} = \frac{\lambda_0}{\Delta\lambda} \quad (2.7)$$

where Δf and $\Delta\lambda$ are the full width at half maximum (FWHM) frequency and bandwidth of the resonance, respectively.

For a phase-shifted Bragg grating (and in fact for all optical resonators in general), the Q factor is determined by two loss mechanisms: coupling loss and waveguide loss [105]. The coupling loss depends on the grating length and the grating coupling coefficient, both of which can be adjusted through design. The waveguide loss, by contrast, is inherent in the fabrication and it arises primarily from the waveguide roughness. Again, we can interpret a phase-shifted grating as an FP cavity, and the photon lifetime is given by:

$$\tau_p = \frac{n_g}{c(\alpha + \alpha_m)} \quad (2.8)$$

where α is the waveguide propagation loss, and α_m is the distributed mirror loss:

$$\alpha_m = \frac{\ln \sqrt{R_1 R_2}}{L} \quad (2.9)$$

where R_1 and R_2 are the mirror reflectivities, and L is the cavity length. Note that both α and α_m here are in units of m^{-1} . When R_1 and R_2 approach unity (corresponding to large κL of the two grating sections), the photon lifetime is limited by the waveguide propagation loss, and we can rewrite Eq. 2.6 to obtain the intrinsic Q factor [14]:

$$Q_I = \omega_0 \tau_p = \frac{\omega_0 \cdot n_g}{c \cdot \alpha_{[m^{-1}]}} = \frac{2\pi \cdot n_g \cdot 4.34}{\lambda \cdot 100 \cdot \alpha_{[dB/cm]}} \quad (2.10)$$

As discussed in Section 2.2.5.5, the loss values for strip waveguide gratings are in the range of 2.5–4.5 dB/cm. Assuming that the loss is 4 dB/cm and $n_g = 4.36$ (simulated value for a 500 nm waveguide with air cladding), the calculated Q_I is about 1.9×10^5 at 1550 nm. As will be shown in the next section, this value is comparable to the maximum Q value that we have observed experimentally.

2.6.2 Design Variations

This section describes how the transmission spectra varies with respect to various grating parameters.

The effects of variations in grating length and corrugation width are shown in Figure 2.48 and Figure 2.49, respectively. In Figure 2.48, as N is increased from 125 to 250, the stop band becomes deeper. This is because more light is reflected back as the grating becomes longer, i.e., higher reflectivity or larger R_1 and R_2 (see Eq. 1.13). More importantly, the resonant peak becomes sharper and the Q factor increases from 1900 to 3×10^4 . This is also due to the increasing R_1 and R_2 . From Eq. 2.9 and Eq. 2.8, we can see that the distributed mirror loss decreases, thus resulting in a longer photon lifetime and a higher Q factor. When N is fixed at 200 and the corrugation width is increased from 40 nm to 80 nm, the stop band becomes broader and deeper, as shown in Figure 2.49. This is easy to understand if we recall our discussion in Section 1.2. Specifically, larger corrugation results in larger κ , thus leading to higher reflectivity and broader bandwidth. We also see that the

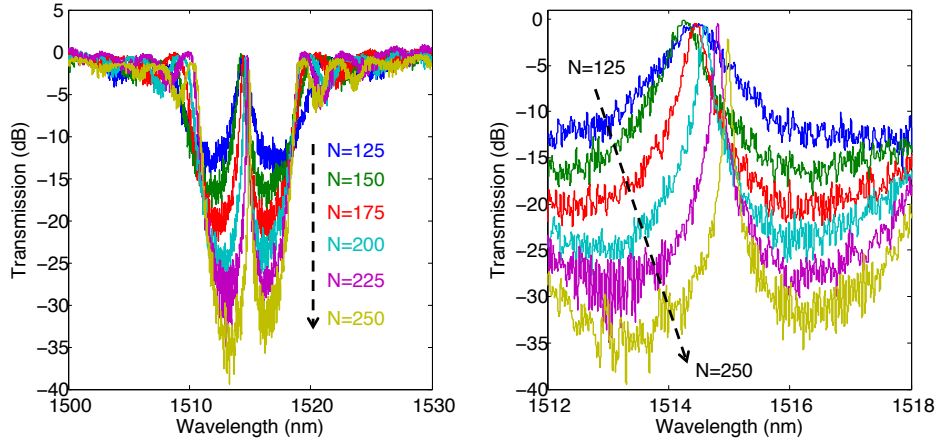


Figure 2.48: Transmission spectra for phase-shifted gratings with different N . Fixed parameters: oxide cladding, $W = 500$ nm, $\Delta W = 60$ nm, $\Lambda = 320$ nm. As N is increased, the stop band becomes deeper due to the increasing reflectivity, and the resonant peak becomes sharper due to the reduced coupling loss and higher Q factor.

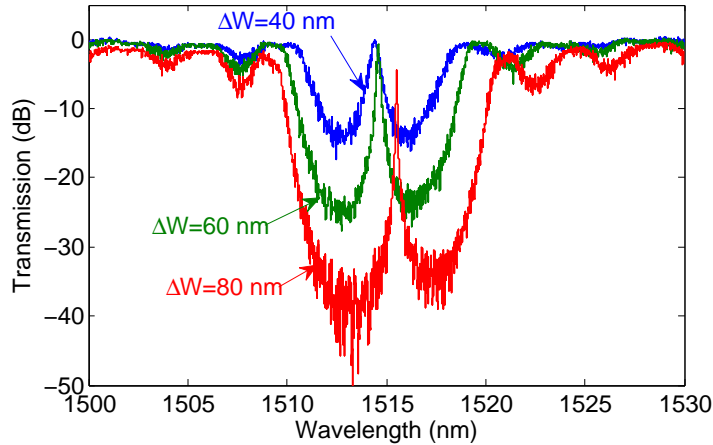


Figure 2.49: Transmission spectra for phase-shifted gratings with different ΔW . Fixed parameters: oxide cladding, $W = 500$ nm, $N = 200$, $\Lambda = 320$ nm. As ΔW is increased, the stop band becomes wider and deeper due to the increasing coupling coefficient, and the resonant peak becomes sharper due to the reduced coupling loss and higher Q factor.

resonant peak becomes sharper and the Q factor increases from 3000 to 3.3×10^4 . Again, this is due to the higher reflectivity, similar to the case in Figure 2.48.

Figure 2.50 shows the contour plot of the Q factor as a function of N and ΔW . The top and right boundaries of the contour plot are also plotted in Figure 2.51.

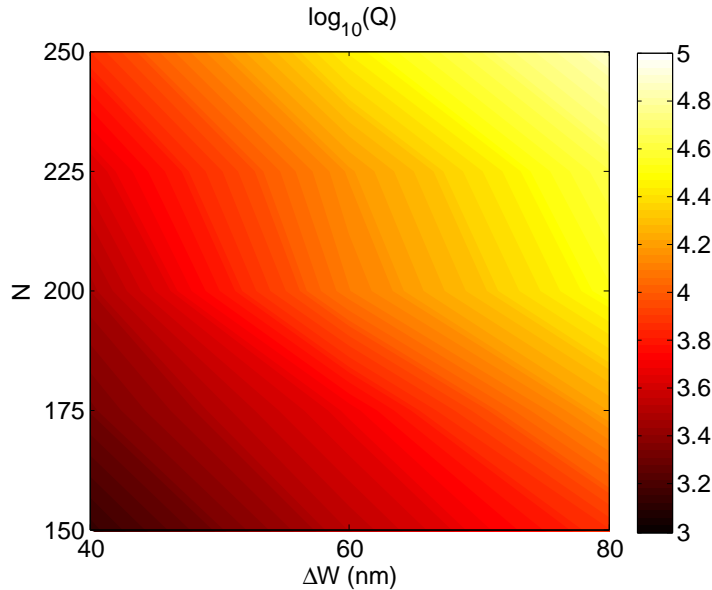


Figure 2.50: Contour plot of the Q factor as a function of ΔW and N . Fixed parameters: oxide cladding, $W = 500$ nm, $\Lambda = 320$ nm. The Q factor increases towards the top-right corner of the contour, i.e., large N and/or ΔW (essentially a high mirror reflectivity).

Obviously, to obtain a high Q factor, one would use a large N and/or ΔW (essentially a higher mirror reflectivity). However, it is important to note again that the Q factor will be ultimately limited by the waveguide loss. Here, we give another set of data to show this limitation in Figure 2.52. When N is 150, the transmittivity of resonance peak is very high. As N is increased beyond 150, the peak amplitude dramatically decreases. When N is 300, the resonance is buried into the noises and is hardly seen. This can be interpreted as increasing the mirror reflectivity (R , intensity reflectivity) of an FP cavity. For a loss-less FP cavity ($\alpha = 0$), the maximum transmission is unity [103]. However, if we include loss or gain, the

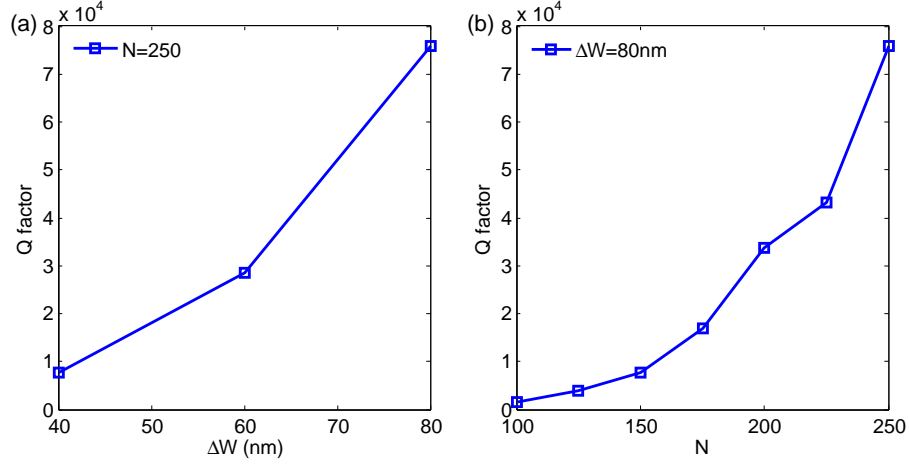


Figure 2.51: Measured Q factor as a function of (a) ΔW (corresponding to the top boundary of the contour plot in Figure 2.50) and (b) N (corresponding to the right boundary of the contour plot in Figure 2.50).

peak transmission is no longer unity. Let the intensity loss (or gain) per pass be G , defined as $G = I_{output}/I_{input}$, the maximum transmission can be written [103]:

$$T_{max} = \frac{(1-R)^2 G}{(1-GR)^2} \quad (2.11)$$

assuming that the FP cavity is symmetric, i.e., identical mirrors (analogous to a standard phase-shifted grating). In the case of loss, G is less than 1, so T_{max} is less than unity. When R approaches unity, T_{max} dramatically decreases, though Q still increases, as shown in Figure 2.53. Note that this is also analogous to the case of reducing the coupling coefficient in a ring resonator, where the peak amplitude in the drop port becomes smaller and the extinction ratio in the through port also becomes smaller.

By measuring many devices with different parameters, we have observed a minimum FWHM linewidth of about 8 pm (i.e., 1 GHz), as shown in Figure 2.54. This results in a maximum Q factor of 1.9×10^5 , which matches with the previous calculation in Section 2.6.1 using Eq. 2.10.

It is also important to note that when the Q factor is very high, the measured res-

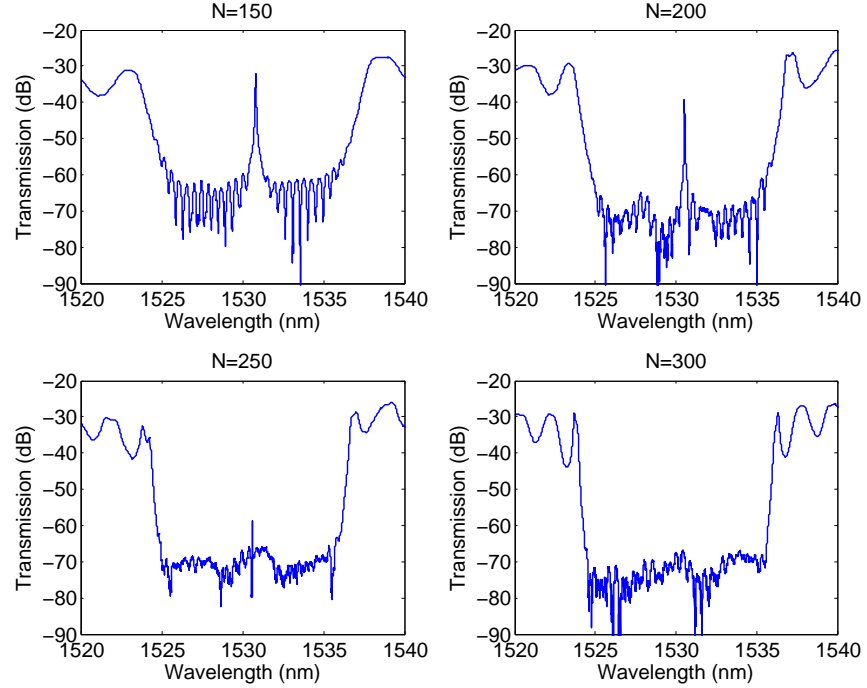


Figure 2.52: Transmission spectra (unnormalized) for phase-shifted gratings with different N . Fixed parameters: air cladding, $W = 500$ nm, $\Delta W = 60$ nm, and $\Lambda = 330$ nm. The peak amplitude drops significantly after $N=200$, as it goes beyond the critical coupling condition.

onance peak is power-dependant, as shown in Figure 2.55. When the input power is -10 dBm, the resonance has an almost ideal symmetric Lorentzian shape with a 3-dB linewidth of 20 pm (corresponding to a Q factor of about 7.6×10^4). However, when the input power is 0 dBm, the shape of the resonance is skewed to the right. This is because the high Q factor and the small modal volume result in high energy intensities and thus strong light-matter interaction. In this particular case, the power that actually enters into the device is about -6 dBm (0.25 mW), which can be regarded as a threshold for nonlinearities. The nonlinear optical effects include the Kerr effect that changes the refractive index and two-photon absorption (TPA) that generates free carriers and causes subsequent free-carrier dispersion (FCD) and free-carrier absorption (FCA). The heat generated from two-photon absorption

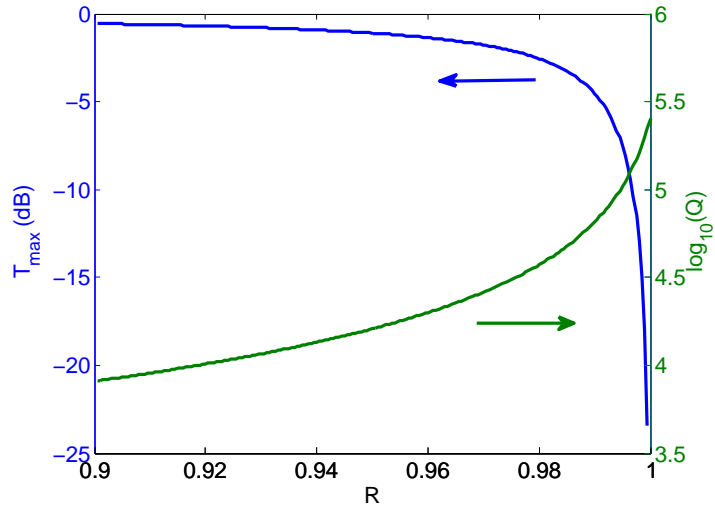


Figure 2.53: Maximum transmission and Q factor of an FP cavity as a function of R . Simulation parameters: $\alpha = 3 \text{ dB/cm}$, $L = 100 \mu\text{m}$, $G = 0.9931$. The maximum transmission decreases dramatically after the critical coupling condition, when the coupling loss equals the waveguide loss: $R = \sqrt{G} = 0.9965$.

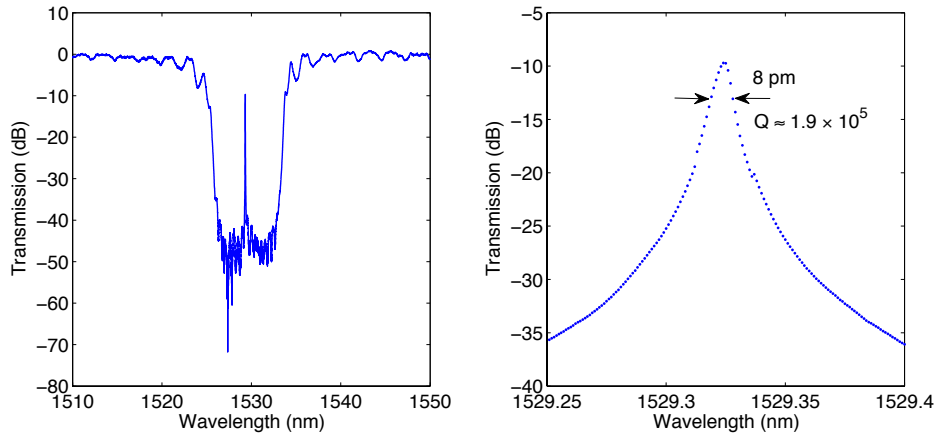


Figure 2.54: Maximum Q factor experimentally observed. Design parameters: air cladding, $W = 500 \text{ nm}$, $\Delta W = 40 \text{ nm}$, $N = 300$, and $\Lambda = 330 \text{ nm}$.

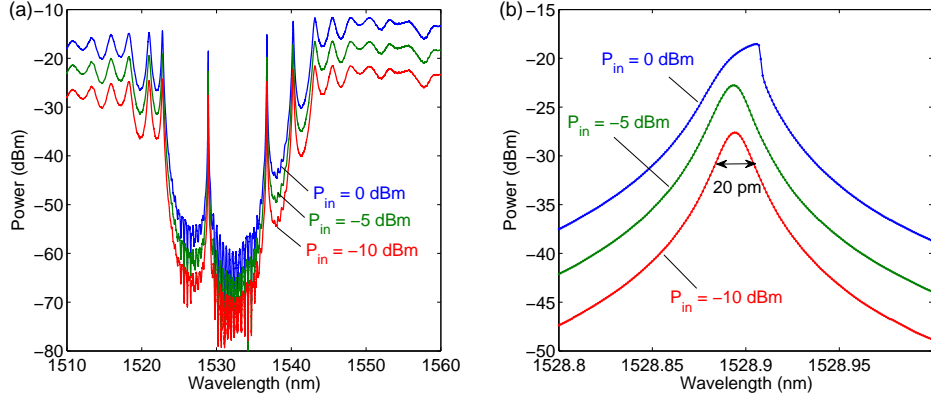


Figure 2.55: Measured transmission spectra (raw) of a high-Q phase-shifted grating at various input power levels. At 0 dBm input power, the resonance becomes asymmetric and the peak wavelength is skewed to the right.

and free-carrier absorption also raises the temperature and causes additional refractive index change by the thermo-optic effect. All these nonlinear effects combine and can lead to bi-stability or self-pulsation phenomena in high-Q silicon photonic cavities [106, 107]. Taking all these effects into account, the steady-state characteristic equation for a two-port system (including phase-shifted gratings) can be found [107]:

$$\frac{\omega_0'}{2Q_C}|s_1|^2 = |a|^2(\omega - \omega_0')^2 + \frac{|a|^2}{4} \left[\frac{\omega_0'}{Q_I} + \frac{\omega_0'}{Q_C} + \frac{\beta_{TPA}c^2}{n^2V_{TPA}}|a|^2 + \frac{e^3}{n^2\omega^2\varepsilon_0} \left(\frac{\beta_{TPA}c^2}{n^2V_{TPA}} \frac{|a|^4}{2\hbar\omega} \frac{\tau_{recon}}{V_{FC}} \right) \left(\frac{1}{m_e^{*2}\mu_e} + \frac{1}{m_h^{*2}\mu_h} \right) \right]^2 \quad (2.12)$$

where a is the normalized cavity field amplitude ($|a|^2$ equals the cavity energy), s_1 is the input waveguide field amplitude ($|s_1|^2$ equals the input power), Q_I is the intrinsic quality factor as defined by Eq. 2.10, Q_C is the coupling quality factor (i.e., replacing the waveguide loss by the distributed mirror loss in Eq. 2.10), β_{TPA} is the TPA coefficient, V_{TPA} is the cavity volume for TPA, V_{FC} is the cavity volume for free carriers, and τ_{recon} is the carrier recombination time. m_e^* and m_h^* are the

effective masses of electrons and holes, respectively. μ_e and μ_h are the carrier mobilities of electrons and holes, respectively. The constants c , e , ϵ_0 , and \hbar are the speed of light in vacuum, the elementary charge, the vacuum permittivity, and the reduced Planck constant, respectively. The cavity resonance wavelength including nonlinear effects can be given as [107]:

$$\begin{aligned} \lambda' = \frac{2\pi c}{\omega_0'} &= \lambda_0 - \frac{\lambda_0 e^2}{2n_0 n \omega^2 \epsilon_0} \left(\frac{\beta_{TPA} c^2 |a|^4 \tau_{recon}}{n^2 V_{TPA} 2\hbar \omega V_{FC}} \right) \left(\frac{1}{m_e^*} + \frac{1}{m_h^*} \right) \\ &+ \frac{\lambda_0}{n_0} \frac{\partial n}{\partial T} |a|^2 R_T \left[\frac{\beta_{TPA} c^2}{n^2 V_{TPA}} |a|^2 + \frac{e^3}{n^2 \omega^2 \epsilon_0} \left(\frac{\beta_{TPA} c^2 |a|^4 \tau_{recon}}{n^2 V_{TPA} 2\hbar \omega V_{FC}} \right) \right. \\ &\left. \left(\frac{1}{m_e^{*2} \mu_e} + \frac{1}{m_h^{*2} \mu_h} \right) \right] + \frac{\lambda_0}{n_0} \frac{n_2 c}{n V_{Kerr}} |a|^2 \end{aligned} \quad (2.13)$$

where λ_0 is the resonant wavelength in the linear regime, $\partial n / \partial T$ is the thermal-optic coefficient, R_T is the thermal resistance, n_2 is the Kerr coefficient, and V_{Kerr} is the cavity volume for Kerr effect, which is equal to that for TPA.

In Eq. 2.12, we can observe that the second term on the right-hand side causes the asymmetry of the resonance spectrum at high input powers. On the right-hand of Eq. 2.13, the second term corresponds to the FCD-induced blue shift, the third term corresponds to the thermal-optic red shift, and the last term corresponds to the Kerr effect. At room temperature, the thermal-optic effect dominates the bistability in high-Q silicon photonic cavities [107], therefore, we observed the red shift of the resonant wavelength in Figure 2.55(b).

In summary, high-Q phase-shifted gratings are potential for use in nonlinear optics. On the other hand, to avoid such nonlinearities and to remain in the linear regime, it is important to perform the measurement with low enough power.

2.6.3 Applications³

Phase-shifted Bragg gratings have various applications, such as biosensing [15, 105], microwave photonics [27, 108], and ultrafast optical signal processing [109]. In this section, we present an example of using a strip waveguide phase-shifted grating for biosensing.

Integrated waveguide Bragg gratings are promising candidates for sensing applications, including biosensors and gas sensors. In this section, we demonstrate its capability as a biosensor but the theory applies to gas sensors as well. For a bulk refractive index (RI) change, Δn_{fluid} , the Bragg wavelength shift $\Delta\lambda_B$ can be described by:

$$\frac{\Delta\lambda_B}{\lambda_B} = \frac{\Delta n_{fluid}}{n_g} \frac{\partial n_{eff}}{\partial n_{fluid}} \quad (2.14)$$

The sensitivity is the slope of wavelength shift versus bulk refractive index change:

$$S = \frac{\Delta\lambda_B}{\Delta n_{fluid}} = \frac{\lambda_B}{n_g} \frac{\partial n_{eff}}{\partial n_{fluid}} \quad (2.15)$$

and its unit is nm/RIU (refractive index unit). The limit of detection (LOD) is the minimum detectable refractive index change and there are usually two definitions: 1) change in index corresponding to one resonator linewidth, and 2) a system detection limit corresponding to the index change for a standard deviation in the measurement noise. The first definition describes the intrinsic device performance and thus is also known as intrinsic LOD:

$$\Delta n_{min} = \frac{\lambda_B}{QS} \quad (2.16)$$

Note that there are many other definitions in the literature, especially from the biological perspectives; however, we only focus on the optical properties in this work.

Figure 2.56 shows the measurement setup for biosensing. Aqueous solutions

³Parts of Section 2.6.3 have been published: S. T. Fard, S. M. Grist, V. Donzella, S. A. Schmidt, J. Flueckiger, X. Wang, W. Shi, A. Millspaugh, M. Webb, D. M. Ratner, K. C. Cheung, and L. Chrostowski, “Label-free silicon photonic biosensors for use in clinical diagnostics,” in *SPIE Photonics West*, San Francisco, CA, February 2013, paper 862909.

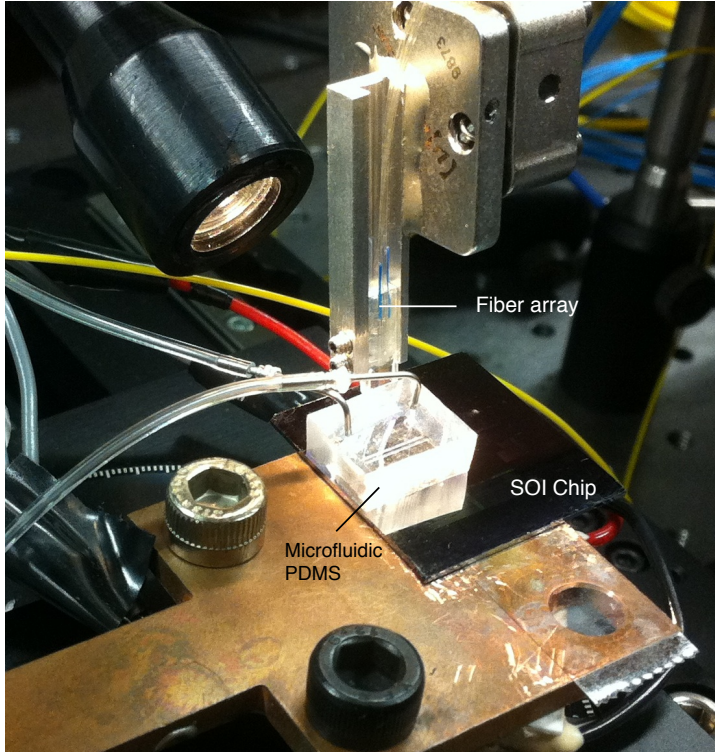


Figure 2.56: Measurement setup for biosensing. Reagents were introduced to the sensor using a reversibly bonded PDMS flow cell and Chemyx Nexus 3000 Syringe Pump at 10 $\mu\text{L}/\text{min}$. Note that the input/output grating couplers are placed far away from the sensor on the chip.

of NaCl were prepared in concentrations of 62.5 mM, 125 mM, 250 mM, 1 M, and 2 M. The refractive indices were measured using a refractometer. The Bragg grating sensors were exposed to the solutions at a flow rate of 10 $\mu\text{L}/\text{min}$. Figure 2.57 shows the experimental results of the sensitivity analysis of a strip waveguide phase-shifted grating with the following design parameters: $W = 500$ nm, $\Delta W = 40$ nm, $\Lambda = 320$ nm, and $N = 300$. A sensitivity of 58.52 nm/RIU is measured, which is close to the simulated value of about 55 nm/RIU. The quality factor (Q) of this device is measured to be 27600, which leads to an intrinsic LOD of about 9.3×10^{-4} RIU. As will be discussed in Chapter 4, we have also designed a biosensor using phase-shifted gratings in slot waveguides, which shows an improved in-

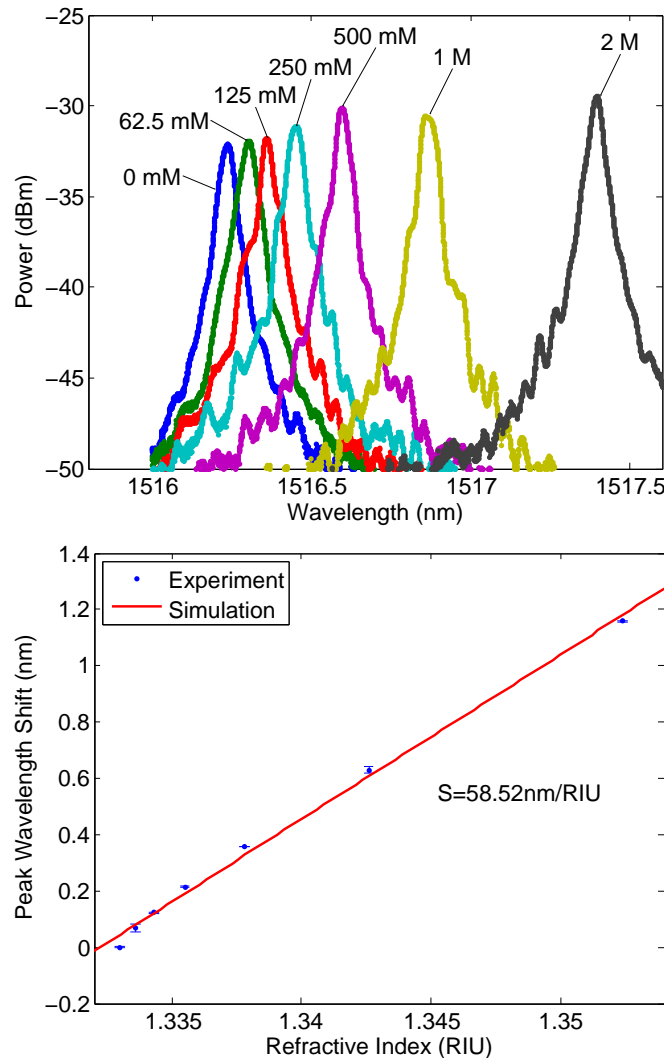


Figure 2.57: Top: transmission spectra for various concentrations of NaCl (note: 1 M=1 mol/L=1000 mol/m³). Bottom: peak wavelength shift versus bulk refractive index, showing a sensitivity of 58.52 nm/RIU.

trinsic LOD of about 3×10^{-4} RIU.

2.7 Sampled Gratings⁴

In this section, we present another important grating structure called sampled gratings. A sampled grating is formed by applying a sampling function to a conven-

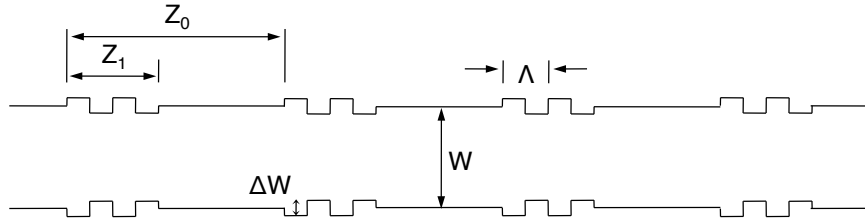


Figure 2.58: Schematic of a sampled grating.

tional uniform grating so that the grating elements are removed in a periodic fashion, as illustrated in Figure 2.58. The grating burst length is Z_1 , and the sampling period is Z_0 . The reflectivity of this structure can be obtained from the coupled-mode theory, which predicts that every spatial Fourier component of the dielectric perturbation contributes a peak to the reflection spectrum [110]. The multiplication of the sampling function and the uniform grating function in the spatial domain will be translated into the convolution of the single Fourier component of the uniform grating at the Bragg wavelength with the comb of Fourier components in the sampling function. Therefore, it leads to a reflection spectrum with periodic maxima [111]. Figure 2.59 shows the measured spectral responses of two sampled gratings on strip waveguides, where periodic maxima were clearly observed. The spacing between reflection peaks can be approximated by [111]:

$$\lambda_{spacing} \approx \frac{\lambda_B^2}{2n_g Z_0} \quad (2.17)$$

⁴Parts of Section 2.7 have been published: X. Wang, W. Shi, R. Vafaei, N. A. F. Jaeger, and L. Chrostowski, “Uniform and sampled Bragg gratings in SOI strip waveguides with sidewall corrugations,” *IEEE Photonics Technology Letters*, vol. 23, no. 5, pp. 290-292, 2011.

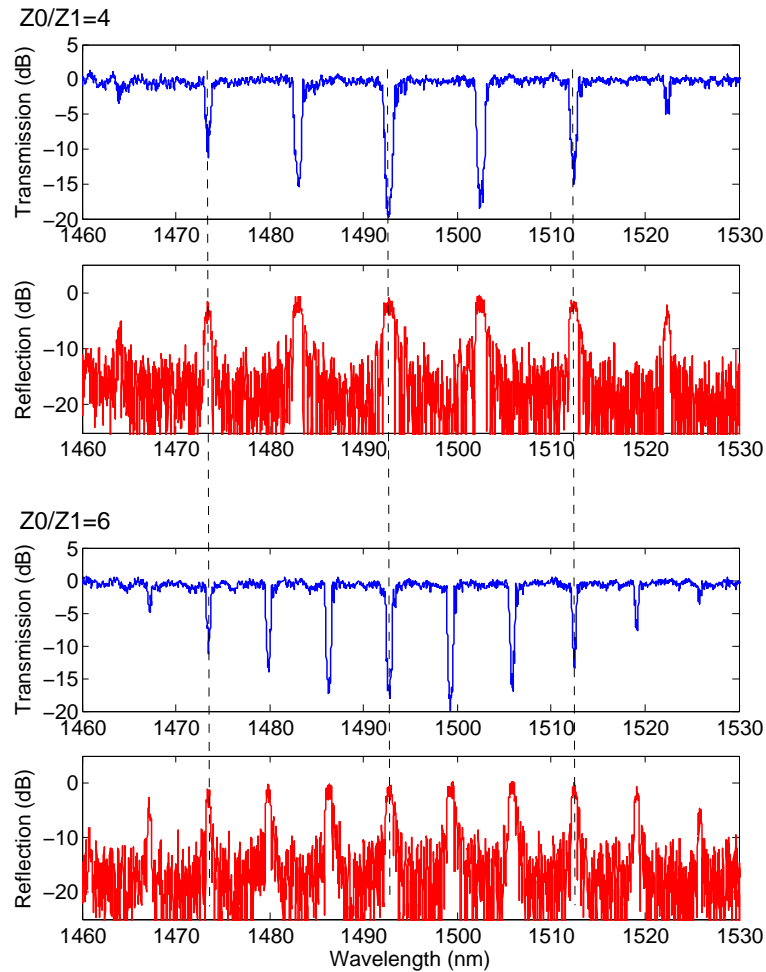


Figure 2.59: Measured transmission and reflection spectra of two sampled gratings. Design parameters: air cladding, $W = 500$ nm, $\Delta W = 20$ nm, $Z_1 = 6.4 \mu\text{m}$. Each device includes 20 sampling periods (i.e., total length is $20 Z_0$). The peak spacing for $Z_0/Z_1 = 4$ is 1.5 times larger than that for $Z_0/Z_1 = 6$, in agreement with Eq. 2.17.

This can be confirmed by comparing the spectra of the two devices in Figure 2.59, i.e., the peak spacing for $Z_0/Z_1 = 4$ is 1.5 times larger than that for $Z_0/Z_1 = 6$.

These comb-like spectra can be deployed in tunable lasers to achieve a wide tuning range through the Vernier effect [111]. They can also be used for multi-channel add/drop multiplexers and dispersion compensations. Figure 2.60 shows a layout example for achieving Vernier effect using two slightly mismatched sampled gratings. The measurement results are shown in Figure 2.61, where only the

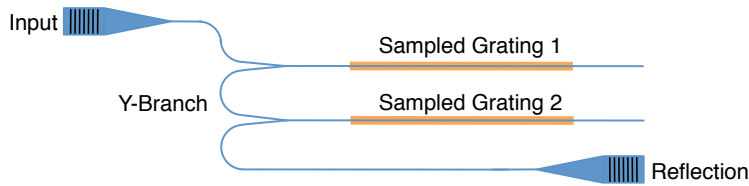


Figure 2.60: Layout for the Vernier effect using two sampled gratings with slightly mismatched sampling periods.

reflection peaks at 1530 nm are well aligned.

The suppression ratio of the side peaks is about 10 dB; however, this can be further improved by active tuning and/or optimizing the grating design such as using apodization to reduce the sidelobes. By adding active tuning components (e.g., thermal heaters) to each of the sampled gratings, the peak alignment can be adjusted. Specifically, a small index change in one sampled grating relative to the other can cause adjacent reflection maxima to come into alignment, thus shifting the final selected wavelength by a large amount [111]. This is similar to the principle of Vernier scale, i.e., a small shift in one arm can cause a substantial change in the alignment of the marks. For tunable lasers based on Vernier effect, lasing occurs at the pair of maxima that are aligned.

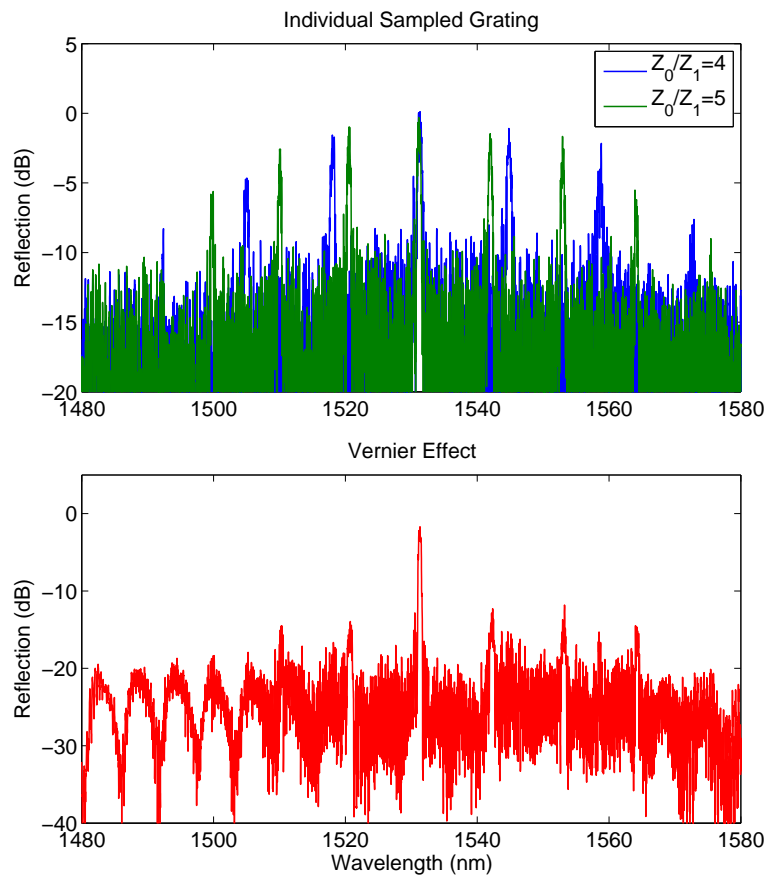


Figure 2.61: Measured reflection spectra of two individual sampled gratings (top) and the Vernier effect (bottom). The only major peak for the Vernier effect occurs where the peaks of individual sampled gratings are well aligned (at 1530 nm).

2.8 Summary

In this chapter, we have studied Bragg gratings in standard single-mode strip waveguides working at TE polarization. We predict that this family of devices will find many applications because it only requires a single etch (and is clearly more robust than slot waveguides, which will be discussed in Chapter 4). The bandwidth has been demonstrated as large as 30 nm (e.g., using 160 nm corrugations on a 500 nm strip waveguide with air cladding) and could be even larger by using larger corrugations or narrower waveguides. The strong coupling strength is particularly useful for designing high-Q phase-shifted gratings, as we have discussed in Section 2.6.

However, it is more challenging to design narrow-band gratings in strip waveguides. We have demonstrated bandwidths of about 1 nm using 10 nm corrugations (see Figure 2.33), but this is much smaller than the typical minimum feature size (also called critical dimension) of the current fabrication processes and is even approaching the limit of the grid size (e.g., 5 nm for the processes used in this thesis). Simard et al. have demonstrated strip waveguide gratings with bandwidths smaller than 1 nm, however, it was achieved at the expense of using a multi-mode waveguide (1200 nm wide) and a third-order grating (860 nm period).

Another critical issue is the fabrication nonuniformity – the effective index of a strip waveguide is sensitive to both width and thickness of the waveguide. Therefore, very good fabrication quality is needed. Specifically, the Si thickness uniformity of the wafer, as well as the linewidth uniformity of the fabrication process, has to be precisely controlled.

Chapter 3

Rib Waveguide Bragg Gratings

In the last chapter, we have discussed many grating structures using strip waveguides. It is clear that strip waveguide Bragg gratings have relatively large bandwidths (e.g., >1 nm even for a 10 nm corrugation width). However, numerous applications require narrow bandwidths, such as in wavelength-division multiplexing (WDM) systems. Also, our wafer-scale test has shown that strip waveguide gratings are very sensitive to fabrication variations. An alternative is to use rib waveguides, which typically have larger cross-sections and can reduce the fabrication challenges. In this chapter, we will demonstrate several types of narrow-band Bragg gratings using rib waveguides. We first discuss the basics of rib waveguides, and then demonstrate simple uniform gratings using rib waveguides.¹ We also propose a multi-period Bragg grating concept using rib waveguides. The sidewalls of the rib and the slab are corrugated using different periods, resulting in multiple Bragg wavelengths that are controlled separately. We then present the thermal sensitivity and the wafer-scale nonuniformity of rib waveguide gratings. Finally, we demonstrate rib waveguide Bragg gratings using a spiral geometry, which is to our knowledge the most compact Bragg grating filter to date.

¹Parts of Section 3.1 and Section 3.2 have been published: X. Wang, W. Shi, H. Yun, S. Grist, N. A. F. Jaeger, and L. Chrostowski, “Narrow-band waveguide Bragg gratings on SOI wafers with CMOS compatible fabrication process,” *Optics Express*, vol. 20, no. 14, pp. 15547-15558, 2012.

3.1 Rib Waveguide

The rib waveguide (also known as ridge waveguide) is another important waveguide geometry used in silicon photonics. In fact, the first demonstration of silicon photonic Bragg gratings uses a rib waveguide [68]. In general, it refers to a waveguide that consists of an infinite slab with a strip superimposed onto it. The waveguide geometry is often designed to be single mode [33]. However, a nominally single-mode rib waveguide can have higher-order leaky modes, which can cause unwanted dips in the transmission spectrum on the shorter wavelength side of the fundamental Bragg wavelength. To separate these leaky modes away from the fundamental mode, it is necessary to shrink the waveguide dimensions [68]. This is a general trend in silicon photonics as well, because small waveguide dimensions are desired for small bending radius and high integration density. However, most integrated Bragg gratings were demonstrated in bulky rib waveguides (e.g., up to a few microns [68, 73, 74, 112]) until our recent work in [113].

Figure 3.1 shows the cross section of the rib waveguide that we used for the grating design. It differs from the commonly used rib geometry, which usually has

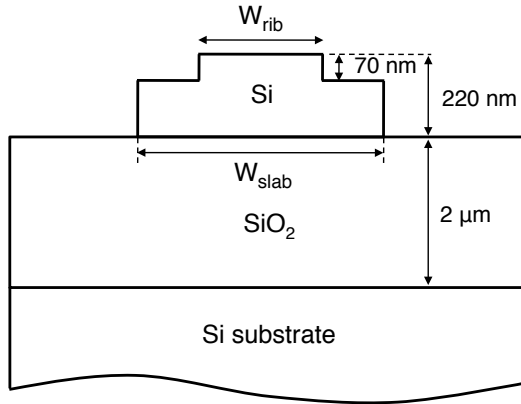


Figure 3.1: Schematic of the rib waveguide cross section (not to scale): $W_{\text{rib}} = 500 \text{ nm}$, and $W_{\text{slab}} = 1 \mu\text{m}$.

an infinite slab. In contrast, the finite slab strengthens the mode confinement and thus allows for relatively tighter bends. Again, the silicon thickness is 220 nm, and the shallow etch depth is 70 nm. The rib width (W_{rib}) is 500 nm, and the slab

width (W_{slab}) is 1 μm . As shown in Figure 3.2, most light is confined under the rib.

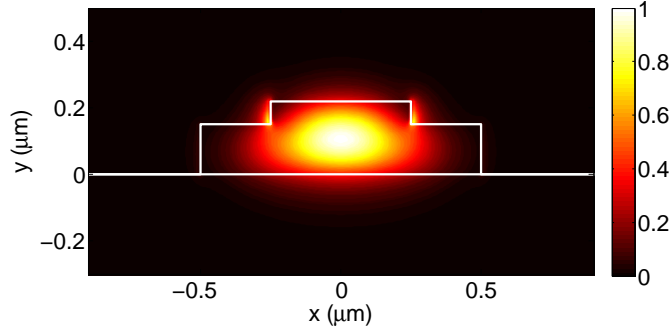


Figure 3.2: Simulated electric field of the fundamental TE mode in the rib waveguide with air cladding. The field intensity is low around the sidewalls, allowing for weak perturbations to the mode using relatively large sidewall corrugations.

The overlap between the electrical field with the sidewalls is very low around both the rib and slab sidewalls. This overlap reduction makes it possible to introduce weaker effective index perturbations compared to the strip waveguide gratings, thus allowing for smaller coupling coefficients and narrower bandwidths. Additionally, the waveguide propagation loss is also reduced. Figure 3.3 shows the cross-section of a fabricated rib waveguide.

3.2 Uniform Gratings

3.2.1 Design and Fabrication

There are several configurations to make gratings on rib waveguides. The grating corrugations can be on the top surface [68, 74], or on the sidewalls, where the sidewalls can be corrugated either on the rib [73] or on the slab [114]. The top-surface-corrugated configuration usually has a fixed etch depth, therefore, it is difficult to adjust the grating coupling coefficient. In contrast, the sidewall-corrugated configuration is much more flexible. The grating coupling coefficient can be easily controlled by varying the corrugation width, which is essential for complex grating structures, such as apodized gratings that can suppress reflection side lobes [114].

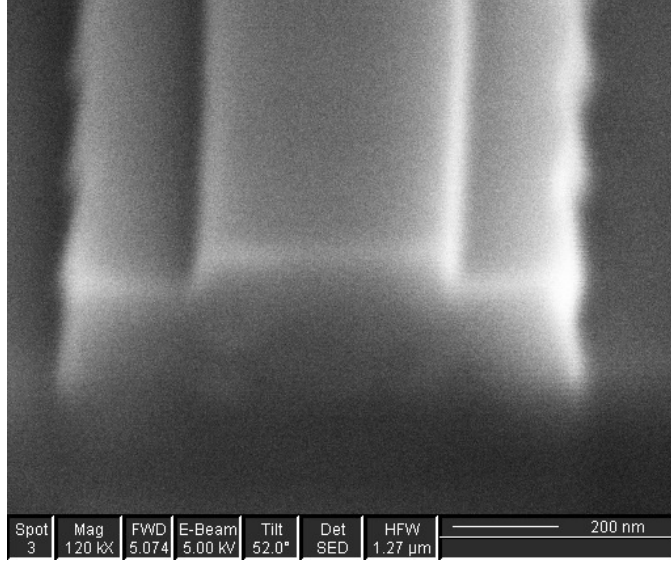


Figure 3.3: Cross-sectional SEM image of a rib waveguide with gratings on the slab.

Therefore, we use the latter configuration in our work. The gratings are realized by introducing periodic sidewall corrugations either on the rib or slab. Figure 3.4 shows the SEM images of two fabricated devices. The grating period Λ is designed to be 290 nm, with a duty cycle of 50%, and the number of grating period N is 2000. Note that we used square corrugations in the layout, but again, the gratings actually fabricated are rounded due to the lithography effects, as we already discussed in Chapter 2.

As mentioned in Chapter 1 and Chapter 2, strip waveguides typically exhibit much less bending loss than rib waveguides, therefore we use strip waveguides for routing. A double-layer linear taper was designed for the transition between the strip and rib waveguides, as shown in Figure 3.5. The taper is 30 μm long to ensure that the transition loss is negligible [34].

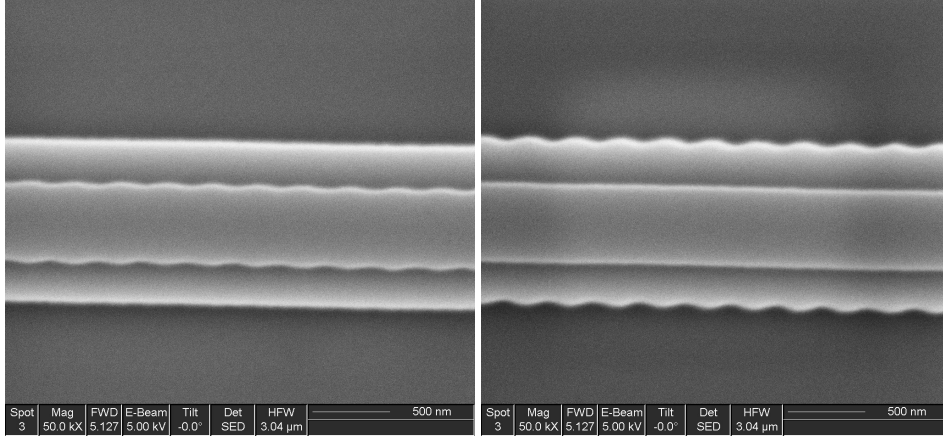


Figure 3.4: Top view SEM images of fabricated rib waveguide gratings designed with 60 nm corrugations on the rib (left) and 80 nm corrugations on the slab (right).

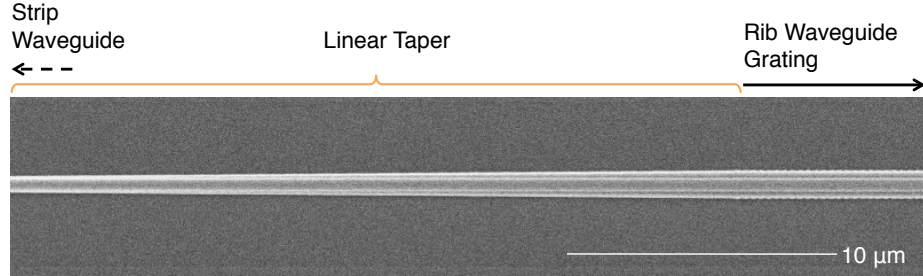


Figure 3.5: Top view SEM image of the transition from the strip waveguide to the rib waveguide grating using a linear taper.

3.2.2 Measurement Results

Figure 3.6 and Figure 3.7 show the measured spectral responses of two rib waveguide gratings with oxide cladding. The corrugations are designed on the slab, and the corrugation width is 80 nm and 100 nm, respectively. For both devices, only one dip exists in the transmission spectrum in a wide wavelength range, as can be seen in Figure 3.6. This indicates that the higher-order leaky modes are far away from the fundamental mode and thus can be ignored.

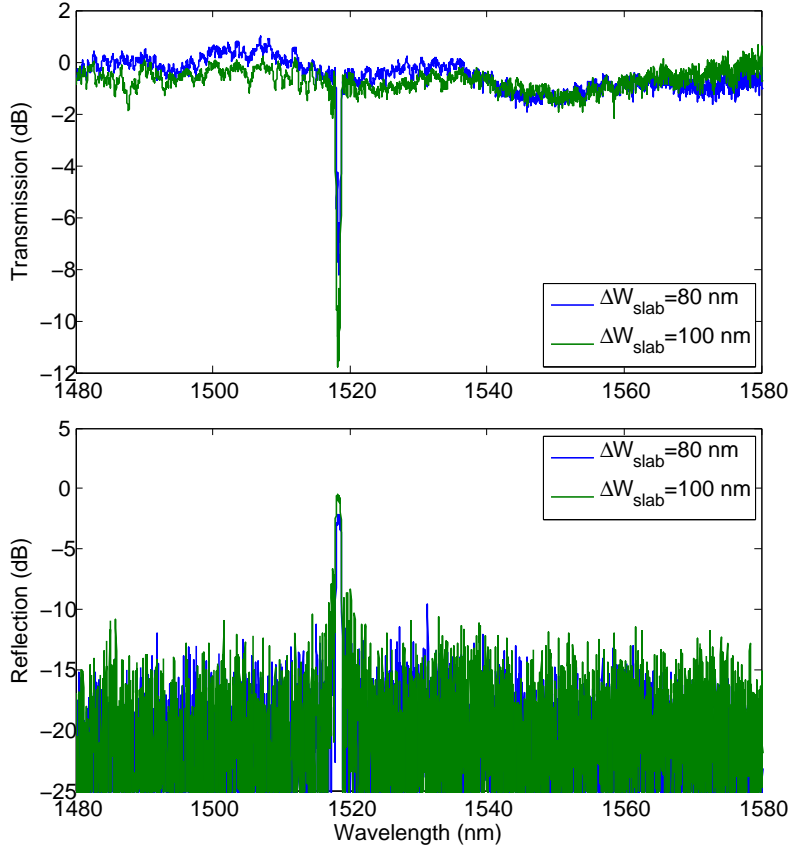


Figure 3.6: Measured transmission responses of two rib waveguide gratings with corrugations on the slab, each showing only one dip in a wide wavelength range without higher-order leaky modes.

More importantly, Figure 3.7 shows that the first-null bandwidth is only about 1.12 nm for $\Delta W_{\text{slab}} = 80 \text{ nm}$ and 1.19 nm for $\Delta W_{\text{slab}} = 100 \text{ nm}$. The 3-dB bandwidths are 0.74 nm and 0.86 nm, respectively. Based on the curve fitting in Figure 3.7, we obtain that the coupling coefficient κ is $2.52 \times 10^3 \text{ m}^{-1}$ for $\Delta W_{\text{slab}} = 80 \text{ nm}$, and is $3.25 \times 10^3 \text{ m}^{-1}$ for $\Delta W_{\text{slab}} = 100 \text{ nm}$. The ratio between these two κ is 1:1.29, comparable to the corrugation size ratio (1:1.25). This confirms that κ is approximately proportional to the corrugation size. However, we should recall that the bandwidth is determined not only by κ but also the grating length L (see

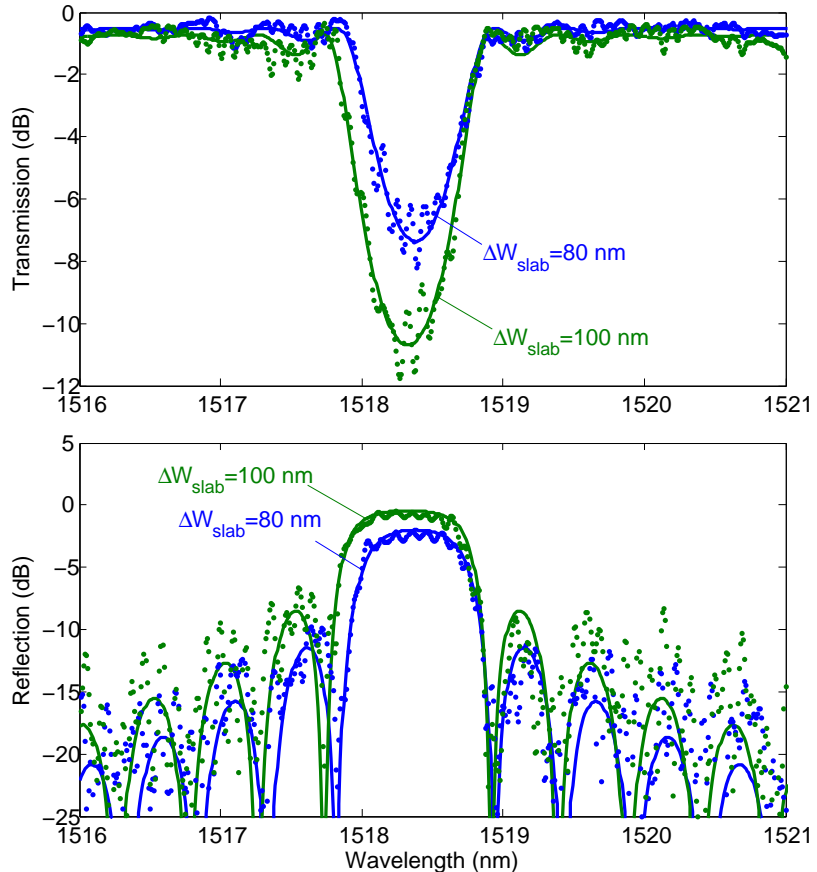


Figure 3.7: Zoomed-in view of Figure 3.6 around the Bragg wavelength. The dots are the measured values, and the solid curves are the fits using the analytical expression in Eq. 1.9. As expected, the grating with larger corrugations shows a slightly larger bandwidth and a higher reflectivity.

Eq. 1.16), especially for a small κ . In this case, the term π/L in the square root of Eq. 1.16 equals $5.42 \times 10^3 \text{ m}^{-1}$, which is actually larger than the two κ values above. This explains that the first-null bandwidth does not increase proportionally to the corrugation size, i.e., the bandwidth ratio is only 1:1.06. Also, as expected, the larger κ for $\Delta W_{\text{slab}} = 100 \text{ nm}$ causes a higher extinction ratio in the transmission and a larger peak amplitude in the reflection.

If we apply the same corrugation widths on a 500 nm strip waveguide, the first-null bandwidths are definitely much larger ($\geq 10 \text{ nm}$, see Figure 2.28). To obtain a similar bandwidth around 1 nm using strip waveguides, the corrugation width has to be 10 nm or even smaller, which can pose severe fabrication challenges.

Figure 3.8 shows the comparison of the coupling coefficients using different grating structures. The coupling coefficient was extracted by curve-fitting the measured spectral response using Eq. 1.9, as shown in Figure 3.7. We can see that

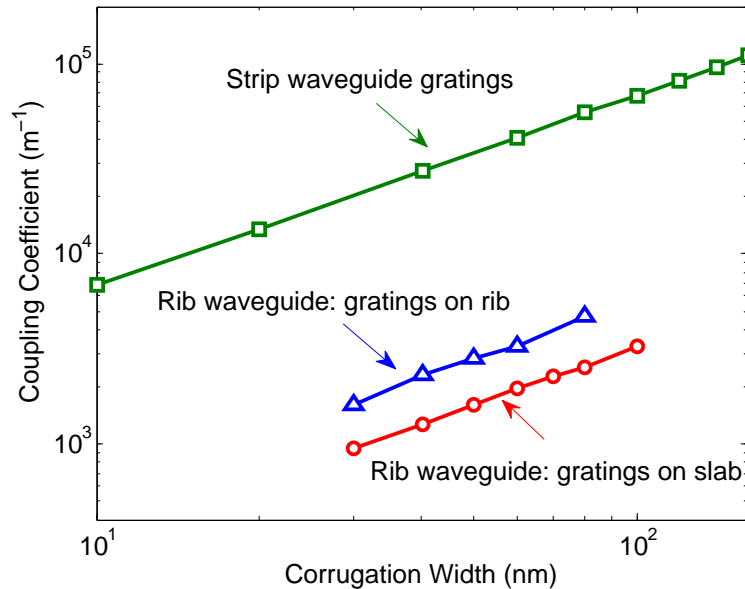


Figure 3.8: Extracted coupling coefficient versus designed corrugation width for various grating structures on a chip with oxide cladding. The strip waveguide is 500 nm wide and has the largest coupling coefficient, while the grating-on-slab configuration has the smallest coupling coefficient.

the green curve is well above the other two curves, i.e., strip waveguide gratings usually have very large κ and bandwidths. For the same corrugation width, the corrugation-on-slab configuration results in a smaller κ than the corrugation-on-rib configuration. This can be attributed to the fact that the optical field distribution at the slab sidewalls is weaker than at the rib sidewalls, as shown in Figure 3.2. The smallest κ we obtained in Figure 3.8 is about $1 \times 10^3 \text{ m}^{-1}$, corresponding to $\Delta W_{\text{slab}} = 30 \text{ nm}$. If we take this value into Eq. 1.16 and assume the grating is long enough, the first-null bandwidth is expected to be about 0.2 nm.

3.3 Multi-period Gratings²

Simple uniform grating structures only have one Bragg reflection band. However, optical filters with flexible spectral responses are of great interest for many applications. For example, in the last chapter we have demonstrated sampled gratings with a comb-like reflection spectrum, and phase-shifted gratings with a high-Q resonance within the stop-band of the transmission spectrum. For applications that require custom spectral responses, it might be necessary to cascade a number of grating sections with different periods. However, the performance of cascaded Bragg gratings is sensitive to the Si thickness variation and the nonuniformity of the fabrication process.

In this section, we demonstrate a multi-period Bragg grating concept, by taking advantage of the multiple sidewalls of the rib waveguide. The sidewalls of the rib and the slab are corrugated using different periods, resulting in two or more Bragg wavelengths that are controlled separately. This approach not only increases the design flexibility for custom optical filters but also reduces the device size and fabrication errors.

3.3.1 Dual-Period Grating

Figure 3.9 illustrates the design of a dual-period Bragg grating using the rib waveguide. The grating periods on the rib and on the slab are $\Lambda_1 = 290 \text{ nm}$ and $\Lambda_2 =$

²Parts of Section 3.3 have been published: X. Wang, H. Yun, N. A. F. Jaeger, and L. Chrostowski, “Multi-period Bragg gratings in silicon waveguides,” in *IEEE Photonics Conference 2013*, Bellevue, WA, September 2013, paper WD2.5.

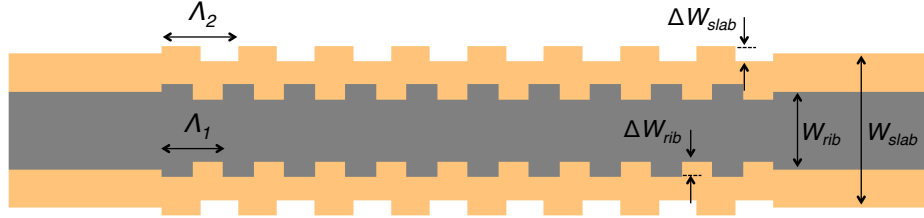


Figure 3.9: Schematic diagram of a dual-period rib waveguide grating (not to scale). Design parameters: $\Lambda_1 = 290 \text{ nm}$, $\Lambda_2 = 295 \text{ nm}$, $\Delta W_{rib} = 80 \text{ nm}$, $\Delta W_{slab} = 100 \text{ nm}$, and the grating length is $580 \mu\text{m}$.

295 nm, respectively. In order to obtain similar coupling coefficients for the two gratings, the corrugation widths on the rib and on the slab are designed to be $\Delta W_{rib} = 80 \text{ nm}$ and $\Delta W_{slab} = 100 \text{ nm}$, respectively. The grating length is $580 \mu\text{m}$, including 2000 periods on the rib and 1966 periods on the slab.

Figure 3.10(a) shows the measured raw transmission spectrum of a fabricated device within a wide wavelength range. We can clearly observe two sharp dips at λ_1 and λ_2 , corresponding to Λ_1 and Λ_2 , respectively. The normalized response is shown in Figure 3.10(b). It can be seen that both dips show an extinction ratio of more than 14 dB, as well as a 3-dB bandwidth of about 1 nm. The spacing between the two dips is 17.63 nm. We also show that the experimental result matches very well with the simulations results, as shown in Figure 3.11. We expect that the two dips can be manipulated separately by adjusting the grating period. The bandwidth can also be tailored by choosing an appropriate corrugation size.

3.3.2 Four-Period Grating

This multi-period concept can be further extended. Figure 3.12 illustrates the design of a 4-period Bragg grating using the rib waveguide. Instead of using symmetric corrugations on the rib or slab layer, we use asymmetric corrugations to increase the number of gratings. The grating periods are $\Lambda_1 = 285 \text{ nm}$ and $\Lambda_2 = 290 \text{ nm}$, $\Lambda_3 = 295 \text{ nm}$ and $\Lambda_4 = 300 \text{ nm}$, respectively. The corrugation widths on the rib and on the slab are still $\Delta W_{rib} = 80 \text{ nm}$ (for Λ_2 and Λ_3) and $\Delta W_{slab} = 100 \text{ nm}$ (for Λ_1 and Λ_4), respectively. The grating length is still $580 \mu\text{m}$, including $2035\Lambda_2$, $2000\Lambda_2$, $1966\Lambda_3$, and $1933\Lambda_4$.

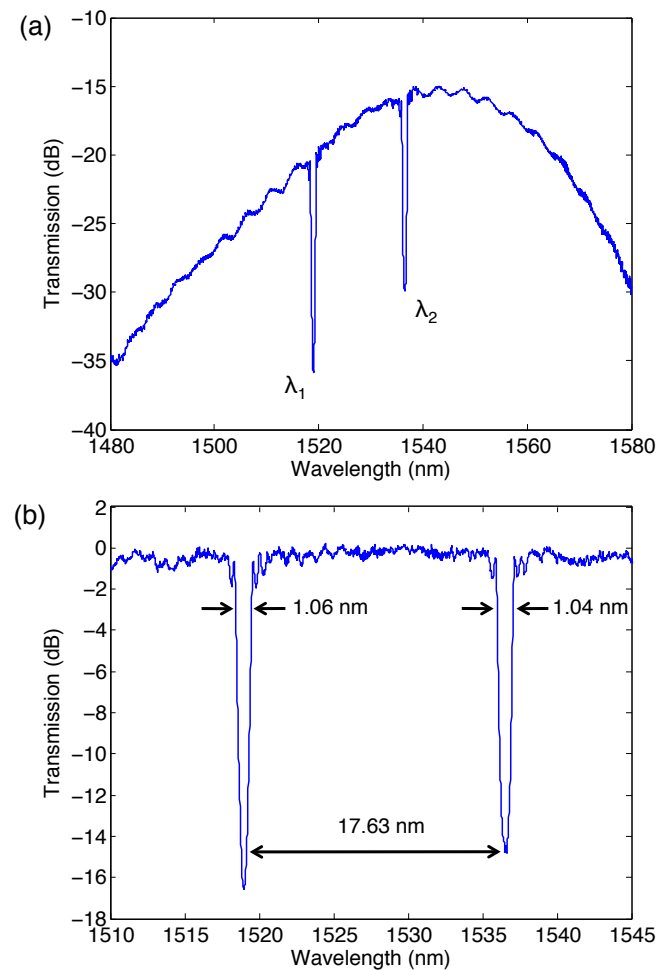


Figure 3.10: (a) Measured (unnormalized) transmission spectrum of the dual-period grating: λ_1 and λ_2 correspond to Λ_1 and Λ_2 , respectively. (b) Normalized response around the two Bragg wavelengths.

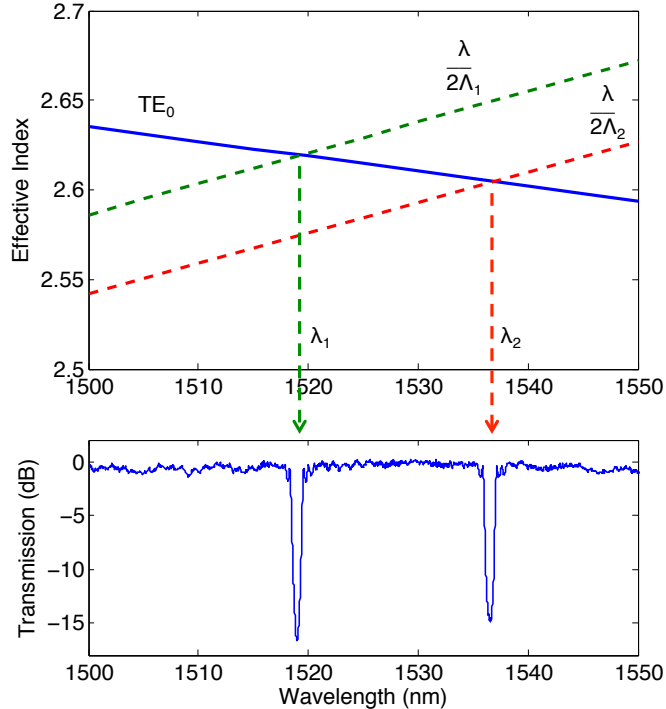


Figure 3.11: Dual-period grating: simulation vs. measurement. In the top graph, the solid blue curve shows the simulated effective index of the fundamental TE mode; the green and red dashed curves corresponds to the effective indices that are needed using Λ_1 and Λ_2 , respectively; thus, the intersection points correspond to the two Bragg wavelengths.

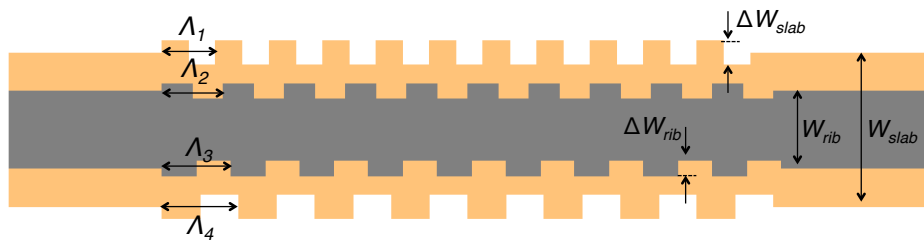


Figure 3.12: Schematic diagram of the 4-period rib waveguide grating (not to scale). Design parameters: $\Lambda_1 = 285 \text{ nm}$, $\Lambda_2 = 290 \text{ nm}$, $\Lambda_3 = 295 \text{ nm}$, $\Lambda_4 = 300 \text{ nm}$, $\Delta W_{rib} = 80 \text{ nm}$, $\Delta W_{slab} = 100 \text{ nm}$, and the grating length is $580 \mu\text{m}$.

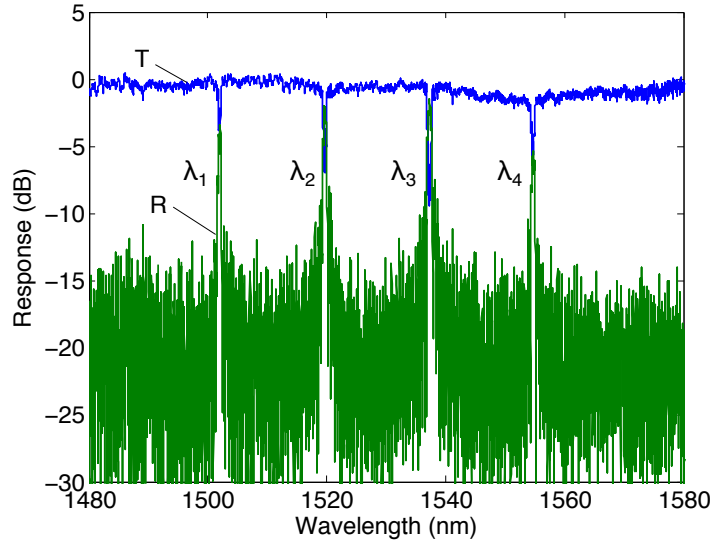


Figure 3.13: Measured spectral responses of a 4-period grating. λ_1 , λ_2 , λ_3 , and λ_4 correspond to Λ_1 , Λ_2 , Λ_3 , and Λ_4 , respectively.

Figure 3.13 shows the measured spectral responses of a fabricated device. We can clearly observe four Bragg wavelengths, each corresponding to one grating period. Note that the extinction ratios of the four notches are lower than those in Figure 3.10, because the coupling coefficients are reduced by half. In summary, this multi-period grating concept increases the design flexibility and allows for more custom optical functions.

3.4 Thermal Sensitivity

In this section, we use the dual-period grating discussed in the Section 3.3.1 to study the thermal sensitivity of rib waveguide gratings. Figure 3.14 shows how the Bragg wavelengths shift with temperatures. Clearly, both Bragg wavelengths are red-shifted as the temperature is increased. As shown in Figure 3.15, the thermal sensitivities of the two Bragg wavelengths are approximately the same: about 85 pm/ $^{\circ}\text{C}$. These values are also very close to the measured thermal sensitivity of strip waveguide gratings in Section 2.4, i.e., 84.4 pm/ $^{\circ}\text{C}$.

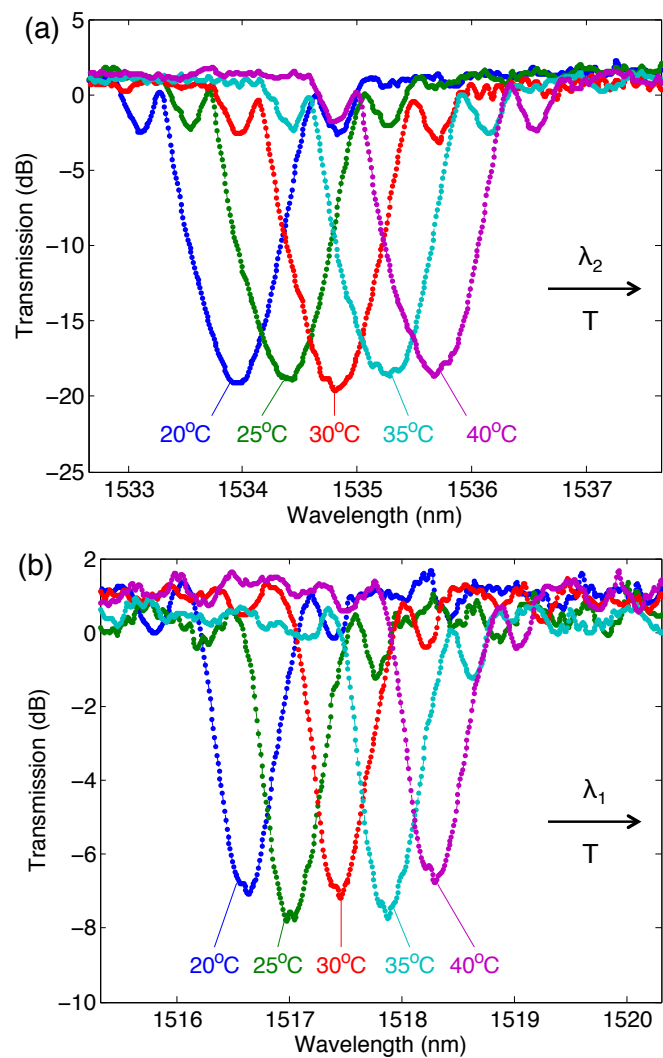


Figure 3.14: Bragg wavelength shift of a dual-period rib waveguide grating at different temperatures: (a) plot around λ_2 , (b) plot around λ_1 .

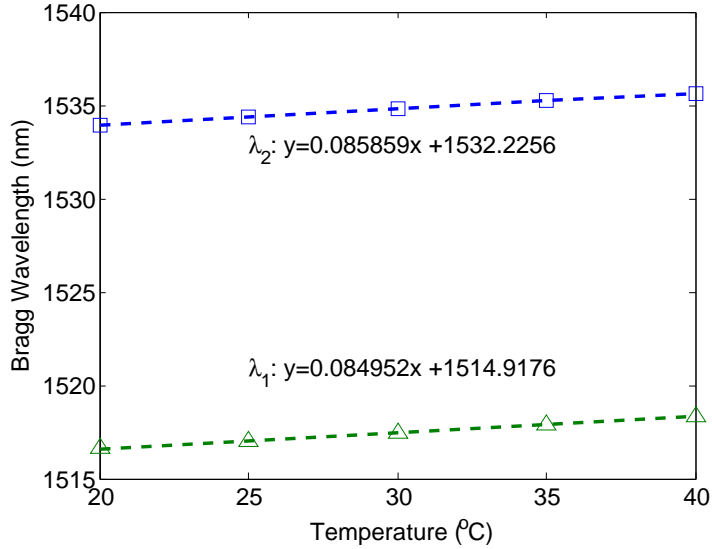


Figure 3.15: Bragg wavelengths versus temperature corresponding to the spectra in Figure 3.14, showing thermal sensitivities of about 85 pm/°C.

3.5 Wafer-Scale Performance

Next, we will study the wafer-scale performance of rib waveguide gratings, again using the dual-period grating device discussed in the Section 3.3.1. We use the same wafers that we used for strip waveguide gratings in the last chapter (recall in Section 2.5 that Wafer A has air cladding and Wafer B has oxide cladding). We may also recall that the exposure dose for the deep etch is increased from left to right across the wafer, so the slab width should decrease from column -4 to column 2. On the other hand, the exposure dose for the partial etch is fixed, so the shallow-etched rib is supposed to be on target everywhere across the wafer. From Figures 3.16 to Figure 3.20 , we have the following important observations:

Wavelength

- The wavelength variations are much smaller than that for the strip waveguide grating, i.e., 6–8 nm vs. >30 nm.
- The wavelength variations are random, whereas for the strip waveguide grat-

ing, the two wafers show a clear trend that the wavelength decreases from left to right columns (see Figures 2.41 to 2.43). This is because the rib waveguide is much less sensitive to the slab width than the strip waveguide to the waveguide width. Therefore, the Si thickness variation, which is random, is the dominant source of variation for rib waveguide gratings, despite of the large and intentional slab width variations induced by the exposure dose sweep.

- λ_1 and λ_2 show almost the same variations. This is expected because the two wavelengths come from the same waveguide and thus are subject to the same waveguide variations. This is also reflected by the spacing between λ_1 and λ_2 , namely, the spacing variation is only about 0.2 nm on both wafers.
- The average values of λ_1 and λ_2 on Wafer B is about 4 nm larger than those on Wafer A, due to the higher index of the cladding.

Bandwidth

- For $\Delta\lambda_2$, both wafers show a similar trend that the bandwidth increases from left to right columns. This agrees with the intentional exposure dose variation, i.e., the slab width decreases and thus the coupling becomes stronger.
- For $\Delta\lambda_1$, the variations are smaller and more random than that for $\Delta\lambda_2$.

Table 3.1 lists the wafer-scale statistics of the measurement data. The general conclusion is that rib waveguide gratings have better uniformity than strip waveguide gratings. Another finding is that the Bragg wavelength variation of rib waveguide gratings is mainly caused by the Si thickness variations. Hence improving the SOI thickness uniformity is very important. It is fortunate that wafer manufacturers are always improving the uniformity over time, driven by the CMOS industry that is now developing 14 nm technologies. In the silicon photonics area, the state-of-the-art foundry process can achieve tight within-wafer silicon thickness variation of $3\sigma < 2.5$ nm [8]. Hopefully, within the next few years, the wafer specifications can be further improved to meet the strict requirement of silicon photonic devices in a cost-effective way.

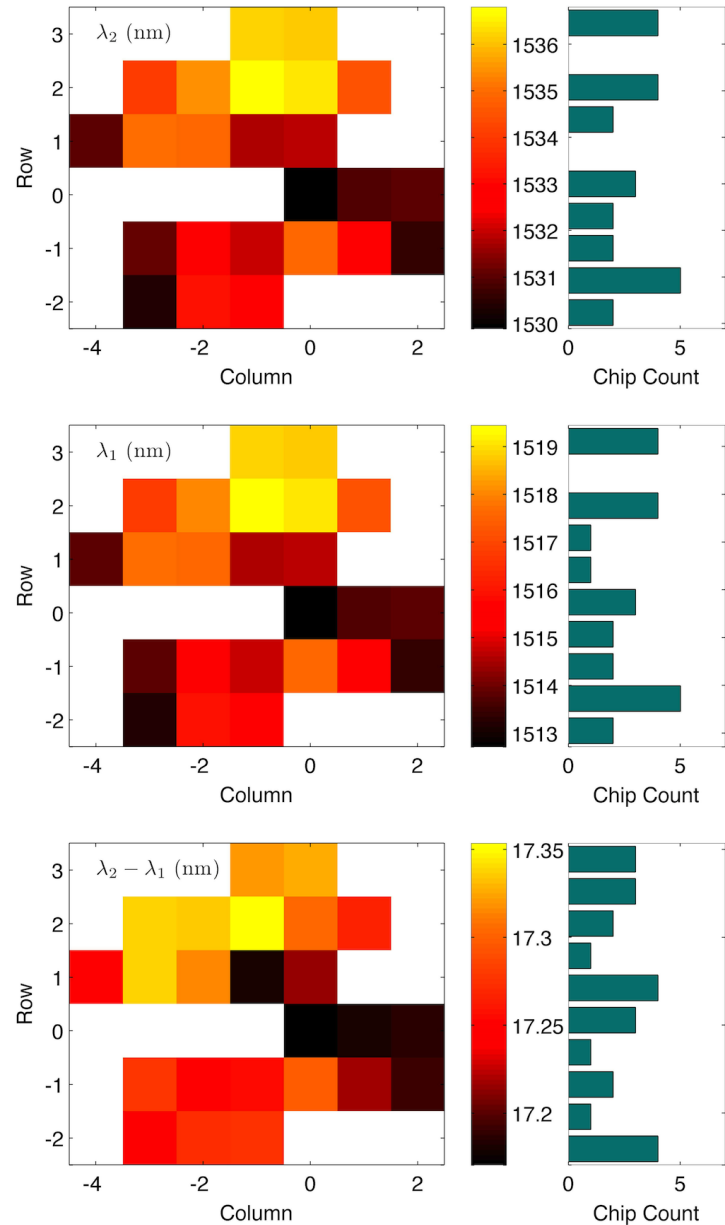


Figure 3.16: Wavelength nonuniformity of the dual-period grating on Wafer A.

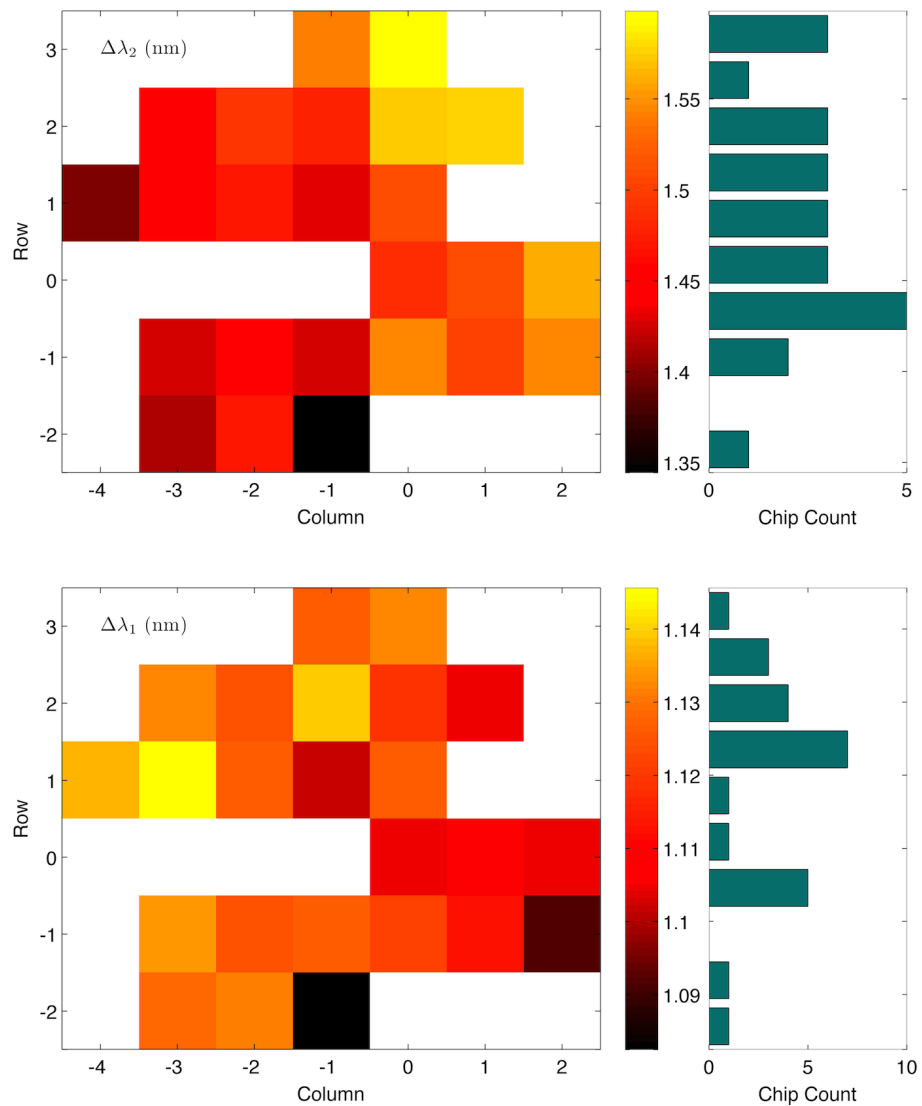


Figure 3.17: Bandwidth nonuniformity of the dual-period grating on Wafer A.

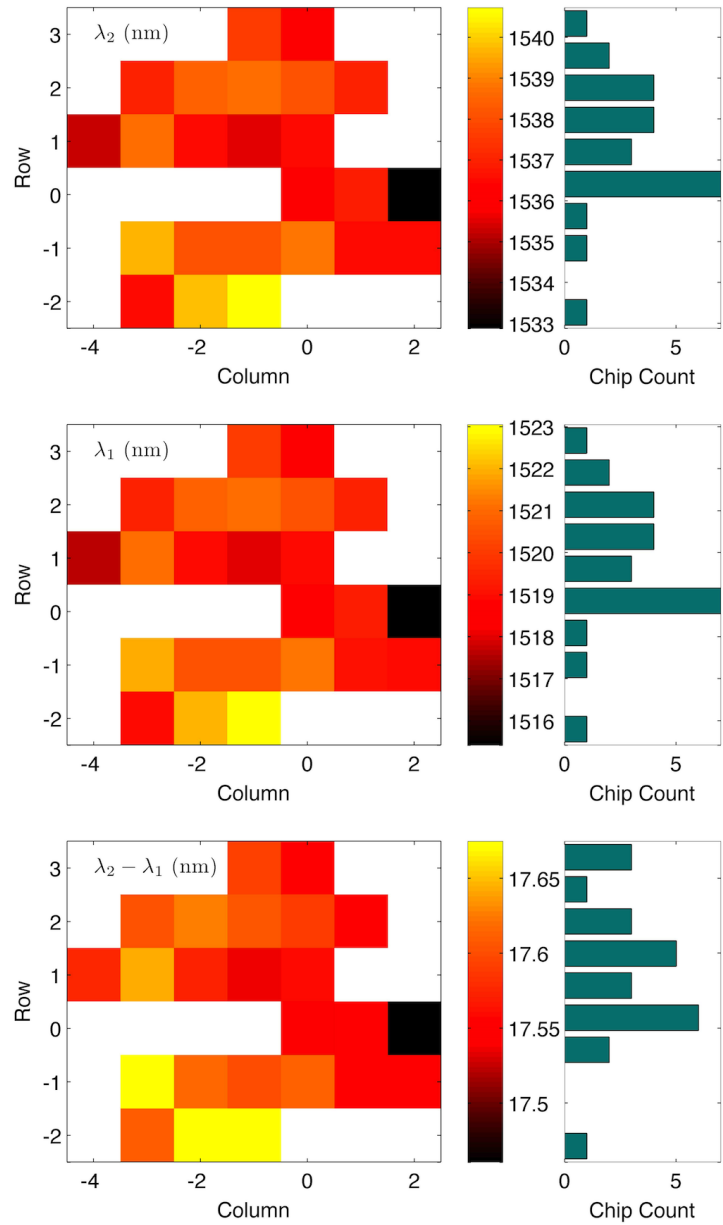


Figure 3.18: Wavelength nonuniformity of the dual-period grating on Wafer B.

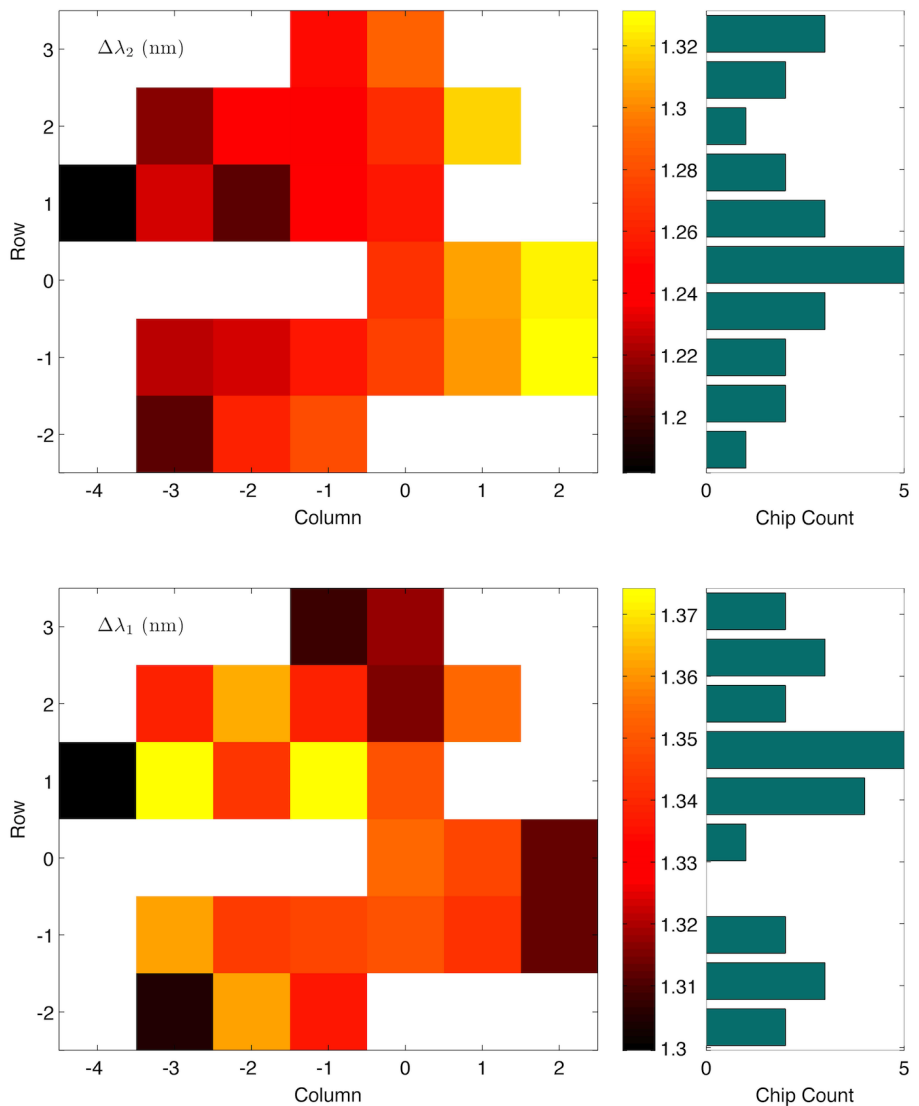


Figure 3.19: Bandwidth nonuniformity of the dual-period grating on Wafer B.

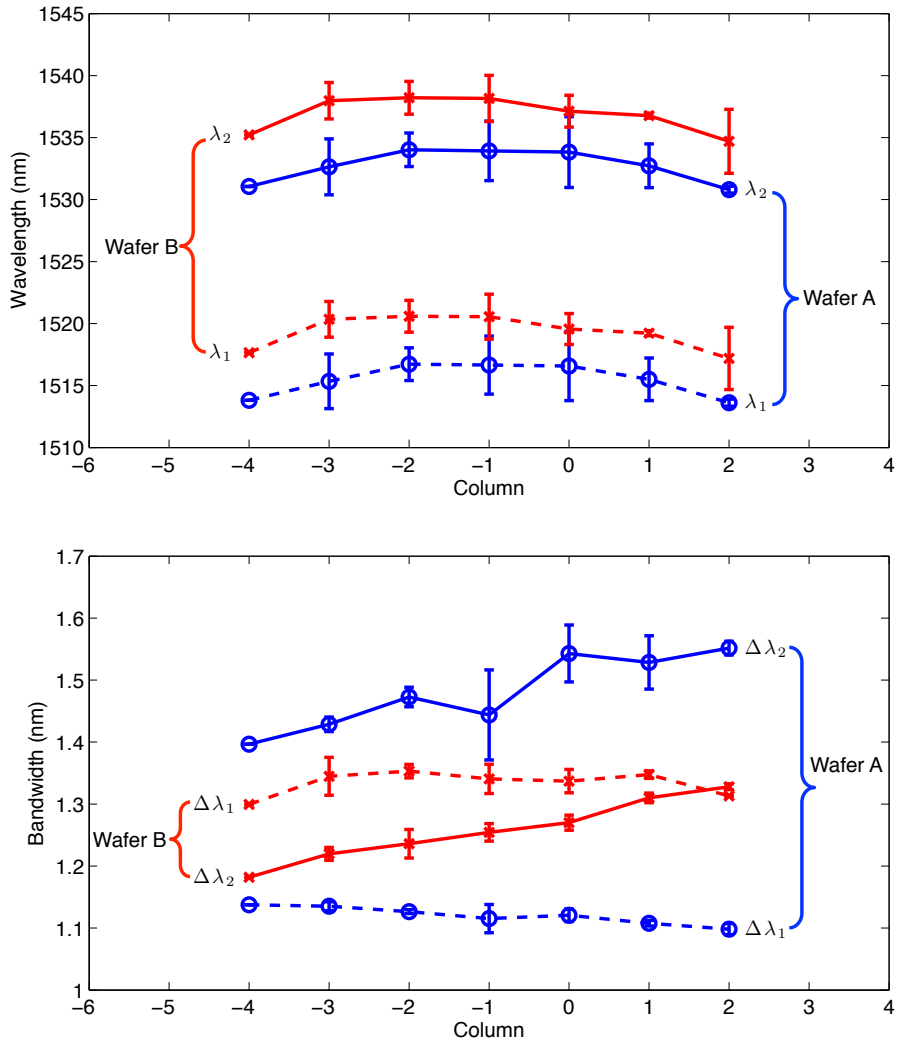


Figure 3.20: Performance nonuniformity of the dual-period grating as a function the column number. Each error bar is symmetric and the length is two standard deviations (within each column). All variations are random except the bandwidth variations for $\Delta\lambda_2$, which show that the bandwidth increases from left to right columns due to the intentional exposure dose variation.

Device	Parameter	Wafer A (air cladding)			Wafer B (oxide cladding)		
		Mean	Range	Standard Deviation	Mean	Range	Standard Deviation
Strip WBG	λ	1523.52 nm	31.90 nm	8.80 nm	1534.76 nm	33.56 nm	8.99 nm
	$\Delta\lambda$	4.24 nm	1.17 nm	0.31 nm	2.92 nm	0.33 nm	0.09 nm
Rib WBG	λ_1	1515.91 nm	6.73 nm	2.12 nm	1519.75 nm	7.63 nm	1.66 nm
	λ_2	1533.18 nm	6.91 nm	2.17 nm	1537.34 nm	7.85 nm	1.70 nm
	$\lambda_2-\lambda_1$	17.26 nm	0.18 nm	0.06 nm	17.59 nm	0.21 nm	0.05 nm
	$\Delta\lambda_1$	1.12 nm	0.06 nm	0.02 nm	1.34 nm	0.07 nm	0.02 nm
	$\Delta\lambda_2$	1.48 nm	0.25 nm	0.06 nm	1.26 nm	0.15 nm	0.04 nm

Table 3.1: Statistics of strip and rib waveguide Bragg gratings (WBG).

3.6 Spiral Gratings³

We have shown that rib waveguide gratings can achieve narrow bandwidths. Since the perturbations are very weak, a very long length is required to obtain a high reflectivity. However, this is often not desired from the layout perspective because the high aspect ratio makes it difficult to integrate them efficiently in photonic integrated circuits. More importantly, the performance of long Bragg gratings is more likely to be affected by the Si thickness variations, as we already discussed in Section 2.2.5.5. If the fabrication is done using electron beam lithography, long Bragg gratings may also suffer from stitching errors due to the limited writing field. Therefore, it is important to pack long Bragg gratings in a small area.

Recently, Zamek et al. [115] demonstrated Bragg gratings based on a curved strip waveguide with weakly coupled pillars, showing a length of 920 μm within an area of 190 $\mu\text{m} \times$ 114 μm and a stop bandwidth of 1.7 nm. The packing efficiency, defined as L/\sqrt{A} where L is the length and A is the area, is about 6.2 [115]. To further improve the packing efficiency, spiral geometries can be used [116, 117].

³Parts of Section 3.6 have been published: X. Wang, H. Yun, and L. Chrostowski, “Integrated Bragg gratings in spiral waveguides,” in *CLEO 2013*, San Jose, CA, June 2013, paper CTh4F.8.

Simard et al. demonstrated third-order Bragg gratings in multimode strip waveguides, showing a length of 2 mm within an area of $200 \mu\text{m} \times 190 \mu\text{m}$, attaining packing efficiency of about 10.2 [116].

In this section, we demonstrate first-order Bragg gratings in a single-mode rib waveguide using a spiral geometry. Our results show not only a significantly improved packing efficiency of about 21.8, but also a very narrow bandwidth of 0.26 nm.

3.6.1 Design

The rib waveguide is the same as in the last few sections, and we chose to use the rib sidewalls for the construction of gratings. As illustrated in Figure 3.21, the

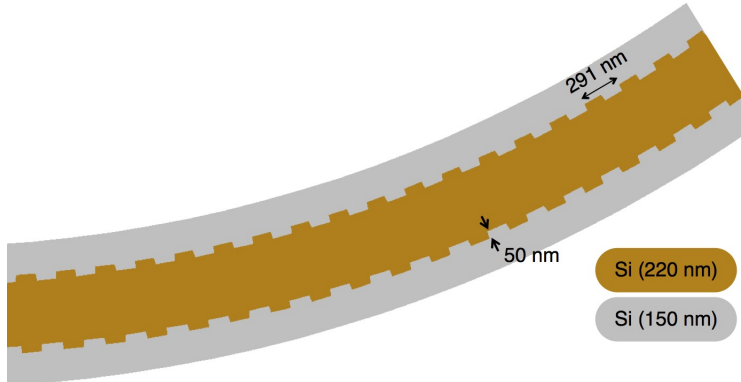


Figure 3.21: Top view of the spiral grating design.

gratings are designed on the rib using sidewall corrugations. On each side of the rib, the corrugation width is designed to be 50 nm. The period of the first-order grating is kept constant at 290.9 nm in the whole spiral.

Figure 3.22 shows the optical microscope images of a fabricated device. The spiral consists of a series of half circles with different diameters (D), while the radius of curvature is kept constant within each half circle. As shown in Figure 3.22(b), the diameters of the two smallest half circles (D_{min}) in the centre, i.e., the S-shape, are $20 \mu\text{m}$. The spacing between two adjacent half circles, or the spiral pitch (P), is $5 \mu\text{m}$ to ensure low crosstalk. Note that this value is quite conservative and could be reduced (e.g. to $3 \mu\text{m}$) to further improve the space

efficiency. Therefore, the diameters of the half circles except for the S-shape start

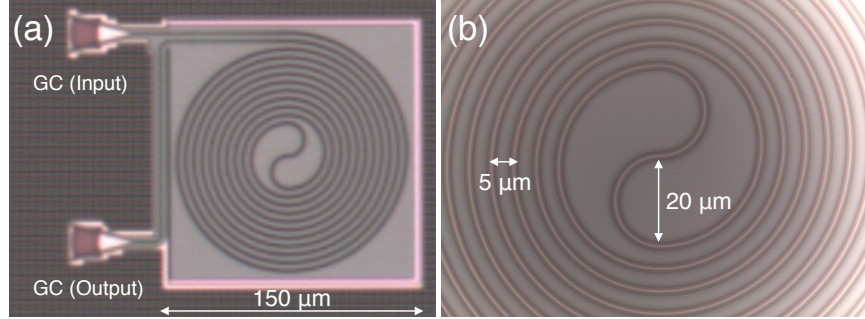


Figure 3.22: Optical microscope images of the fabricated device with $N=10$.
(a) Whole layout. (b) Enlarged image of center region of the spiral.

from $45 \mu\text{m}$ and increment with a step of $5 \mu\text{m}$. The length and area of the spiral is determined by the largest half circle, and, as shown in Figure 3.22(a), the largest half circle is the outmost one on the right, with clockwise light propagation. Excluding this largest half circle and the S-shape, the spiral can be divided equally into left and right, each with N half circles. The diameter of the largest half circle can then be described as:

$$D_{max} = 2D_{min} + (2N_R + 1)P \quad (3.1)$$

and the total length of the spiral grating is:

$$L = \frac{\pi}{2} [4(N_R + 1)D_{min} + (2N_R^2 + 2N_R + 1)P] \quad (3.2)$$

In this work, we present two proof-of-concept designs, one with $N_R = 5$, $D_{max} = 95 \mu\text{m}$, $L = 1.233 \text{ mm}$, and the other with $N_R = 10$, $D_{max} = 145 \mu\text{m}$, $L = 3.118 \text{ mm}$.

In the spiral, the variation of the bending radius potentially causes two issues: the variation in the effective index and the mode mismatch loss. First, we simulate the effective index of the waveguide as a function of bending radius (R), as shown in Figure 3.23. We can see that for R larger than $22.5 \mu\text{m}$, the effective index variation is very small ($< 1.2 \times 10^{-4}$) and thus is negligible. However, from $R = 22.5 \mu\text{m}$ to $R = 10 \mu\text{m}$, the effective index is increased by about 1.8×10^{-3} , which

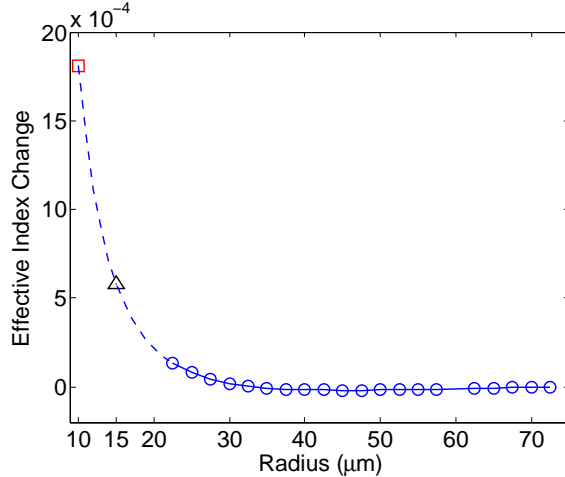


Figure 3.23: Effective index change of the rib waveguide versus bending radius for device with $N_R=10$. The index change from $R=10 \mu\text{m}$ to $R=22.5 \mu\text{m}$ is remarkable, while for R larger than $22.5 \mu\text{m}$, the index change is very small.

is obviously undesirable for a perfectly uniform grating. To improve upon this in future, one can consider slightly decreasing the grating period in the S-shape to compensate for the higher effective index. Alternatively, one may increase the bending radius of the S-shape while keeping the grating period constant, and reduce the spiral pitch to maintain the packing efficiency. The second approach also has an advantage of reducing the mode mismatch loss at the centre point of the S-shape, as will be discussed below. Table 3.2 lists the mode mismatch losses at different places in the spiral. At the centre point of the S-shape, the change in bending orientation causes a remarkable mode mismatch loss, which is about 0.13 dB for $R=10 \mu\text{m}$. This is clearly the dominant source of mode mismatch loss in the spiral, as the second largest one is only about 0.01 dB (at the ending points of the S-shape), and the third largest one is already negligible (at the connection points between $R = 22.5 \mu\text{m}$ and $R = 25 \mu\text{m}$). If the R of the S-shape is increased to $15 \mu\text{m}$, the mode mismatch loss is reduced to about 0.06 dB, and effective index variation is also reduced to 5.8×10^{-4} , as shown in Figure 3.23.

WG A	WG B	Loss (dB)
R = 10 μm	R = 10 μm^*	0.1336
R = 10 μm	R = 22.5 μm	0.0102
R = 22.5 μm	R = 25 μm	6.6157 $\times 10^{-5}$

* indicates bending in the opposite direction.

Table 3.2: Mode mismatch loss between two bent waveguides (WG).

3.6.2 Results and Discussion

Figure 3.24 shows the SEM image of the fabricated gratings. Figure 3.25 shows

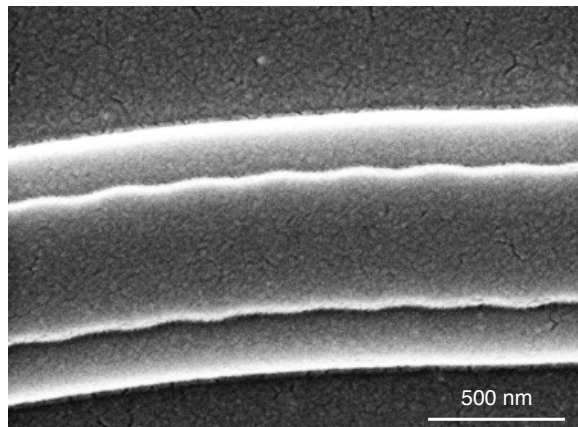


Figure 3.24: SEM image of the fabricated spiral gratings.

the measured transmission spectra of the two fabricated devices. We can see that there is only one sharp dip in each curve within a wide wavelength range (120 nm), indicating single-mode operation. Additionally, the envelopes of the two curves overlap very well, which means that the longer device does not introduce much excess loss, thus indicating that the propagation loss of the spiral waveguide grating is low. As shown in Figure 3.25(b), the shorter device shows an extinction ratio of about 6.5 dB and a 3-dB bandwidth of 0.28 nm. For the longer device, the extinction ratio increases to about 23 dB since more light is reflected, while the

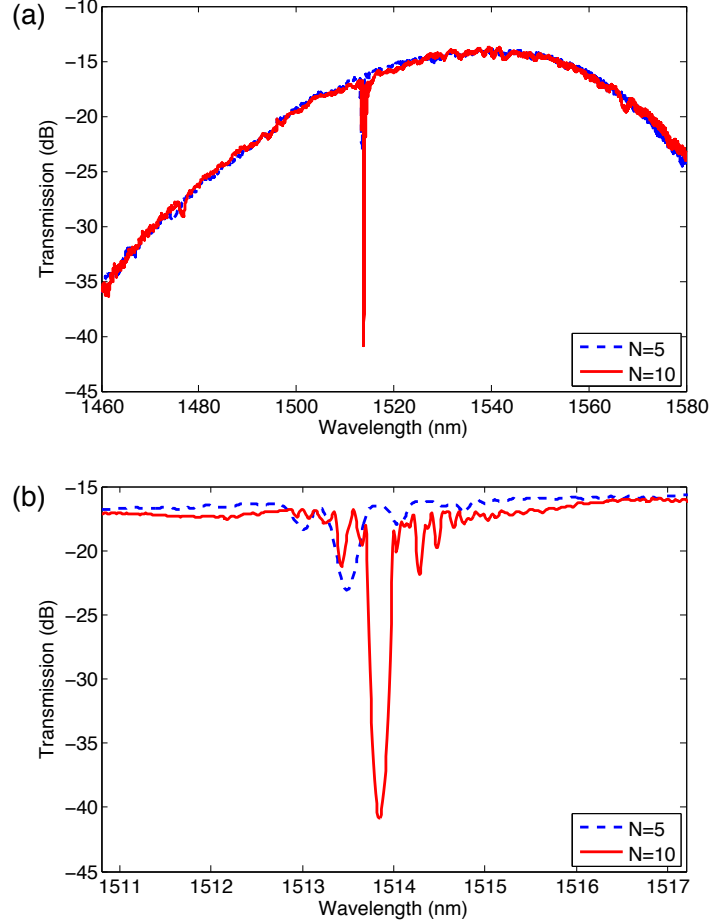


Figure 3.25: (a) Measured transmission spectra of the two spiral gratings. (b) Enlarged plot around the Bragg wavelength.

3-dB bandwidth is slightly reduced to 0.26 nm. The reduction in the first-null bandwidth is more distinguishable, i.e., from 0.6 nm for $N = 5$ to 0.32 nm for $N = 10$, which agrees with the theories for Bragg gratings with weak index modulations (see Eq. 1.16). We also observe a slight Bragg wavelength shift of about 0.35 nm between the two devices, which is most likely due to the Si thickness variations. In terms of footprint, the longer device occupies an area of $141 \mu\text{m} \times 146 \mu\text{m}$, which is smaller than previously reported Bragg gratings in curved waveguides [115] and spiral waveguides [116]. The length, in contrast, is much longer, and shows a

greatly improved packing efficiency of 21.8. Again, we expect that the packing efficiency can be further improved by reducing the spiral pitch (e.g. to 3 μm).

In summary, we have experimentally demonstrated integrated first-order Bragg gratings in silicon spiral waveguides using a CMOS-compatible fabrication process. The devices exhibit high packing efficiencies as well as very narrow bandwidths. Compared with long straight waveguide gratings, the spiral shape is more desirable for large-scale integrated photonic circuits; meanwhile, it can reduce the effects of Si thickness variations on the grating performance. Further work will include the optimization of the S-shape to reduce the mode mismatch loss and effective index perturbations.

3.7 Summary

In this chapter, we have studied Bragg gratings in rib waveguides. This family of devices is especially useful for narrow-band applications, such as WDM filters. Although this particular rib geometry has a finite slab and requires two etches, it is also possible to design gratings with similar performance based on the more commonly used rib geometry and using only one etch (i.e., with infinite slab and corrugations on the rib). The coupling coefficient has been demonstrated as low as about $1 \times 10^3 \text{ m}^{-1}$, which corresponds to a bandwidth of only 0.2 nm.

The multi-period grating structure is very useful for making custom optical functions, with the additional benefits of reducing the device size and the effects of fabrication nonuniformity. We find that our rib waveguide gratings have much better uniformity than strip waveguide gratings, and that the Si thickness variation is the only major cause of the wavelength variation. We also show that the spiral grating is not only favourable for the real estate on chip but also has the potential to minimize the effects of the Si thickness variation.

Chapter 4

Slot Waveguide Bragg Gratings

Optical sensing is one of the promising applications for silicon photonic Bragg gratings [15, 77]. The sensitivity is determined by the overlap between the electric field and the surrounding medium [14, 15]. In Section 2.6.3, we have demonstrated a biosensor using a strip waveguide phase-shifted grating. Since the electric field is concentrated in the silicon, only weak evanescent field tails are available for the sensing, resulting in a low sensitivity of only about 58 nm/RIU. To improve the sensitivity, we propose to use slot waveguides for Bragg gratings. Unlike strip or rib waveguides, slot waveguides are very sensitive to the RI change of the cladding because the electric field is concentrated in the low-index slot region. In this Chapter, we will present a comprehensive study on slot waveguide Bragg gratings, including both uniform and phase-shifted gratings.¹ We will investigate a number of design variations for both types of device. We also demonstrate a biosensor using a slot waveguide phase-shifted grating. Experimental results show a high bulk sensitivity of 340 nm/RIU and a high Q factor of about 1.5×10^4 , which together results in an intrinsic LOD of only 3×10^{-4} RIU. Finally, we demonstrate its capability of interrogating specific biomolecular interactions.

¹A version of Sections 4.1–4.3 has been published: X. Wang, S. Grist, J. Flueckiger, N. A. F. Jaeger, and L. Chrostowski, “Silicon photonic slot waveguide Bragg gratings and resonators,” *Opt. Express*, vol. 21, no. 16, pp. 19029–19039, 2013.

4.1 Slot Waveguide

Slot waveguide was first proposed by Almeida et al. in 2004 [36]. The large dielectric discontinuity at the high-index-contrast interfaces lead to a very strong optical confinement in the slot, which is promising for sensing and nonlinear optics. Figure 4.1 illustrates the cross section of a slot waveguide. It consists of two sili-

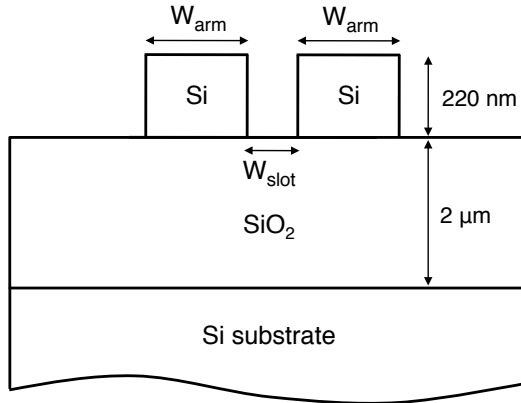


Figure 4.1: Schematic of a slot waveguide cross section (not to scale).

con arms separated by a low-index slot region. The geometric parameters include the arm width (W_{arm}) and the slot width (W_{slot}), both of which are defined by the lithography, and the waveguide height (H), which is fixed at 220 nm. The cladding material can be air, water, glass, or other low-index materials. In Section 4.2 and Section 4.3, we will use silicon oxide as the cladding material. In Section 4.4, the cladding material is the analyte to be measured. Figure 4.2 shows the simulated TE mode profile of a slot waveguide with oxide cladding. It can be clearly seen that the electric field is strongly confined inside the slot region. There are also weak evanescent fields decaying on the outer sides of the waveguide, which slightly add to the light-matter interaction, and, as will be discussed below, can also be used for the construction of Bragg gratings. The SEM image of the cross section of a fabricated slot waveguide is shown in Figure 4.3.

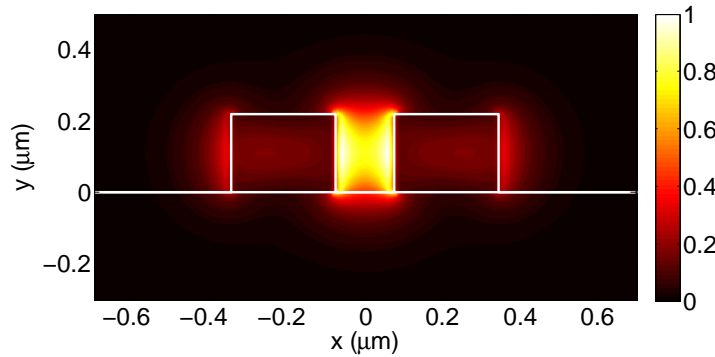


Figure 4.2: Simulated electric field of the fundamental TE mode in a slot waveguide with the following design parameters: oxide cladding, $W_{arm} = 270$ nm, and $W_{slot} = 150$ nm. The field intensity is strongly confined inside the slot region.

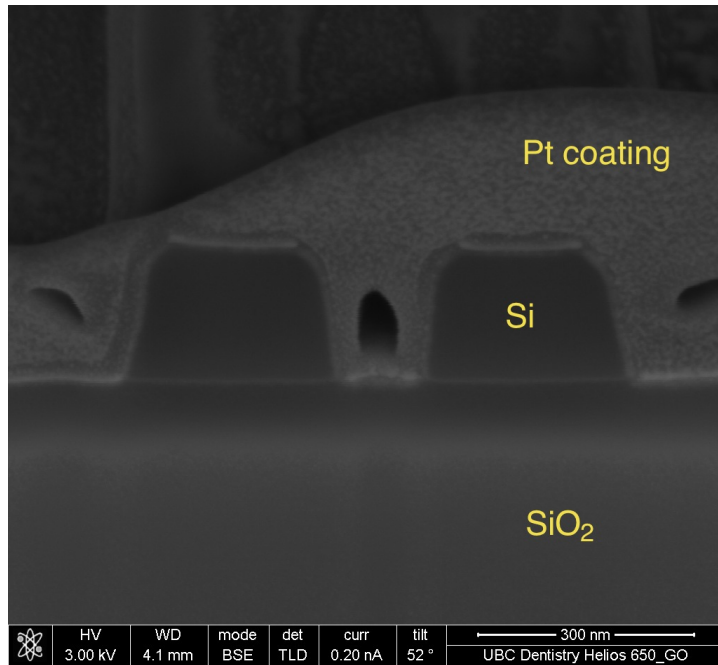


Figure 4.3: SEM image of the focused ion beam (FIB) milled cross section of a fabricated device (the small hole in the centre was due to the incomplete coating of platinum deposited to protect the waveguides during the FIB milling). Design parameters: $W_{arm} = 270$ nm, and $W_{slot} = 150$ nm.

4.2 Uniform Gratings

In this section, we present the design of uniform Bragg gratings in slot waveguides. A number of design variations will be discussed. Experimental results show high extinction ratios of 40 dB and bandwidths ranging from 2 nm to more than 20 nm.

4.2.1 Design and Fabrication

The gratings are formed with periodic sidewall corrugations either on the inside or the outside of the slot waveguide, as shown in Figure 4.4. Both configurations can modulate the effective index of the optical mode. Here, we present our designs of uniform gratings in two different waveguides (WG1 and WG2) with various corrugation widths (ΔW_{in} or ΔW_{out}). Table 4.1 lists all of our design variations. All

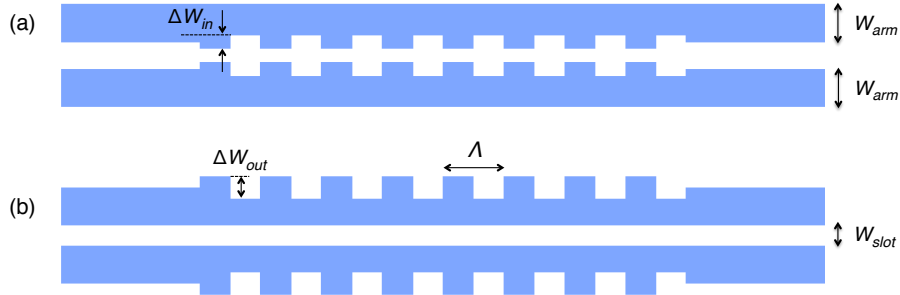


Figure 4.4: Schematic diagrams (not to scale) of the slot waveguide Bragg gratings with corrugations (a) inside and (b) outside.

WG #	W _{slot}	W _{arm}	n _{eff}	Λ	ΔW _{in}	ΔW _{out}
1	150 nm	270 nm	1.85	420 nm	10, 20 nm	0
					0	10, 20, 30, 40 nm
2	200 nm	270 nm	1.80	430 nm	10, 20, 30, 40 nm	0
					0	10, 20, 30, 40 nm

Table 4.1: Design variations for uniform slot waveguide Bragg gratings.

devices have 1000 grating periods. The effective index (n_{eff}) of each waveguide was calculated at 1550 nm. The grating period (Λ) was chosen to obtain a Bragg wavelength close to 1550 nm while being compatible with the foundry design rules.

Figure 4.5 shows the top view SEM images of two fabricated devices. Again, we used square sidewall corrugations in the mask layout, as illustrated in Figure 4.4. However, as is clearly seen in Figure 4.5, the fabricated corrugations were rounded and resemble sinusoidal shapes due to lithographic effects.

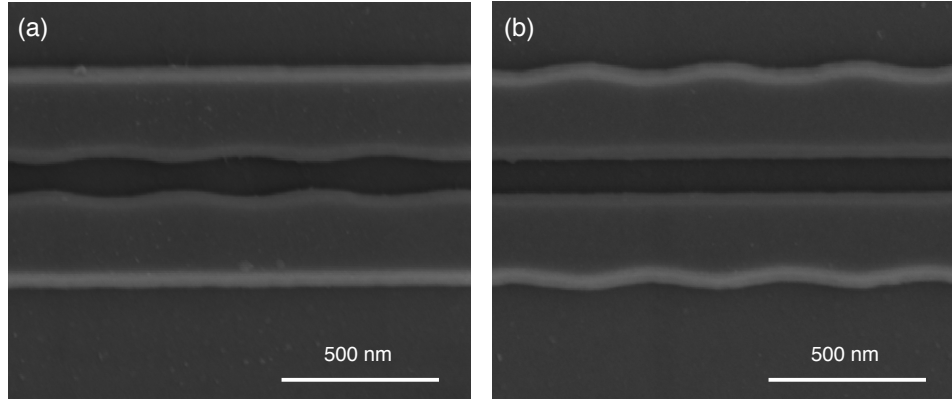


Figure 4.5: Top view SEM images of the fabricated slot waveguide Bragg gratings: (a) corrugation inside for $W_{slot} = 150$ nm, $W_{arm} = 270$ nm, and $\Delta W_{in} = 20$ nm. (b) corrugations outside for $W_{slot} = 150$ nm, $W_{arm} = 270$ nm, and $\Delta W_{out} = 40$ nm.

In order to minimize the total footprint and bending losses, we use 500 nm wide strip waveguides for the routing, as well as for the Y-branch design. The coupling between the strip and slot waveguides is realized through mode converters [118]. As shown in Figure 4.6, one arm of the slot waveguide expands linearly in the coupling region and eventually becomes the strip waveguide. The other arm is slightly tilted in the coupling region, with its width and distance from the first arm unchanged; then after the coupling region, it bends away and tails off. The coupling length is 5 μm to ensure that the coupling loss is negligible [118–120]. Figure 4.7 shows the SEM image of a fabricated strip-to-slot mode converter.

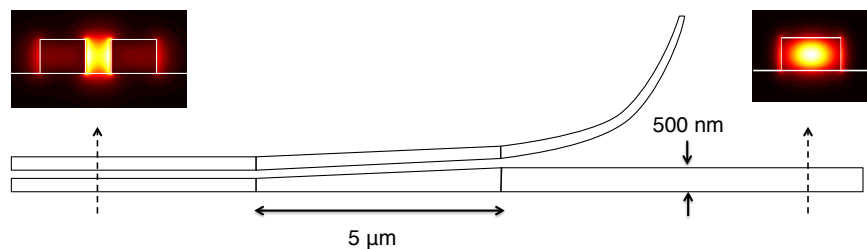


Figure 4.6: Schematic of the strip-to-slot mode converter (not to scale).

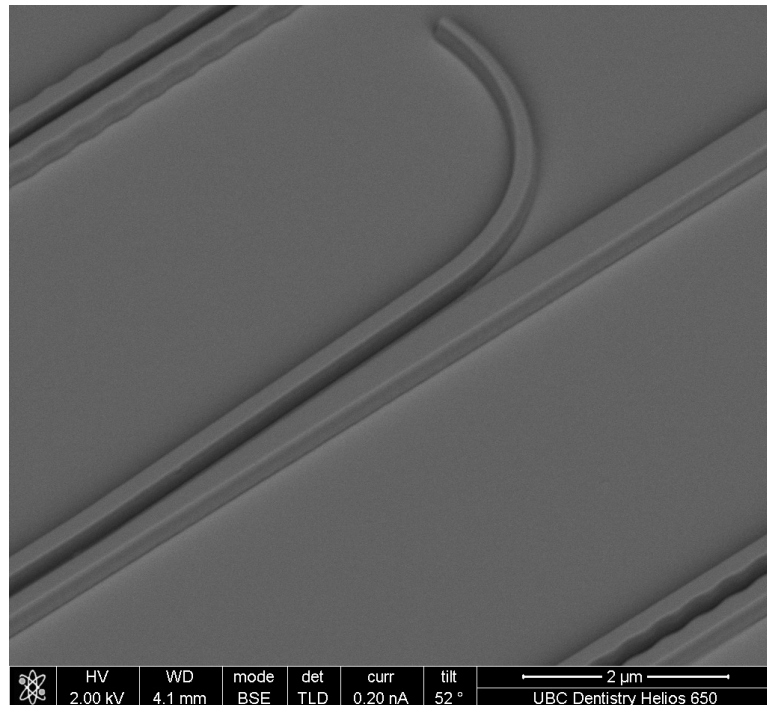


Figure 4.7: SEM image of a strip-to-slot mode converter as illustrated in Figure 4.6.

4.2.2 Measurement Results

Figure 4.8 shows the measured raw spectral responses of a uniform grating. The transmission spectrum shows a deep notch with an extinction ratio greater than 40 dB. The centre wavelength is about 1550 nm, in good agreement with the design value. Accordingly, a peak is seen in the reflection spectrum. The peak power is about 3 dB below the transmission level, corresponding to the extra loss of the Y-branch. The Y-branch also has weak parasitic back-reflection due to the abrupt waveguide discontinuity, which limits the noise floor of the reflection spectrum.

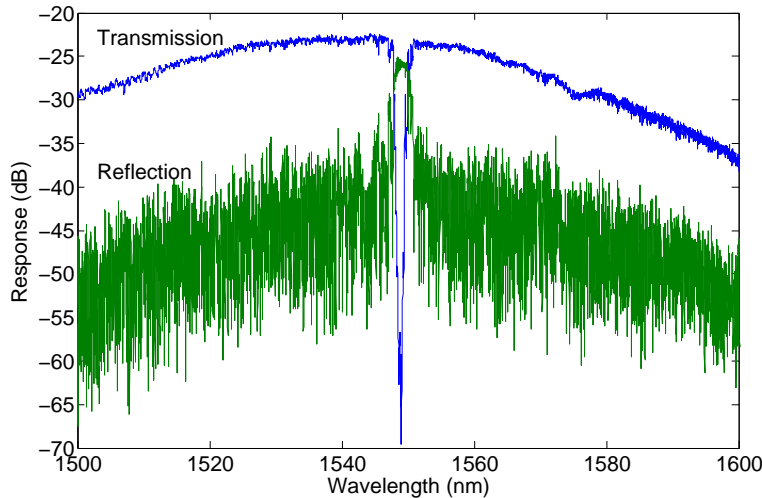


Figure 4.8: Measured raw spectra of a uniform grating designed on WG1 with $\Delta W_{out} = 10$ nm, showing a deep notch with an extinction ratio greater than 40 dB at about 1550 nm.

Figure 4.9 shows the measured transmission spectra for the devices based on WG1. The spectra were normalized by using a straight waveguide as a reference to subtract the insertion loss, i.e., the envelope of the transmission spectrum in Figure 4.8. We can see that all the devices exhibit high extinction ratios of about 40 dB. As the corrugation width is increased, the stop-band becomes broader due to the increased grating coupling coefficient.

The bandwidths for all design variations are also plotted versus corrugation width in Figure 4.10. We can see that the bandwidth ranges from 2 nm to more than 20 nm. The green curve is well above the other three curves, and the device using

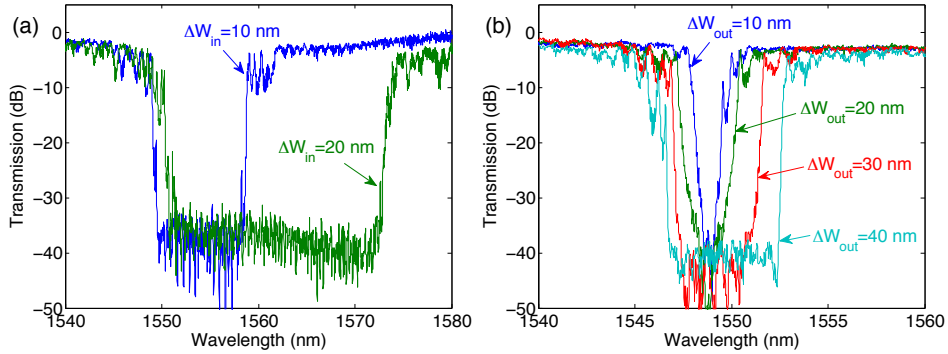


Figure 4.9: Measured transmission spectra of the uniform gratings designed on WG1. (a) corrugations inside, (b) corrugations outside. For both configurations, the stop-band becomes broader with increasing corrugation width.

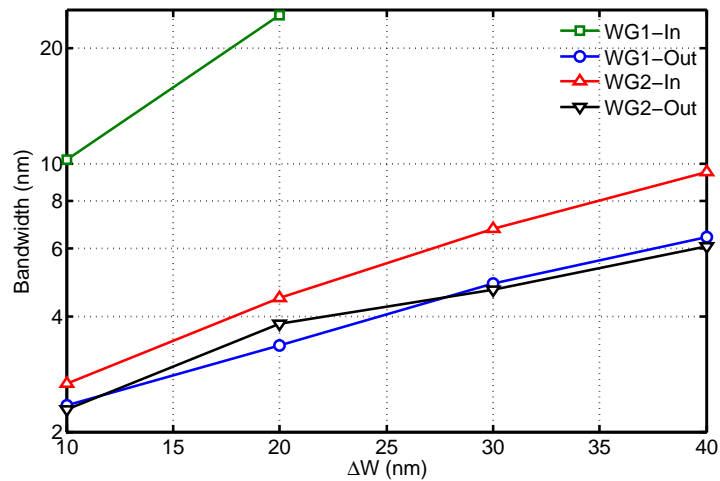


Figure 4.10: Measured bandwidth versus designed corrugation width on WG1 and WG2. WG1 with inside corrugations shows the largest bandwidth due to the strongest perturbation.

WG1 with 20 nm inside corrugations have the largest grating coupling coefficient. An intuitive explanation is that the optical field is strongly confined in the slot, as shown in Figure 4.2, and a small corrugation can have a large impact on the field. Increasing the slot width reduces the optical confinement in the slot, and, therefore, the effect of a particular corrugation inside the slot of WG2 is smaller than it is in WG1, which is why the red curve is below the green curve. When the corrugations are placed on the outside of the slot waveguide, in both WG1 and WG2, the bandwidths are narrower and very similar to each other, due to the fact that the evanescent field tails are relatively weak.

4.3 Phase-Shifted Gratings

In this section, we will discuss phase-shifted gratings in slot waveguides. Experimental results show Q factors up to 3×10^4 . This is higher than all reported values for slot waveguide ring resonators, which usually suffer from large bending losses and mode mismatch losses.

4.3.1 Design and Fabrication

Figure 4.11(a) shows the schematic of a phase-shifted Bragg grating using corrugations on the outside of the slot waveguide. The length of the phase shift is equal to one grating period. On each side of the phase shift, there are N grating periods that function as a distributed Bragg reflector (DBR). The principle of operation is the same as in strip waveguide, as discussed in Section 2.6, i.e., a cavity is created by the phase shift and a resonant peak will appear at the centre of the stop-band of the transmission spectrum. The only difference is that the optical mode is concentrated in the slot region. Figure 4.11(b) shows a top view SEM image of a fabricated device, with the phase shift highlighted in the dashed box.

In order to better understand this structure, we also performed 3D-FDTD simulations. Figure 4.11(c) shows a simulated transmission spectrum featuring a sharp resonant peak at the centre of the stop-band. Figure 4.12 shows the electric field distributions for the on-resonance state and an off-resonance state. Again, we can see that the electric field is strongly confined in the slot region, whether the wavelength is on- or off-resonance. In Figure 4.12(a), the wavelength is 1543 nm, lo-

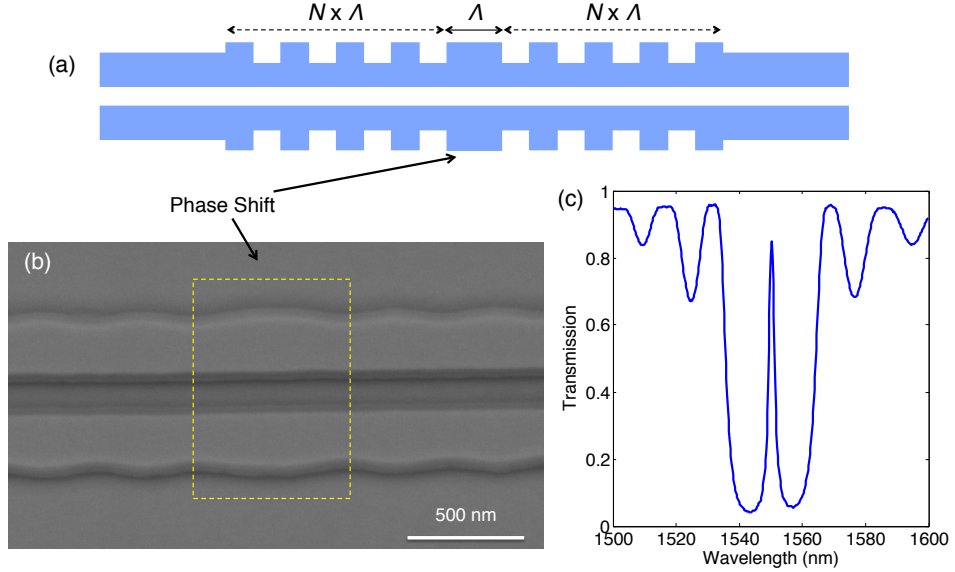


Figure 4.11: Phase-shifted Bragg gratings with corrugations on the outside of the slot waveguide: (a) schematic diagram (not to scale), (b) SEM image showing the phase shift region of a fabricated device, (c) transmission spectrum simulated by FDTD with the following geometric parameters: WG1, $\Delta W_{out} = 40$ nm, and $N = 50$.

cated in the left valley of the stop-band in Figure 4.11(c). The incoming light is mostly reflected back by the first DBR mirror on the left. As the wavelength shifts to the resonant peak at 1550 nm, the cavity starts to resonate and light is concentrated around the phase shift, as shown in Figure 4.12(b).

As discussed in Section 2.6, we have known that the intrinsic Q factor of a phase-shifted grating is limited by the waveguide loss (see Eq. 2.10). Compared with conventional low-loss waveguides on silicon (i.e., strip and rib waveguides), slot waveguides exhibit relatively high losses. Typical reported loss values for slot waveguides are on the order of 10 dB/cm [119, 121, 122]. Assuming that the loss is 10 dB/cm and $n_g = 3.35$ (simulated value for WG1 in Table 4.1), the calculated Q_I is about 5.89×10^4 at 1550 nm. If this resonator is critically coupled [14], the total Q is reduced by a factor of two and becomes about 2.95×10^4 . As will be further discussed in next section, these approximations give values comparable to

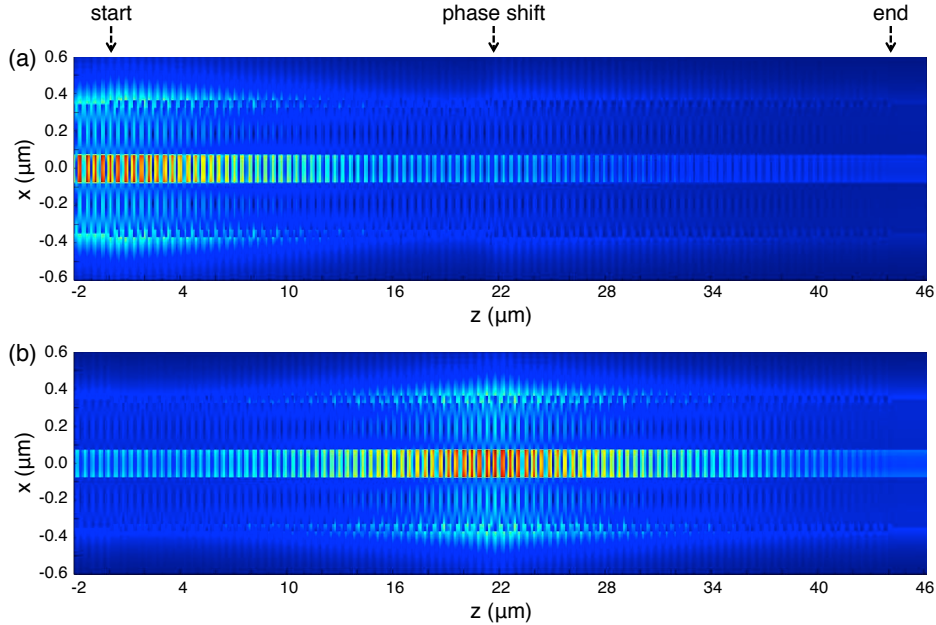


Figure 4.12: Electric field distributions for light incident from the left at (a) 1543 nm and (b) 1550 nm. The simulation parameters are the same as in Figure 4.11(c). The field was recorded at the middle of the silicon waveguide in the vertical direction (i.e., corresponding to the plane of $y=110$ nm in Figure 4.2).

the maximum Q values that we have observed experimentally.

4.3.2 Measurement Results

We designed a number of phase-shifted gratings based on WG1 and WG2 (see Table 4.1), using both inside-corrugation and outside-corrugation configurations. For each configuration, we used the largest corrugation width listed in Table 4.1 in order to obtain the largest grating coupling coefficient. Figure 4.13 shows the measured raw spectral responses of a phase-shifted grating. A sharp resonant peak is clearly seen at the centre of the stop-band in the transmission spectrum and, accordingly, a deep notch appears in the reflection spectrum.

We varied the length of the gratings to study its impact on the Q factor. Figure 4.14(a) shows a set of transmission spectra for devices based on WG1 with

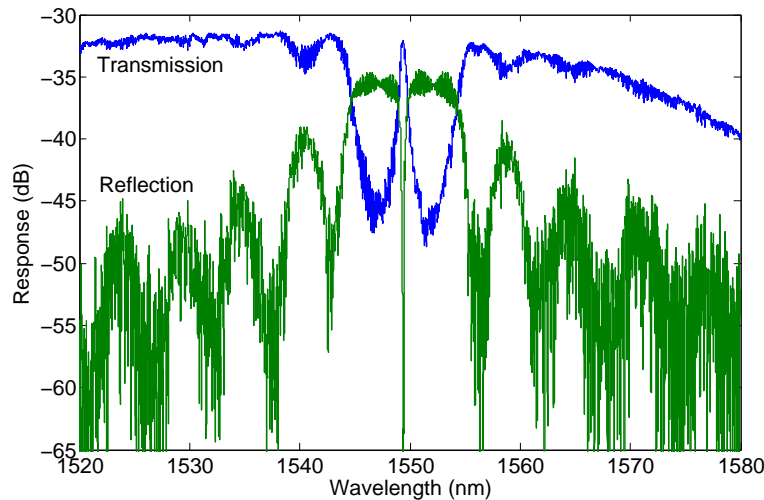


Figure 4.13: Measured raw spectra of a phase-shifted grating designed on WG1 with $\Delta W_{out} = 40$ nm and $N = 300$.

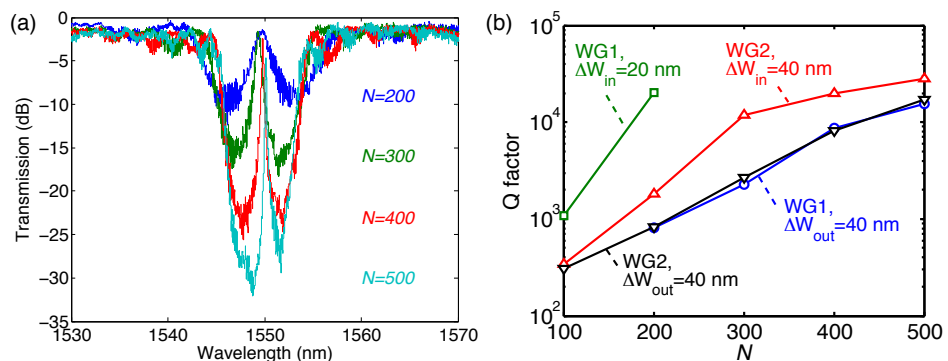


Figure 4.14: (a) Measured transmission spectra for phase-shifted gratings designed on WG1 with $\Delta W_{out} = 40$ nm and various lengths, (b) Q factor as a function of N .

$\Delta W_{out} = 40$ nm and for various lengths. As N is increased from 200 to 500, the stop-band becomes deeper because more light is reflected back. Also, the resonant peak becomes sharper and the Q factor increases from 800 to 1.55×10^4 , although the peak amplitude slightly decreases. The Q factor is also plotted as a function of N for all design variations in Figure 4.14(b). We can see that the green curve is well above the other three curves, which verifies that WG1 with $\Delta W_{in} = 20$ nm has the largest grating coupling coefficient. However, when N exceeds 200, the cavity becomes over coupled and the amplitude of the resonant peak drops dramatically so that it cannot be observed. The blue and black curves are on the bottom and overlap with each other, which verifies that WG1 and WG2 with $\Delta W_{out} = 40$ nm have small, and similar, grating coupling coefficients. Finally, the red curve is in between the other three, again in agreement with the result in Figure 4.10, and shows the maximum Q factor of about 3×10^4 at $N = 500$. This is the highest Q factor reported for slot waveguide resonators. This is also very close to the calculated Q factor under critical coupling condition, assuming that the wavelength propagation loss is 10 dB/cm. Recently, a few approaches have been reported to reduce the loss figures for slot waveguides [119, 123, 124]. For example, Spott et al. reported the lowest loss of 2 dB/cm by using asymmetric slot structures, but at the expense of reduced optical confinement and a relatively complicated fabrication process [124]. However, we expect that further improvements in the lithography and etching processes will reduce the loss of slot waveguides and lead to better performance for slot waveguide Bragg gratings.

4.4 Biosensing Applications²

In this section, we present a novel silicon photonic biosensor using a phase-shifted Bragg grating in a slot waveguide. We experimentally demonstrate a high sensitivity of 340 nm/RIU measured in salt solutions and a high quality factor of 1.5×10^4 (in an aqueous medium), enabling a low LOD of 3×10^{-4} RIU. We also demonstrate the device's ability to interrogate specific biomolecular interactions, resulting

²A version of Section 4.4 has been published: X. Wang, J. Flueckiger, S. Schmidt, S. Grist, S. T. Fard, J. Kirk, M. Doerfler, K. C. Cheung, D. M. Ratner, and L. Chrostowski, “A silicon photonic biosensor using phase-shifted Bragg gratings in slot waveguide,” *J. Biophotonics*, vol. 6, no. 10, pp. 821-828, 2013.

in the first of its kind label-free biosensor.

4.4.1 Silicon Photonic Biosensors

Silicon photonic biosensors have demonstrated great potential for label-free on-chip detection of biomolecules [14, 125]. Various optical structures [126, 127], such as microring [128–132] and microdisk resonators [14, 133], Bragg gratings [77, 134], and photonic crystals [135], have been developed on the SOI platform for biological sensing applications. Nearly all of these sensors are based on measuring the RI change of the surrounding environment, which allows for real-time and direct detection of molecular interactions near the sensor surface. We know that the sensitivity is determined by the overlap between the electric field and the analyte. In many silicon photonic sensors (e.g., strip-waveguide-based ring resonators and Bragg gratings, disk resonators, conventional photonic crystals), the majority of the electric field is confined in the high-index material (i.e., silicon), thus it is difficult to interact with the analyte efficiently and the sensitivity is low. For example, in Section 2.6.3, we have demonstrated a strip waveguide grating sensor with a high Q factor of 27600, but the sensitivity is only 58 nm/RIU, which leads to an intrinsic LOD of 9.3×10^{-4} RIU, similar to that of a strip waveguide ring resonator (e.g., 1.1×10^{-3} RIU in [128]).

To enhance the sensitivity, an effective solution is to use slot waveguide structures [36]. In slot waveguides, the electric field is concentrated inside the low-index slot, leading to an increased field overlap with the analyte and hence a higher sensitivity. A slot waveguide ring resonator was first developed for biosensing applications by Barrios et al. [136] on a Si_3N_4 – SiO_2 platform, showing a bulk sensitivity of 212 nm/RIU. This structure has also been demonstrated on the SOI platform by Claes et al. [137], showing a higher sensitivity of 298 nm/RIU, as well as a much smaller footprint due to the high index contrast of the material system.

We also know that the LOD is another important parameter to evaluate the sensor performance. For single-resonator silicon photonic sensors, the LOD depends not only on the sensitivity but also on the Q factor and the system noise [14]. For the purpose of comparing different single-resonator sensors (neglecting the measurement system noise), the intrinsic LOD is defined as the RI change correspond-

ing to one resonance linewidth, which is inversely proportional to the sensitivity and the Q factor (see Eq. 2.16). Therefore, it is necessary to have both high sensitivity and high Q factor to minimize the intrinsic LOD. The afore-mentioned slot waveguide ring resonators have shown high sensitivities, however, their Q factors are typically very low, which is primarily limited by the high bending loss, mode mismatch loss, and scattering loss due to waveguide roughness [137]. Although Baehr-Jones et al. [121] demonstrated slot ring resonators with exceptionally high Q values (>20000 in air) in 2005, they pointed out that there are significant challenges in the design and fabrication. Thus, their record Q values have not been reproduced since then, and in fact, other reported Q values since then are much lower (e.g., Barrios et al. reported Q=330 [136] and Claes et al. reported Q=1800 [137], both in water). Moreover, in general, ring resonators have limited free spectral ranges (FSR) and demanding tolerance on the structural geometry (e.g., in order to achieve a high extinction ratio, the critical coupling condition must be satisfied, which requires a strict control of the coupling region). Recently, another structure called a slotted photonic crystal [138, 139] has gained attention in this field due to its small modal volume and greatly enhanced light-matter interaction. However, it presents additional design and fabrication challenges.

As already demonstrated in the previous sections, slot waveguide Bragg gratings and resonators do not suffer from the high bending losses and mode mismatch losses of slot waveguide ring resonators. Therefore, a much higher Q factor can be achieved with slot waveguide phase-shifted gratings. By combining the high sensitivity of the slot with the high Q factor of the phase-shifted grating, we experimentally obtained an intrinsic LOD of 3×10^{-4} RIU at 1550 nm. To our knowledge, this is the best experimental result for slot-based biosensors. Additional advantages of this sensor include simple optical design, a high extinction ratio, a small footprint, a large range for RI change (owing to single-mode operation), rapid integration with microfluidic channels, and compatibility with commercial CMOS fabrication technology. Commercial CMOS compatibility is particularly important for producing high-volume, low-cost, and possibly disposable sensor chips by leveraging the economies of scale of the CMOS foundry process. To evaluate the performance of this sensor, the silicon chip is integrated with a reversibly bonded polydimethylsiloxane (PDMS) microfluidic chip. We observe that the experimen-

tal performance of the sensor is in excellent agreement with numerical simulations. The performance of the biosensor in a modified biological sandwich assay is also presented.

4.4.2 Design and Fabrication

Figure 4.15 shows the schematic diagram of the sensor. The design parameters are as follows: $W_{arm} = 270$ nm, $W_{slot} = 150$ nm, $\Delta W_{out} = 40$ nm, $\Lambda = 440$ nm, and $N = 150$. The simulated Bragg wavelength is around 1530 nm when the cladding is water ($n = 1.33$). The total length of this sensor is about 132 μm . The footprint, however, is very small because the sensor is just a waveguide that is less than 1 μm wide, with a total area smaller than 132 μm^2 . An SEM image of the fabricated

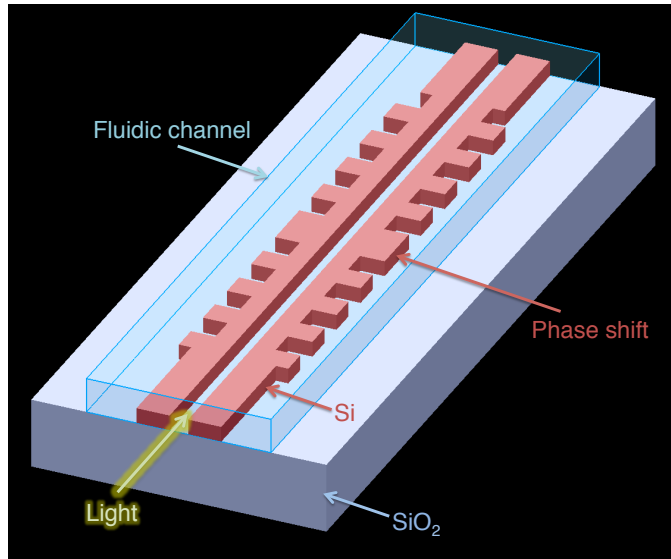


Figure 4.15: Schematic diagram of the sensor integrated with the microfluidic channel.

device is shown in Figure 4.16.

The microfluidic channels were fabricated using PDMS soft lithography [140]. Briefly, SU-8 photoresist (MicroChem) was spin cast onto standard silicon wafers to a thickness of approximately 80 μm , then patterned using UV exposure through a transparency mask containing the microfluidic channel designs. After resist de-

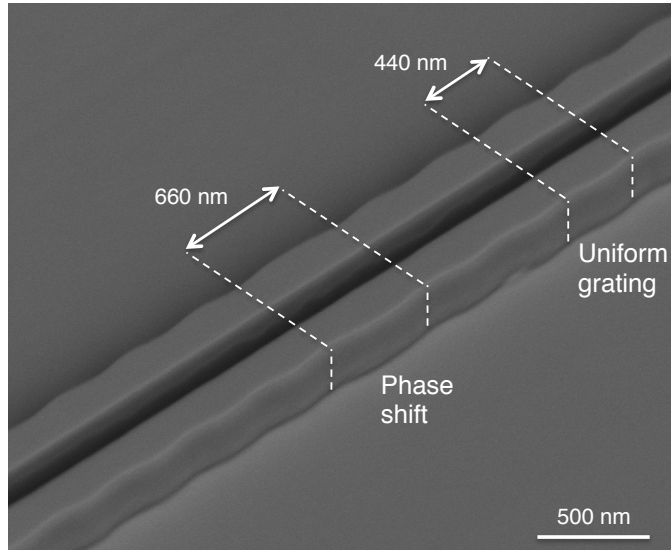


Figure 4.16: SEM image of the fabricated device. Note that the phase shift in the central region can be identified by measuring the spacing between the grating grooves. Here, the spacing with the phase shift is 660 nm, corresponding to 1.5 times the grating period.

development PDMS prepolymer and curing agent (Sylgard), mixed at a ratio of 10:1, were cast onto the mold and cured. The PDMS was then demolded and the individual microfluidic chips were diced and their inlet and outlet holes bored. Fluidic connections were made using friction fit fluid dispensing tips (EFD) interfaced with standard silastic tubing and connected to a syringe pump (Chemtex Nexus 3000). NaCl solutions of varying concentrations (in deionized water) were used for the refractive index sensitivity calibration of the sensor. For these experiments, the syringe pump was used to deliver deionized water, 62.5 mM, 125 mM, 250 mM, and 500 mM solutions through the microfluidic channels atop the sensors, interrupting flow briefly between reagent changes. The refractive indices of these solutions were measured using a digital refractometer (Reichert AR200).

4.4.3 Experiments and Discussion

Figure 4.17 shows the measured transmission spectrum of the sensor immersed in deionized water. As expected, a sharp resonance peak appears at the centre of the

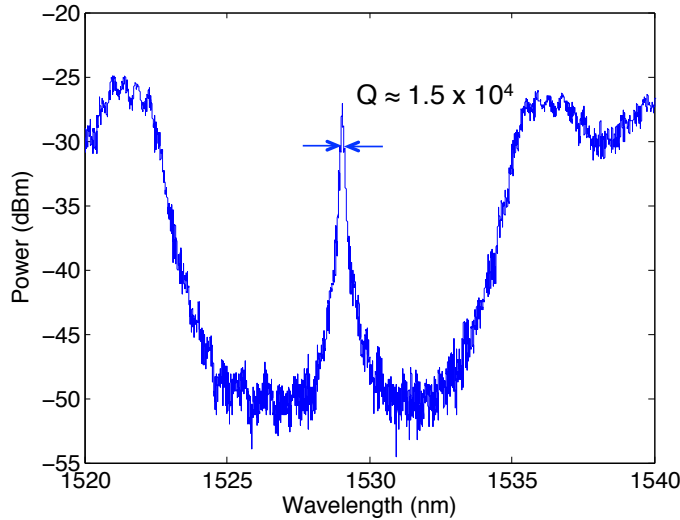


Figure 4.17: Measured transmission spectrum of the sensor immersed in deionized water.

stop band. The FWHM linewidth of this resonance is about 0.1 nm, corresponding to a Q factor of about 1.5×10^4 . This “in-water” Q factor is much higher than those of the reported slot waveguide ring resonators [136, 137] and the slotted photonic crystal cavities [138]. Also of interest is that the resonance peak exhibits a large extinction ratio of larger than 20 dB, which is rarely seen in other slot-based biosensors such as ring resonators.

Bulk Sensitivity

Figure 4.18(a) shows the measured transmission spectra of the sensor covered with different NaCl concentrations. For each concentration, we measured the optical spectra multiple times (every ~ 1.5 minutes) to verify the reliability and repeatability. The peak wavelength shift during the six steps is also shown in Figure 4.18(b). Since the refractive indices of the salt solutions are already known, we plot the peak wavelength shift as a function of the refractive index in Figure 4.19. We clearly observe that the experimental result agrees well with the simulation result. The sensitivity (S) is about 340 nm/RIU, which is higher than those of the reported slot waveguide ring resonators [136, 137, 141–143].

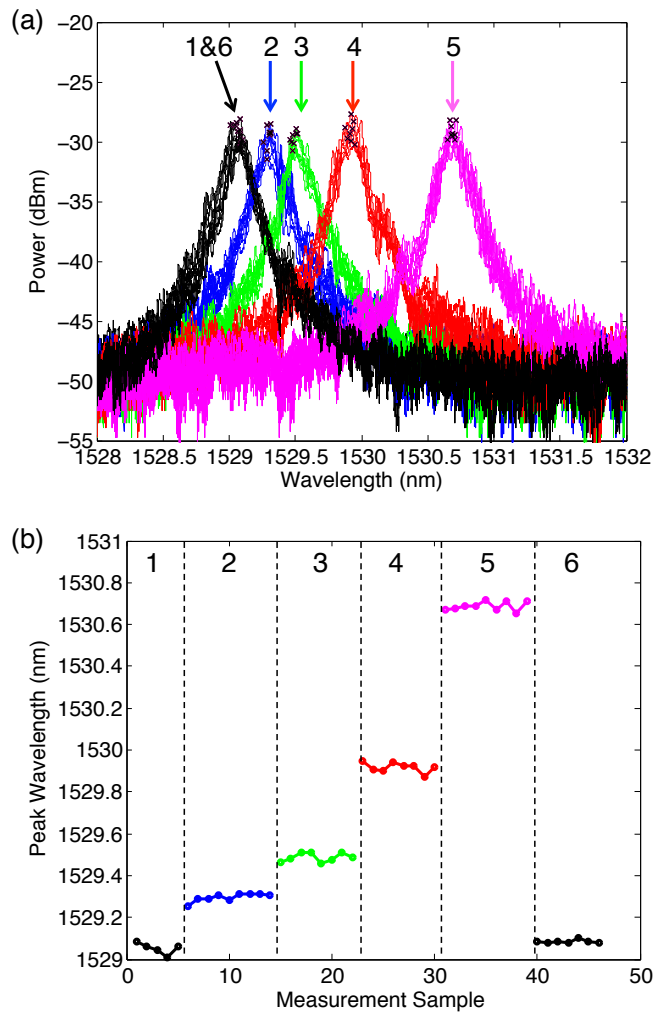


Figure 4.18: Measurement results for various NaCl concentrations: (a) transmission spectra for all the measurements, (b) peak wavelength shift during the salt steps. Each color represents a NaCl concentration. Steps 1 and 6 correspond to 0 mM, and Steps 2 to 5 correspond to 62.5 mM, 125 mM, 250 mM, and 500 mM solutions, respectively.

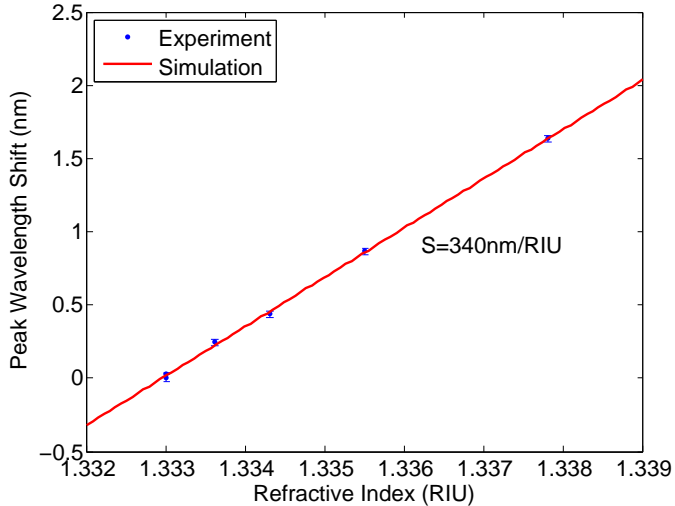


Figure 4.19: Measured and simulated peak wavelength shift as a function of the refractive index of the salt solution. For the experimental data, the symmetric error bars are two standard deviation units in length.

Based on the Q factor (1.5×10^4) and the sensitivity (340 nm/RIU), the intrinsic LOD is about 3×10^{-4} . This intrinsic LOD is, to date, the best experimental result for slot-based biosensors.

Biosensing

To demonstrate the biosensing capability, we conducted a modified sandwich assay involving well-characterized biomolecules with high binding affinities. The results, together with the accompanying reagent sequencing, are shown in Figure 4.20(a) and (b) respectively. Reagents were delivered to the sensor at $10 \mu\text{L}/\text{min}$ via reversibly-bonding PDMS microfluidics, briefly pausing flow to switch reagents. To limit the effects of thermal drift, the optical stage was thermally controlled to 30C, thereby negating minor perturbations in the ambient temperature of the room. Optical scans of the resonant peaks were taken every 45 seconds and a signal baseline was established using phosphate buffered saline (PBS) for 20 minutes prior to sequencing other reagents. Lorentzian fitting of the optical spectra was used to determine the resonance wavelength.

To orient the capture antibody on the sensor surface, Protein-A (1 mg/mL)

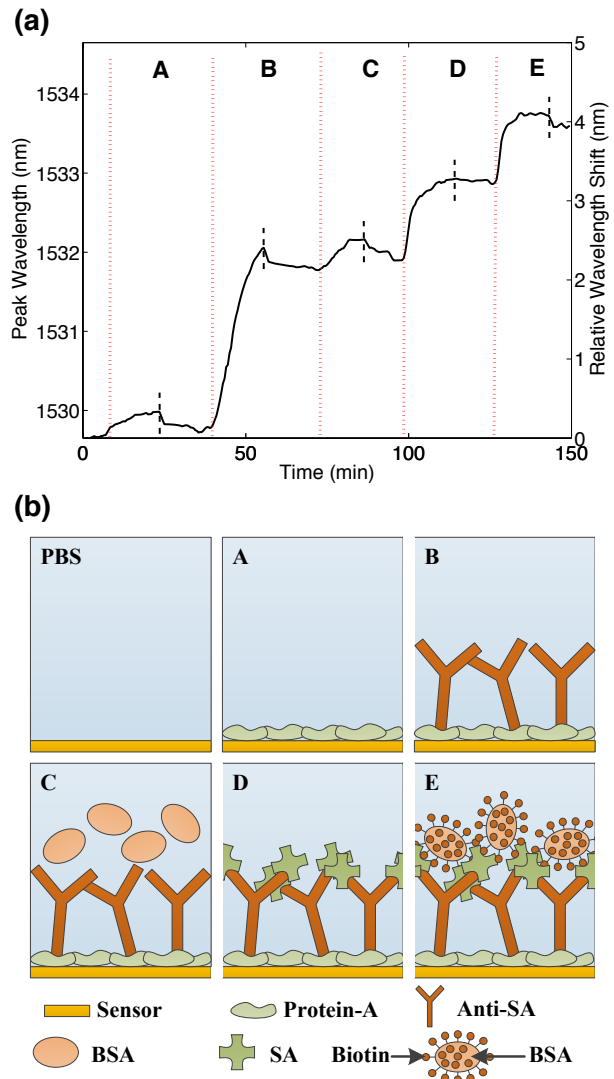


Figure 4.20: Biosensing experimental results: (a) depicts the resonance wavelength shifts as the experiment progressed while (b) illustrates reagent sequencing corresponding to regions [A-E] in (a). Region A = Protein-A (1 mg/mL), B = anti-streptavidin (SA) (125 μ g/mL), C = Bovine Serum Albumen (BSA) (2 mg/mL), D = streptavidin (SA) (1.8 μ M), E = Biotin-BSA (2.5 mg/mL). Introduction of reagent in each region was followed by a PBS-wash, as shown by the short, black-dashed line mid-way through each region.

was passively adsorbed to its surface [144] followed by a PBS wash to remove un-bound or loosely bound protein as shown in region [A] of Figure 4.20(a) and (b). Next, the capture antibody, anti-Streptavidin (antiSA, 125 μ g/mL), was introduced to functionalize the sensor's surface. Upon adsorption, the 160 kDa protein results in a 2 nm resonant wavelength shift, as can be clearly seen in region [B]. To ensure our biological interactions were specific, the functionalized sensor was challenged with bovine serum albumin (BSA, 2 mg/mL), as shown in Region [C]. After a PBS wash, the signal drops towards the pre-BSA baseline, as expected. We hypothesize that the slight residual BSA is the result of incomplete rinsing by PBS or by permanent adsorption of BSA to the sensor surface resulting from incomplete coverage of the first Protein-A monolayer [145]. Next, we introduced the target analyte, Streptavidin (SA, 1.8 μ M), resulting in irreversible binding to antiSA even after the PBS rinse, as shown in region [D]. Finally, to illustrate a secondary amplification step, capture of biotinylated BSA (b-BSA, 2.5 mg/mL) to the immobilized SA is shown in region [E]. To validate that the wavelength shifts are as expected, we performed a quantitative analysis on the first protein monolayer based on observations by Coen et al. [145]. They determined coverage of the first monolayer on the waveguide surface to be 10-50% and that the successful immobilization of an IgG's Fc domain to a Protein-A receptor occurred on the second or third add layer. This presents a challenge in quantifying an exact number of bound molecules, especially for subsequent steps where molecules have multiple binding domains that may or may not be occupied. In addition, Claes et. al. discovered that biomolecules do not completely adhere and bind within the slot [137], creating additional uncertainty for an accurate analysis. Using Lumerical MODE solver, we modelled a 1 nm thick monolayer of Protein-A (42 kDa with a RI = 1.48 [146]) assuming: (1) moderate packing density on the waveguide surface due to steric hindrances, (2) limited diffusion into the slot, and (3) a sparse 3 nm film representing the second add layer. The simulated wavelength shift is twice the experimentally observed value, indicating 50% surface coverage with a 1 nm film. Based on the relative size and molecular weights of the subsequent molecules [147, 148], the resulting proportional wavelength shifts are also as expected. This simple assay demonstrates the specific and selective biosensing capability of our novel sensor and its potential for use in clinically relevant diagnostic settings.

Future work will include the integration of this sensor in architectures that allow for multiplexing and reference sensors, ultimately enabling more sophisticated label-free assays. In addition, surface functionalization strategies and chemistries we recently published in [149] will be explored to demonstrate its capability as a medical diagnostic sensor for use in complex media like saliva, serum, and whole blood.

4.5 Summary

The integration of Bragg gratings in slot waveguides offers many new possibilities. It combines the superior sensing ability of slot waveguides with the flexibility in the design of the spectral response of Bragg gratings. The uniform gratings show high extinction ratios of 40 dB and bandwidths ranging from 2 nm to more than 20 nm. The phase-shifted gratings show Q factors up to 3×10^4 , much higher than most reported values for slot waveguide ring resonators. This family of devices also has great potential for optical modulation, nonlinear optics and optical signal processing.

Chapter 5

Conclusion and Future Work

5.1 Conclusion

In this thesis, we have studied silicon photonic waveguide Bragg gratings. Three types of waveguides – strip, rib, and slot waveguides – have been investigated, each as a dedicated chapter. In each chapter, we presented the design and experimental results of various grating devices. We have also demonstrated a number of applications using our grating devices. The major contributions of this research include:

1. Towards CMOS-compatible silicon photonics. Most of the early work on integrated waveguide Bragg gratings relies on e-beam lithography fabrication. Though attractive for prototyping, e-beam lithography has one fatal drawback – low throughput, e.g., it could literally take hours to write only one wafer, preventing it from real productions. In this thesis, all of the silicon chips were fabricated using commercial CMOS fabrication facilities, paving the way for the future development and commercialization of silicon photonic Bragg gratings.
2. A comprehensive study of uniform Bragg gratings in strip waveguides. We have investigated almost all possible design variations, including grating period, corrugation width, waveguide width, cladding material, grating length, and corrugation shape. The experimental results for most design variations

agree with theoretical analysis and/or simulation results. However, we should emphasize the results for grating length variations. We have observed that the propagation losses of 500 nm strip waveguide gratings are within the range of 2.5–4.5 dB/cm, independent of the corrugation width. To our knowledge, this is the first report on the propagation loss of silicon photonic Bragg gratings. More interestingly, we have observed that as the grating length is increased beyond a certain value, the bandwidth becomes broader, which is primarily due to Si thickness variations.

3. Lithography effects. We have demonstrated a model to predict the fabrication imperfections of silicon photonic devices during the lithography process. This model has been validated for silicon photonic Bragg gratings by comparing the simulation results of the virtually fabricated gratings and the experimental results.

4. Technical achievements:

- (a) Layout. We have discussed a number of practical techniques from the layout point of view, such as using design hierarchy in the GDSII file, generating cells using scripts in Pyxis Layout, using Y-branch to characterize the reflection port, two common layout configurations – individual fibers vs. fiber array, and a compact layout approach to increase the space-efficiency on the chip.
- (b) Characterization. We have shown the importance of using a tunable laser with low SSE to characterize grating devices with high extinction ratios. In the absence of such a tunable laser source, we should optimize the sweeping settings to obtain the largest dynamic range.

5. Phase-shifted gratings in strip waveguides.

- (a) A comprehensive study of phase-shifted gratings in strip waveguides. We have discussed the basics of phase-shifted gratings, such as the structure, physical interpretation from the cavity point of view, the Q factor and the waveguide loss limitations. We have also investigated

several important design variations, including grating length and corrugation width. A maximum Q factor of 1.9×10^5 has been experimentally demonstrated. Optical nonlinearity has also been observed for high-Q phase-shifted gratings.

- (b) Application in biosensing. We have demonstrated a biosensor using a strip waveguide phase-shifted grating, showing a sensitivity of about 58 nm/RIU and a Q factor of 27600, which leads to an intrinsic LOD of about 9.3×10^{-4} RIU.
 - (c) Application in microwave photonics and ultrafast optical signal processing [27, 108, 109].
6. Sampled grating and the Vernier effect. We have demonstrated sampled gratings, as well as the Vernier effect using two slightly-mismatched sampled gratings, for the first time on the silicon photonics platform. They can be used in tunable lasers to achieve a wide tuning range.
 7. Narrow-band uniform Bragg gratings in rib waveguides. We have studied sidewall corrugations either on the rib or on the slab. Experimental results show that for the same corrugation width, the corrugation-on-slab configuration results in a smaller κ than the corrugation-on-rib configuration. The smallest κ we have obtained is about $1 \times 10^3 \text{ m}^{-1}$, corresponding to a bandwidth of about 0.2 nm.
 8. Multi-period gratings. We have demonstrated a multi-period grating concept, by taking advantage of the multiple sidewalls of the rib waveguide. The sidewalls of the rib and the slab are corrugated using different periods, resulting in two or more Bragg wavelengths that are controlled separately. This approach not only increases the design flexibility for custom optical filters but also reduces the device size and fabrication errors.
 9. Thermal sensitivity. We have studied the thermal sensitivities of strip and rib waveguide Bragg gratings, both showing that the Bragg wavelength increases with temperature by about 84 pm/ $^\circ\text{C}$.

10. Wafer-scale performance. We have studied the wafer-scale nonuniformity of strip and rib waveguide gratings. The general conclusion is that rib waveguide gratings have better uniformity than strip waveguide gratings. Another finding is that the Bragg wavelength variation of rib waveguide gratings is primarily caused by the Si thickness variations. Hence improving the SOI thickness uniformity is very important.
11. Spiral gratings. We have demonstrated compact first-order Bragg gratings using a spiral rib waveguide. Our results show not only a significantly improved packing efficiency of about 21.8, but also a very narrow 3-dB bandwidth of 0.26 nm.
12. Slot waveguide Bragg gratings.
 - (a) We have demonstrated both uniform and phase-shifted gratings in slot waveguides. The gratings are formed with periodic sidewall corrugations either on the inside or the outside of the slot waveguide. Experimental results show bandwidths ranging from 2 nm to more than 20 nm for uniform gratings, and Q factors up to 3×10^4 for phase-shifted gratings.
 - (b) Application in biosensing. We have demonstrated a novel biosensor using a slot waveguide phase-shifted grating. Experimental results show a sensitivity of about 340 nm/RIU and a Q factor of 1.5×10^4 , enabling an intrinsic LOD of about 3×10^{-4} RIU (lowest intrinsic LOD for slot-based biosensors). We have also demonstrated the device's ability to interrogate specific biomolecular interactions.

5.2 Future Work

- Apodized grating. As we have seen, uniform gratings often have large side-lobes in their reflection spectra. To reduce the level of the side-lobes, apodization should be used, i.e., varying the amplitude of the index modulation along the length of the grating. Fortunately, apodization is a mature technique that has been widely used for fiber Bragg gratings and there are various apodization profiles [82, 150]. However, we should point out that to characterize

the reflection of apodized gratings, the Y-branch we used in this thesis is not appropriate because it has weak parasitic back-reflection due to the abrupt waveguide discontinuity, which limits the noise floor of the reflection spectrum. To solve this problem, directional couplers or adiabatic couplers could possibly be used [151].

- TM gratings. In this thesis, we have only focused on Bragg gratings operating at TE polarization. Alternatively, we could design Bragg gratings at TM polarization, which has a few advantages. First, the TM mode has very low intensities around the waveguide sidewalls, therefore, the propagation loss is lower than that of the TE mode. This also allows for smaller coupling coefficients and is useful for narrow-band gratings. Moreover, the effective index of the TM mode is much smaller than that of the TE mode, which means that the grating period has to be increased (by a factor of about 1.5) and thus reducing the fabrication challenge.
- Active grating devices. Since the grating devices are sensitive to dimensional variations, it is necessary to develop tunable grating devices with accurate control, e.g., using thermal heating or p-i-n structures. It is also interesting to design high-speed modulators using p-n junctions, as illustrated in Figure 5.1.
- More applications. In this thesis, we have demonstrated a number of applications, however, we think that they represent just the tip of the iceberg. We expect that silicon photonic Bragg gratings will find more applications in silicon lasers [50], WDM systems, biosensors, microwave photonics, and optical signal processing.
- Last but not the least, real products! There are still many challenges that must be overcome before large-scale production can occur. Nonetheless, we expect that the silicon photonics community will keep making progress towards the commercialization of silicon photonic chips. Specifically for silicon photonic Bragg gratings, considerable effort will need to be given to improving the fabrication process, e.g., using immersion lithography, better wafer uniformity, and yield control.

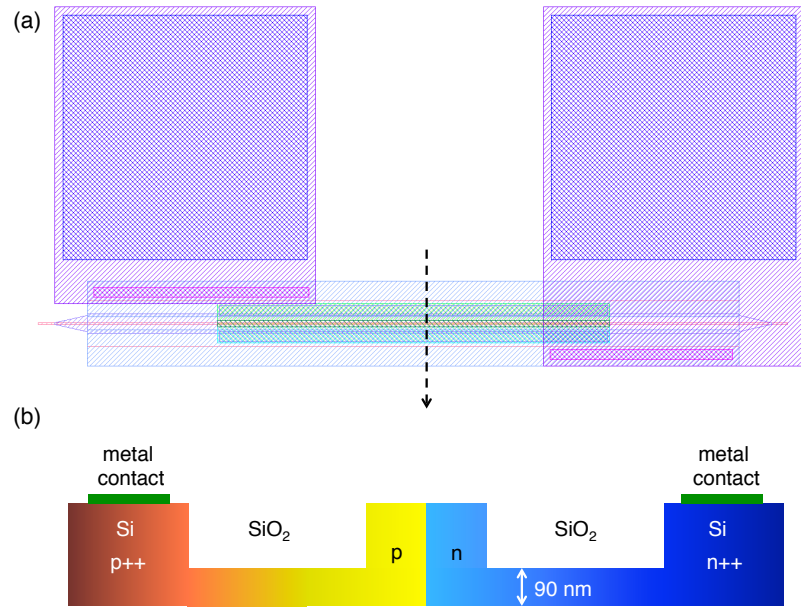


Figure 5.1: A proposed active grating device – high-speed modulator based on a p-n junction: (a) mask layout and (b) schematic of the cross section of the p-n junction.

Bibliography

- [1] Agilent Technologies, *Agilent 81600B Tunable Laser Source Family* (2013). → pages xi, 34
- [2] M. Lipson, “Guiding, modulating, and emitting light on silicon – challenges and opportunities,” *J. Lightwave Technol.* **23**, 4222–4238 (2005). → pages 1
- [3] B. Jalali and S. Fathpour, “Silicon photonics,” *J. Lightwave Technol.* **24**, 4600–4615 (2006). → pages 2
- [4] R. Soref, “The past, present, and future of silicon photonics,” *IEEE J. Sel. Top. Quantum Electron.* **12**, 1678–1687 (2006). → pages 1
- [5] D. Liang and J. E. Bowers, “Recent progress in lasers on silicon,” *Nature Photon.* **4**, 511–517 (2010). → pages 2, 4, 5
- [6] J. Sun, E. Timurdogan, A. Yaacobi, E. S. Hosseini, and M. R. Watts, “Large-scale nanophotonic phased array,” *Nature* **493**, 195–199 (2013). → pages 3
- [7] M. Hochberg and T. Baehr-Jones, “Towards fabless silicon photonics,” *Nature Photon.* **4**, 492–494 (2010). → pages 3, 8
- [8] <http://www.epixfab.eu>, (Retrieved on Nov. 22, 2013). → pages 3, 5, 14, 19, 93
- [9] <http://www.opsisfoundry.org>, (Retrieved on Nov. 22, 2013). → pages 3, 5, 19
- [10] T.-Y. Liow, K.-W. Ang, Q. Fang, J.-F. Song, Y.-Z. Xiong, M.-B. Yu, G.-Q. Lo, and D.-L. Kwong, “Silicon modulators and germanium photodetectors on SOI: Monolithic integration, compatibility, and performance optimization,” *IEEE J. Sel. Top. Quantum Electron.* **16**, 307–315 (2010). → pages 3

- [11] T.-Y. Liow, J. Song, X. Tu, A.-J. Lim, Q. Fang, N. Duan, M. Yu, and G.-Q. Lo, “Silicon optical interconnect device technologies for 40 Gb/s and beyond,” *IEEE J. Sel. Top. Quantum Electron.* **19**, 8200312 (2013). → pages 3
- [12] D. A. B. Miller, “Device requirements for optical interconnects to silicon chips,” *Proc. IEEE* **97**, 1166–1185 (2009). → pages 4
- [13] G. T. Reed, G. Mashanovich, F. Y. Gardes, and D. J. Thomson, “Silicon optical modulators,” *Nature Photon.* **4**, 518–526 (2010). → pages 4, 6
- [14] L. Chrostowski, S. Grist, J. Flueckiger, W. Shi, X. Wang, E. Ouellet, H. Yun, M. Webb, B. Nie, Z. Liang, K. C. Cheung, S. A. Schmidt, D. M. Ratner, and N. A. F. Jaeger, “Silicon photonic resonator sensors and devices,” *Proc. SPIE* **8236**, 823620 (2012). → pages 4, 62, 106, 115, 119
- [15] S. Talebi Fard, S. M. Grist, V. Donzella, S. A. Schmidt, J. Flueckiger, X. Wang, W. Shi, A. Millspaugh, M. Webb, D. M. Ratner, K. C. Cheung, and L. Chrostowski, “Label-free silicon photonic biosensors for use in clinical diagnostics,” *Proc. SPIE* **8629**, 862909 (2013). → pages 4, 70, 106
- [16] J. T. Robinson, L. Chen, and M. Lipson, “On-chip gas detection in silicon optical microcavities,” *Opt. Lett.* **16**, 4296–4301 (2008). → pages 4, 5
- [17] J. Roels, I. De Vlaminck, L. Lagae, B. Maes, D. Van Thourhout, and R. Baets, “Tunable optical forces between nanophotonic waveguides,” *Nature Nano.* **4**, 510–513 (2009). → pages 4
- [18] D. Van Thourhout and J. Roels, “Optomechanical device actuation through the optical gradient force,” *Nature Photon.* **4**, 211–217 (2010). → pages 4
- [19] J. Mower and D. Englund, “Efficient generation of single and entangled photons on a silicon photonic integrated chip,” *Phys. Rev. A* **84**, 052326 (2011). → pages 4
- [20] D. Bonneau, E. Engin, K. Ohira, N. Suzuki, H. Yoshida, N. Iizuka, M. Ezaki, C. M. Natarajan, M. G. Tanner, R. H. Hadfield, S. N. Dorenbos, V. Zwillaer, J. L. O’Brien, and M. G. Thompson, “Quantum interference and manipulation of entanglement in silicon wire waveguide quantum circuits,” *New J. Phys.* **14**, 045003 (2012). → pages
- [21] N. Matsuda, H. Le Jeannic, H. Fukuda, T. Tsuchizawa, W. J. Munro, K. Shimizu, K. Yamada, Y. Tokura, and H. Takesue, “A monolithically in-

tegrated polarization entangled photon pair source on a silicon chip,” Sci. Rep. **2** (2012). → pages

- [22] J. O’Brien, B. Patton, M. Sasaki, and J. Vučković, “Focus on integrated quantum optics,” New J. Phys. **15**, 035016 (2013). → pages 4
- [23] J. Leuthold, C. Koos, and W. Freude, “Nonlinear silicon photonics,” Nature Photon. **4**, 535–544 (2010). → pages 4
- [24] R. Soref, “Mid-infrared photonics in silicon and germanium,” Nature Photon. **4**, 495–497 (2010). → pages 4
- [25] D. Marpaung, C. Roeloffzen, R. Heideman, A. Leinse, S. Sales, and J. Capmany, “Integrated microwave photonics,” Laser & Photonics Reviews **7**, 506–538 (2013). → pages 4
- [26] M. Ko, J.-S. Youn, M.-J. Lee, K.-C. Choi, H. Rucker, and W.-Y. Choi, “Silicon photonics-wireless interface IC for 60-GHz wireless link,” IEEE Photon. Technol. Lett. **24**, 1112–1114 (2012). → pages
- [27] M. Burla, L. R. Cortés, M. Li, X. Wang, L. Chrostowski, and J. A. na, “Integrated waveguide Bragg gratings for microwave photonics signal processing,” Opt. Express **21**, 25120–25147 (2013). → pages 4, 70, 131
- [28] <http://teraxion.com/en/crx-sff>, (Retrieved on Nov. 22, 2013). → pages 4, 7
- [29] C. Xia, L. Chao, and T. H. K., “Device engineering for silicon photonics,” NPG Asia Mater. **3**, 34–40 (2011). → pages 4
- [30] J. Michel, J. Liu, and L. C. Kimerling, “High-performance Ge-on-Si photodetectors,” Nature Photon. **4**, 527–534 (2010). → pages 4
- [31] W. Bogaerts, R. Baets, P. Dumon, V. Wiaux, S. Beckx, D. Taillaert, B. Luysaert, J. V. Campenhout, P. Bienstman, and D. V. Thourhout, “Nanophotonic waveguides in silicon-on-insulator fabricated with CMOS technology,” J. Lightwave Technol. **23**, 401–412 (2005). → pages 4, 14
- [32] W. Bogaerts, S. Selvaraja, P. Dumon, J. Brouckaert, K. De Vos, D. Van Thourhout, and R. Baets, “Silicon-on-insulator spectral filters fabricated with CMOS technology,” IEEE J. Sel. Top. Quantum Electron. **16**, 33–44 (2010). → pages 4, 20
- [33] R. A. Soref, J. Schmidtchen, and K. Petermann, “Large single-mode rib waveguides in GeSi-Si and Si-on-SiO₂,” IEEE J. Quantum Electron. **27**, 1971–1974 (1991). → pages 4, 79

- [34] P. Dong, W. Qian, S. Liao, H. Liang, C.-C. Kung, N.-N. Feng, R. Shafiiha, J. Fong, D. Feng, A. V. Krishnamoorthy, and M. Asghari, “Low loss shallow-ridge silicon waveguides,” *Opt. Express* **18**, 14474–14479 (2010). → pages 5, 81
- [35] W. Bogaerts and S. K. Selvaraja, “Compact single-mode silicon hybrid rib/strip waveguide with adiabatic bends,” *IEEE Photon. J.* **3**, 422–432 (2011). → pages 5
- [36] V. R. Almeida, Q. Xu, C. A. Barrios, and M. Lipson, “Guiding and confining light in void nanostructure,” *Opt. Lett.* **29**, 1209–1211 (2004). → pages 5, 107, 119
- [37] R. Ding, T. Baehr-Jones, W.-J. Kim, A. Spott, M. Fournier, J.-M. Fedeli, S. Huang, J. Luo, A. K.-Y. Jen, L. Dalton, and M. Hochberg, “Sub-volt silicon-organic electro-optic modulator with 500 MHz bandwidth,” *J. Light-wave Technol.* **29**, 1112–1117 (2011). → pages 5
- [38] C. Koos, P. Vorreau, T. Vallaitis, P. Dumon, W. Bogaerts, R. Baets, B. Esem-besson, I. Biaggio, T. Michinobu, F. Diederich, W. Freude, and J. Leuthold, “All-optical high-speed signal processing with silicon-organic hybrid slot waveguides,” *Nature Photon.* **3**, 216–219 (2009). → pages 5
- [39] Y. Liu, T. Baehr-Jones, J. Li, A. Pomerene, and M. Hochberg, “Efficient strip to strip-loaded slot mode converter in silicon-on-insulator,” *IEEE Photon. Technol. Lett.* **23**, 1496–1498 (2011). → pages 5
- [40] R. Won, “Integrating silicon photonics,” *Nature Photon.* **4**, 498–499 (2010). → pages 5
- [41] C. Kopp, S. Bernabé, B. Bakir, J.-M. Fedeli, R. Orobctchouk, F. Schrank, H. Porte, L. Zimmermann, and T. Tekin, “Silicon photonic circuits: On-CMOS integration, fiber optical coupling, and packaging,” *IEEE J. Sel. Top. Quantum Electron.* **17**, 498–509 (2011). → pages 5
- [42] G. Roelkens, D. Vermeulen, S. Selvaraja, R. Halir, W. Bogaerts, and D. Van Thourhout, “Grating-based optical fiber interfaces for silicon-on-insulator photonic integrated circuits,” *IEEE J. Sel. Top. Quantum Electron.* **17**, 571–580 (2011). → pages 5, 23
- [43] A. Mekis, S. Gloeckner, G. Masini, A. Narasimha, T. Pinguet, S. Sahni, and P. De Dobbelaere, “A grating-coupler-enabled CMOS photonics platform,” *IEEE J. Sel. Top. Quantum Electron.* **17**, 597–608 (2011). → pages 23

- [44] L. He, Y. Liu, C. Galland, A.-J. Lim, G.-Q. Lo, T. Baehr-Jones, and M. Hochberg, “A high-efficiency nonuniform grating coupler realized with 248-nm optical lithography,” *IEEE Photon. Technol. Lett.* **25**, 1358–1361 (2013). → pages 5
- [45] H. Rong, R. Jones, A. Liu, O. Cohen, D. Hak, A. Fang, and M. Paniccia, “A continuous-wave Raman silicon laser,” *Nature* **433**, 725–728 (2005). → pages 5
- [46] J. Liu, X. Sun, R. Camacho-Aguilera, L. C. Kimerling, and J. Michel, “Ge-on-Si laser operating at room temperature,” *Opt. Lett.* **35**, 679–681 (2010). → pages 5
- [47] M. J. R. Heck, H.-W. Chen, A. W. Fang, B. R. Koch, D. Liang, H. Park, M. N. Sysak, and J. E. Bowers, “Hybrid silicon photonics for optical interconnects,” *IEEE J. Sel. Top. Quantum Electron.* **17**, 333–346 (2011). → pages 5
- [48] A. W. Fang, H. Park, O. Cohen, R. Jones, M. J. Paniccia, and J. E. Bowers, “Electrically pumped hybrid AlGaInAs-silicon evanescent laser,” *Opt. Express* **14**, 9203–9210 (2006). → pages 5
- [49] A. W. Fang, E. Lively, Y.-H. Kuo, D. Liang, and J. E. Bowers, “A distributed feedback silicon evanescent laser,” *Opt. Express* **16**, 4413–4419 (2008). → pages 6
- [50] A. W. Fang, B. R. Koch, R. Jones, E. Lively, D. Liang, Y.-H. Kuo, and J. E. Bowers, “A distributed Bragg reflector silicon evanescent laser,” *IEEE Photon. Technol. Lett.* **20**, 1667–1669 (2008). → pages 6, 133
- [51] M. N. Sysak, J. O. Anthes, D. Liang, J. E. Bowers, O. Raday, and R. Jones, “A hybrid silicon sampled grating DBR tunable laser,” in *IEEE Conference on Group IV Photonics (GFP)*, Cardiff, UK pp. 55–57 (2008). → pages 6
- [52] D. Liang, M. Fiorentino, T. Okumura, H.-H. Chang, D. T. Spencer, Y.-H. Kuo, A. W. Fang, D. Dai, R. G. Beausoleil, and J. E. Bowers, “Electrically-pumped compact hybrid silicon microring lasers for optical interconnects,” *Opt. Express* **17**, 20355–20364 (2009). → pages 6
- [53] J. V. Campenhout, L. Liu, P. R. Romeo, D. V. Thourhout, C. Seassal, P. Regreny, L. D. Cioccio, J.-M. Fedeli, and R. Baets, “A compact SOI-integrated multiwavelength laser source based on cascaded InP microdisks,” *IEEE Photon. Technol. Lett.* **20**, 1345–1347 (2008). → pages 6

- [54] R. A. Soref and B. R. Bennett, “Electrooptical effects in silicon,” IEEE J. Quantum Electron. **23**, 123–129 (1987). → pages 6
- [55] L. Liao, D. Samara-Rubio, M. Morse, A. Liu, D. Hodge, D. Rubin, U. D. Keil, and T. Franck, “High speed silicon Mach-Zehnder modulator,” Opt. Express **13**, 3129–3135 (2005). → pages 6
- [56] Q. Xu, B. Schmidt, S. Pradhan, and M. Lipson, “Micrometre-scale silicon electro-optic modulator,” Nature **435**, 325–327 (2005). → pages 6
- [57] L. Liao, A. Liu, D. Rubin, J. Basak, Y. Chetrit, H. Nguyen, R. Cohen, N. Izhaky, and M. Paniccia, “40 Gbit/s silicon optical modulator for high-speed applications,” Electron. Lett. **43**, 1196–1197 (2007). → pages 6
- [58] M. Lipson, “Compact electro-optic modulators on a silicon chip,” IEEE J. Sel. Top. Quantum Electron. **12**, 1520–1526 (2006). → pages 6
- [59] F. Gardes, A. Brimont, P. Sanchis, G. Rasigade, D. Marris-Morini, L. O’Faolain, F. Dong, J. Fedeli, P. Dumon, L. Vivien, T. Krauss, G. Reed, and J. Marti, “High-speed modulation of a compact silicon ring resonator based on a reverse-biased *pn* diode,” Opt. Express **17**, 21986–21991 (2009). → pages 7
- [60] P. Dong, S. Liao, D. Feng, H. Liang, D. Zheng, R. Shafiiha, C.-C. Kung, W. Qian, G. Li, X. Zheng, A. V. Krishnamoorthy, and M. Asghari, “Low V_{pp} , ultralow-energy, compact, high-speed silicon electro-optic modulator,” Opt. Express **17**, 22484–22490 (2009). → pages 7
- [61] S. Liao, N.-N. Feng, D. Feng, P. Dong, R. Shafiiha, C.-C. Kung, H. Liang, W. Qian, Y. Liu, J. Fong, J. E. Cunningham, Y. Luo, and M. Asghari, “36 GHz submicron silicon waveguide germanium photodetector,” Opt. Express **19**, 10967–10972 (2011). → pages 7
- [62] M. Hochberg, N. Harris, R. Ding, Y. Zhang, A. Novack, Z. Xuan, and T. Baehr-Jones, “Silicon photonics: the next fabless semiconductor industry,” IEEE Solid-State Circuits Magazine **5**, 48–58 (2013). → pages 7
- [63] A. Liu, L. Liao, Y. Chetrit, J. Basak, H. Nguyen, D. Rubin, and M. Paniccia, “Wavelength division multiplexing based photonic integrated circuits on silicon-on-insulator platform,” IEEE J. Sel. Top. Quantum Electron. **16**, 23–32 (2010). → pages 7

- [64] S. Koehl, A. Liu, and M. Paniccia, “Integrated silicon photonics: Harnessing the data explosion,” *Optics & Photonics News* **22**, 24–29 (2011). → pages 7
- [65] <http://www.luxtera.com/>, (Retrieved on Nov. 22, 2013). → pages 7
- [66] <http://genalyte.com/technology-overview/>, (Retrieved on Nov. 22, 2013). → pages 7
- [67] J. Buus, M.-C. Amann, and D. J. Blumenthal, *Tunable Laser Diodes and Related Optical Sources, 2nd Ed.* (John Wiley & Sons, Inc., 2005). → pages 9, 10, 12, 58
- [68] T. E. Murphy, J. T. Hastings, and H. I. Smith, “Fabrication and characterization of narrow-band Bragg-reflection filters in silicon-on-insulator ridge waveguides,” *J. Lightwave Technol.* **19**, 1938–1942 (2001). → pages 12, 13, 79, 80
- [69] L. Liao, A. Liu, S. Pang, and M. J. Paniccia, “Tunable Bragg grating filters in SOI waveguides,” in *Optical Amplifiers and Their Applications/Integrated Photonics Research*, paper IThE2 (2004). → pages 12
- [70] S. Homampour, M. P. Bulk, P. E. Jessop, and A. P. Knights, “Thermal tuning of planar Bragg gratings in silicon-on-insulator rib waveguides,” *Physica Status Solidi (C)* **6**, S240–S243 (2009). → pages 12
- [71] R. Loiacono, G. T. Reed, G. Z. Mashanovich, R. Gwilliam, S. J. Henley, Y. Hu, R. Feldesh, and R. Jones, “Laser erasable implanted gratings for integrated silicon photonics,” *Opt. Express* **19**, 10728–10734 (2011). → pages 12
- [72] Q. Fang, J. F. Song, X. Tu, L. Jia, X. Luo, M. Yu, and G. Q. Lo, “Carrier-induced silicon Bragg grating filters with a p-i-n junction,” *IEEE Photon. Technol. Lett.* **25**, 810–812 (2013). → pages 13
- [73] J. T. Hastings, M. H. Lim, J. G. Goodberlet, and H. I. Smith, “Optical waveguides with apodized sidewall gratings via spatial-phase-locked electron-beam lithography,” *J. Vac. Sci. Technol. B* **20**, 2753–2757 (2002). → pages 13, 79, 80
- [74] I. Giuntini, A. Gajda, M. Krause, R. Steingrüber, J. Bruns, and K. Petermann, “Tunable Bragg reflectors on silicon-on-insulator rib waveguides,” *Opt. Express* **17**, 18518–18524 (2009). → pages 79, 80

- [75] I. Giuntoni, D. Stolarek, H. Richter, S. Marschmeyer, J. Bauer, A. Gajda, J. Bruns, B. Tillack, K. Petermann, and L. Zimmermann, “Deep-UV technology for the fabrication of Bragg gratings on SOI rib waveguides,” *IEEE Photon. Technol. Lett.* **21**, 1894–1896 (2009). → pages 13
- [76] D. T. H. Tan, K. Ikeda, R. E. Saperstein, B. Slutsky, and Y. Fainman, “Chip-scale dispersion engineering using chirped vertical gratings,” *Opt. Lett.* **33**, 3013–3015 (2008). → pages 13
- [77] A. S. Jugessur, J. Dou, J. S. Aitchison, R. M. De La Rue, and M. Gnan, “A photonic nano-Bragg grating device integrated with microfluidic channels for bio-sensing applications,” *Microelectron. Eng.* **86**, 1488–1490 (2009). → pages 13, 106, 119
- [78] D. T. H. Tan, K. Ikeda, and Y. Fainman, “Cladding-modulated Bragg gratings in silicon waveguides,” *Opt. Lett.* **34**, 1357–1359 (2009). → pages 13
- [79] D. T. H. Tan, K. Ikeda, and Y. Fainman, “Coupled chirped vertical gratings for on-chip group velocity dispersion engineering,” *Appl. Phys. Lett.* **95**, 141109 (2009). → pages 13
- [80] D. T. H. Tan, K. Ikeda, S. Zamek, A. Mizrahi, M. P. Nezhad, A. V. Krishnamoorthy, K. Raj, J. E. Cunningham, X. Zheng, I. Shubin, Y. Luo, and Y. Fainman, “Wide bandwidth, low loss 1 by 4 wavelength division multiplexer on silicon for optical interconnects,” *Opt. Express* **19**, 2401–2409 (2011). → pages 13
- [81] A. Simard, N. Belhadj, Y. Painchaud, and S. LaRochelle, “Apodized silicon-on-insulator Bragg gratings,” *IEEE Photon. Technol. Lett.* **24**, 1033–1035 (2012). → pages 13
- [82] T. Erdogan, “Fiber grating spectra,” *J. Lightwave Technol.* **15**, 1277–1294 (1997). → pages 13, 132
- [83] <http://www.mint.ca/>, (Retrieved on Nov. 22, 2013). → pages 14
- [84] <http://www.lumerical.com>, (Retrieved on Nov. 22, 2013). → pages 17, 47
- [85] P. Dumon, “Ultra-compact integrated optical filters in silicon-on-insulator by means of wafer-scale technology,” Ph.D. thesis, Ghent University (2007). → pages 18
- [86] L. Chrostowski, *Silicon Photonics Design* (Lukas Chrostowski, 2013). → pages 20

- [87] <http://www.klayout.de>, (Retrieved on Nov. 22, 2013). → pages 22
- [88] <http://www.designw.com/>, (Retrieved on Nov. 22, 2013). → pages 22
- [89] <http://www.mentor.com/>, (Retrieved on Nov. 22, 2013). → pages 22, 47, 50
- [90] Y. Wang, “Grating coupler design based on silicon-on-insulator,” Master’s thesis, University of British Columbia (2013). → pages 23, 32
- [91] C. Lin, “Photonic device design flow: from mask layout to device measurement,” Master’s thesis, University of British Columbia (2012). → pages 25
- [92] H. Yun, “Design and characterization of a dumbbell micro-ring resonator reflector,” Master’s thesis, University of British Columbia (2013). → pages 25
- [93] <http://siepic.ubc.ca/probestation>, (Retrieved on Nov. 22, 2013). → pages 28
- [94] E. Leckel, J. Sang, E. U. Wagemann, and E. Mueller, “Impact of source spontaneous emission (SSE) on the measurement of DWDM components,” in *Optical Fiber Communication Conference*, paper WB4 (2000). → pages 32
- [95] X. Wang, W. Shi, M. Hochberg, K. Adam, E. Schelew, J. F. Young, N. A. F. Jaeger, and L. Chrostowski, “Lithography simulation for the fabrication of silicon photonic devices with deep-ultraviolet lithography,” in *IEEE Conference on Group IV Photonics (GFP)*, San Diego, CA, 2012, paper ThP 17 (2012). → pages 45
- [96] S. K. Selvaraja, P. Jaenen, W. Bogaerts, D. VanThourhout, P. Dumon, and R. Baets, “Fabrication of photonic wire and crystal circuits in silicon-on-insulator using 193-nm optical lithography,” *J. Lightwave Technol.* **27**, 4076–4083 (2009). → pages 46, 47, 50, 53
- [97] W. Bogaerts, P. Bratt, L. Vanholme, P. Bienstman, and R. Baets, “Closed-loop modeling of silicon nanophotonics from design to fabrication and back again,” *Optical and Quantum Electronics* **40**, 801–811 (2008). → pages 47
- [98] K. Adam, Y. Granik, A. Torres, and N. B. Cobb, “Improved modeling performance with an adapted vectorial formulation of the Hopkins imaging equation,” in *Optical Microlithography XVI* pp. 78–91 (2003). → pages 50
- [99] G. Cocorullo and I. Rendina, “Thermo-optical modulation at 1.5 μm in silicon etalon,” *Electron. Lett.* **28**, 83–85 (1992). → pages 52

- [100] S. Selvaraja, W. Bogaerts, P. Dumon, D. Van Thourhout, and R. Baets, “Sub-nanometer linewidth uniformity in silicon nanophotonic waveguide devices using CMOS fabrication technology,” *IEEE J. Sel. Top. Quantum Electron.* **16**, 316–324 (2010). → pages 52, 53
- [101] A. H. Atabaki, A. A. Eftekhar, M. Askari, and A. Adibi, “Accurate post-fabrication trimming of ultra-compact resonators on silicon,” *Opt. Express* **21**, 14139–14145 (2013). → pages 53
- [102] W. A. Zortman, D. C. Trotter, and M. R. Watts, “Silicon photonics manufacturing,” *Opt. Express* **18**, 23598–23607 (2010). → pages 53
- [103] A. Yariv and P. Yeh, *Photonics: Optical Electronics in Modern Communications, Sixth Edition* (Oxford University Press, 2007). → pages 58, 64, 65
- [104] S. Srinivasan, A. W. Fang, D. Liang, J. Peters, B. Kaye, and J. E. Bowers, “Design of phase-shifted hybrid silicon distributed feedback lasers,” *Opt. Express* **19**, 9255–9261 (2011). → pages 59
- [105] P. Prabhathan, V. M. Murukeshan, Z. Jing, and P. V. Ramana, “Compact SOI nanowire refractive index sensor using phase shifted Bragg grating,” *Opt. Express* **17**, 15330–15341 (2009). → pages 61, 70
- [106] P. Barclay, K. Srinivasan, and O. Painter, “Nonlinear response of silicon photonic crystal microresonators excited via an integrated waveguide and fiber taper,” *Opt. Express* **13**, 801–820 (2005). → pages 68
- [107] X. Sun, X. Zhang, C. Schuck, and H. X. Tang, “Nonlinear optical effects of ultrahigh-Q silicon photonic nanocavities immersed in superfluid helium,” *Sci. Rep.* **3** (2013). → pages 68, 69
- [108] M. Burla, L. Romero Cortes, M. Li, X. Wang, L. Chrostowski, and J. Azana, “On-chip ultra-wideband microwave photonic phase shifter and true time delay line based on a single phase-shifted waveguide Bragg grating,” in *IEEE Microwave Photon. Conf.* pp. W2–3 (2013). → pages 70, 131
- [109] M. Burla, M. Li, L. Romero Cortes, X. Wang, L. Chrostowski, and J. Azana, “2.5 THz bandwidth on-chip photonic fractional Hilbert transformer based on a phase-shifted waveguide Bragg grating,” in *IEEE Photon. Conf.* pp. 436–437 (2013). → pages 70, 131
- [110] A. Yariv and P. Yeh, *Optical Waves in Crystal* (New York: Wiley, 1984). → pages 73

- [111] V. Jayaraman, Z.-M. Chuang, and L. A. Coldren, “Theory, design, and performance of extended tuning range semiconductor lasers with sampled gratings,” *IEEE J. Quantum Electron.* **29**, 1824–1834 (1993). → pages 73, 75
- [112] S. Honda, Z. Wu, J. Matsui, K. Utaka, T. Edura, M. Tokuda, K. Tsutsui, and Y. Wada, “Largely-tunable wideband Bragg gratings fabricated on SOI rib waveguides employed by deep-RIE,” *Electron. Lett.* **43**, 630–631 (2007). → pages 79
- [113] X. Wang, W. Shi, H. Yun, S. Grist, N. A. F. Jaeger, and L. Chrostowski, “Narrow-band waveguide Bragg gratings on SOI wafers with CMOS-compatible fabrication process,” *Opt. Express* **20**, 15547–15558 (2012). → pages 79
- [114] G. Jiang, R. Chen, Q. Zhou, J. Yang, M. Wang, and X. Jiang, “Slab-modulated sidewall Bragg gratings in silicon-on-insulator ridge waveguides,” *IEEE Photon. Technol. Lett.* **23**, 6–9 (2011). → pages 80
- [115] S. Zamek, D. T. H. Tan, M. Khajavikhan, M. Ayache, M. P. Nezhad, and Y. Fainman, “Compact chip-scale filter based on curved waveguide Bragg gratings,” *Opt. Lett.* **35**, 3477–3479 (2010). → pages 99, 104
- [116] A. D. Simard, Y. Painchaud, and S. LaRochelle, “Integrated Bragg gratings in spiral waveguides,” *Opt. Express* **21**, 8953–8963 (2013). → pages 99, 100, 104
- [117] X. Wang, H. Yun, and L. Chrostowski, “Integrated Bragg gratings in spiral waveguides,” in *Conference on Lasers and Electro-Optics*, San Jose, CA, paper CTh4F.8 (2013). → pages 99
- [118] J. Blasco and C. Barrios, “Compact slot-waveguide/channel-waveguide mode-converter,” in *Conference on Lasers and Electro-Optics Europe (CLEO/Europe)* p. 607 (2005). → pages 110
- [119] A. Saynatjoki, L. Karvonen, T. Alasaarela, X. Tu, T. Y. Liow, M. Hiltunen, A. Tervonen, G. Q. Lo, and S. Honkanen, “Low-loss silicon slot waveguides and couplers fabricated with optical lithography and atomic layer deposition,” *Opt. Express* **19**, 26275–26282 (2011). → pages 115, 118
- [120] R. Palmer, L. Alloatti, D. Korn, W. Heni, P. Schindler, J. Bolten, M. Karl, M. Waldow, T. Wahlbrink, W. Freude, C. Koos, and J. Leuthold, “Low-loss silicon strip-to-slot mode converters,” *IEEE Photon. J.* **5**, 2200409 (2013). → pages 110

- [121] T. Baehr-Jones, M. Hochberg, C. Walker, and A. Scherer, “High-Q optical resonators in silicon-on-insulator-based slot waveguides,” *Appl. Phys. Lett.* **86**, 081101 (2005). → pages 115, 120
- [122] H. Zhang, J. Zhang, S. Chen, J. Song, J. Kee, M. Yu, and G.-Q. Lo, “CMOS-compatible fabrication of silicon-based sub-100-nm slot waveguide with efficient channel-slot coupler,” *IEEE Photon. Technol. Lett.* **24**, 10–12 (2012). → pages 115
- [123] R. Ding, T. Baehr-Jones, W.-J. Kim, X. Xiong, R. Bojko, J.-M. Fedeli, M. Fournier, and M. Hochberg, “Low-loss strip-loaded slot waveguides in silicon-on-insulator,” *Opt. Express* **18**, 25061–25067 (2010). → pages 118
- [124] A. Spott, T. Baehr-Jones, R. Ding, Y. Liu, R. Bojko, T. O’Malley, A. Pomerene, C. Hill, W. Reinhardt, and M. Hochberg, “Photolithographically fabricated low-loss asymmetric silicon slot waveguides,” *Opt. Express* **19**, 10950–10958 (2011). → pages 118
- [125] H. K. Hunt and A. M. Armani, “Label-free biological and chemical sensors,” *Nanoscale* **2**, 1544–1559 (2010). → pages 119
- [126] X. Fan, I. M. White, S. I. Shopova, H. Zhu, J. D. Suter, and Y. Sun, “Sensitive optical biosensors for unlabeled targets: A review,” *Anal. Chim. Acta* **620**, 8–26 (2008). → pages 119
- [127] M. S. Luchansky and R. C. Bailey, “High-Q optical sensors for chemical and biological analysis,” *Anal. Chem.* **84**, 793–821 (2012). → pages 119
- [128] K. D. Vos, I. Bartolozzi, E. Schacht, P. Bienstman, and R. Baets, “Silicon-on-insulator microring resonator for sensitive and label-free biosensing,” *Opt. Express* **15**, 7610–7615 (2007). → pages 119
- [129] A. L. Washburn, L. C. Gunn, and R. C. Bailey, “Label-free quantitation of a cancer biomarker in complex media using silicon photonic microring resonators,” *Anal. Chem.* **81**, 9499–9506 (2009). PMID: 19848413. → pages
- [130] M. Iqbal, M. A. Gleeson, B. Spaugh, F. Tybor, W. G. Gunn, M. Hochberg, T. Baehr-Jones, R. C. Bailey, and L. C. Gunn, “Label-free biosensor arrays based on silicon ring resonators and high-speed optical scanning instrumentation,” *IEEE J. Quantum Electron.* **16**, 654–661 (2010). → pages
- [131] M. S. Luchansky and R. C. Bailey, “Silicon photonic microring resonators for quantitative cytokine detection and T-cell secretion analysis,” *Anal. Chem.* **82**, 1975–1981 (2010). PMID: 20143780. → pages

- [132] J. Flueckiger, S. M. Grist, G. Bisra, L. Chrostowski, and K. C. Cheung, “Cascaded silicon-on-insulator microring resonators for the detection of biomolecules in PDMS microfluidic channels,” Proc. SPIE **7929**, 79290I (2011). → pages 119
- [133] S. M. Grist, S. A. Schmidt, J. Flueckiger, V. Donzella, W. Shi, S. T. Fard, J. T. Kirk, D. M. Ratner, K. C. Cheung, and L. Chrostowski, “Silicon photonic micro-disk resonators for label-free biosensing,” Opt. Express **21**, 7994–8006 (2013). → pages 119
- [134] A. S. Jugessur, M. Yagnyukova, J. Dou, and J. S. Aitchison, “Bragg-grating air-slot optical waveguide for label-free sensing,” Proc. SPIE **8231**, 82310N (2012). → pages 119
- [135] S. Mandal and D. Erickson, “Nanoscale optofluidic sensor arrays,” Opt. Express **16**, 1623–1631 (2008). → pages 119
- [136] C. A. Barrios, K. B. Gylfason, B. Sánchez, A. Griol, H. Sohlström, M. Holgado, and R. Casquel, “Slot-waveguide biochemical sensor,” Opt. Lett. **32**, 3080–3082 (2007). → pages 119, 120, 123
- [137] T. Claes, J. Molera, K. De Vos, E. Schacht, R. Baets, and P. Bienstman, “Label-free biosensing with a slot-waveguide-based ring resonator in silicon on insulator,” IEEE Photon. J. **1**, 197–204 (2009). → pages 119, 120, 123, 127
- [138] B. Wang, M. A. Dundar, R. Notzel, F. Karouta, S. He, and R. W. van der Heijden, “Photonic crystal slot nanobeam slow light waveguides for refractive index sensing,” Appl. Phys. Lett. **97**, 151105 (2010). → pages 120, 123
- [139] M. Scullion, A. D. Falco, and T. Krauss, “Slotted photonic crystal cavities with integrated microfluidics for biosensing applications,” Biosens. Bioelectron. **27**, 101–105 (2011). → pages 120
- [140] Y. Xia and G. M. Whitesides, “Soft lithography,” Annu. Rev. Mater. Sci. **28**, 153–184 (1998). → pages 121
- [141] C. A. Barrios, M. J. B. nuls, V. González-Pedro, K. B. Gylfason, B. Sánchez, A. Griol, A. Maquieira, H. Sohlström, M. Holgado, and R. Casquel, “Label-free optical biosensing with slot-waveguides,” Opt. Lett. **33**, 708–710 (2008). → pages 123

- [142] K. B. Gylfason, C. F. Carlborg, A. Kazmierczak, F. Dortu, H. Sohlström, L. Vivien, C. A. Barrios, W. van der Wijngaart, and G. Stemme, “On-chip temperature compensation in an integrated slot-waveguide ring resonator refractive index sensor array,” *Opt. Express* **18**, 3226–3237 (2010). → pages
- [143] C. F. Carlborg, K. B. Gylfason, A. Kazmierczak, F. Dortu, M. J. Banuls Polo, A. Maquieira Catala, G. M. Kresbach, H. Sohlstrom, T. Moh, L. Vivien, J. Popplewell, G. Ronan, C. A. Barrios, G. Stemme, and W. van der Wijngaart, “A packaged optical slot-waveguide ring resonator sensor array for multiplex label-free assays in labs-on-chips,” *Lab Chip* **10**, 281–290 (2010). → pages 123
- [144] W. L. DeLano, M. H. Ultsch, A. M. de, Vos, and J. A. Wells, “Convergent solutions to binding at a protein-protein interface,” *Science* **287**, 1279–1283 (2000). → pages 127
- [145] M. C. Coen, R. Lehmann, P. Gröning, M. Bielmann, C. Galli, and L. Schlapbach, “Adsorption and bioactivity of protein a on silicon surfaces studied by AFM and XPS,” *J. Colloid Interface Sci.* **233**, 180–189 (2001). → pages 127
- [146] J. Vörös, “The density and refractive index of adsorbing protein layers,” *Biophys. J.* **87**, 553–561 (2004). → pages 127
- [147] S. Darst, M. Ahlers, P. Meller, E. Kubalek, R. Blankenburg, H. Ribi, H. Ringsdorf, and R. Kornberg, “Two-dimensional crystals of streptavidin on biotinylated lipid layers and their interactions with biotinylated macromolecules,” *Biophys. J.* **59**, 387–396 (1991). → pages 127
- [148] A. Weisenhorn, F.-J. Schmitt, W. Knoll, and P. Hansma, “Streptavidin binding observed with an atomic force microscope,” *Ultramicroscopy* **42–44**, 1125–1132 (1992). → pages 127
- [149] J. T. Kirk, N. D. Brault, T. Baehr-Jones, M. Hochberg, S. Jiang, and D. M. Ratner, “Zwitterionic polymer-modified silicon microring resonators for label-free biosensing in undiluted humanplasma,” *Biosens. Bioelectron.* **42**, 100–105 (2013). → pages 128
- [150] K. Ennser, M. Zervas, and R. Laming, “Optimization of apodized linearly chirped fiber gratings for optical communications,” *IEEE J. Quantum Electron.* **34**, 770–778 (1998). → pages 132

- [151] J. Xing, K. Xiong, H. Xu, Z. Li, X. Xiao, J. Yu, and Y. Yu, “Silicon-on-insulator-based adiabatic splitter with simultaneous tapering of velocity and coupling,” Opt. Lett. **38**, 2221–2223 (2013). → pages 133

Appendix A

Publications

A.1 Book Chapters

1. X. Wang, W. Shi, and L. Chrostowski, “Silicon photonic Bragg gratings,” in *High-Speed Photonics Interconnects*, L. Chrostowski and K. Iniewski, Ed. CRC Press, 2013, pp. 51-85.
2. X. Wang and L. Chrostowski, “High-speed directly-modulated injection-locked VCSELs,” in *Integrated Microsystems: Electronics, Photonics, and Biotechnology*, K. Iniewski, Ed. CRC Press, 2011, pp. 471-507.

A.2 Journal Publications

1. M. Burla, L. R. Cortes, M. Li, X. Wang, L. Chrostowski, and J. Azana, “Integrated waveguide Bragg gratings for microwave photonics signal processing (Invited Paper),” *Opt. Express*, vo. 21, no. 21, pp. 25120-25147, 2013.
2. X. Wang, S. Grist, J. Flueckiger, N. A. F. Jaeger, and L. Chrostowski, “Silicon photonic slot waveguide Bragg gratings and resonators,” *Opt. Express*, vol. 21, no. 16, pp. 19029-19039, 2013.
3. X. Wang, J. Flueckiger, S. Schmidt, S. Grist, S. T. Fard, J. Kirk, M. Doerfler, K. C. Cheung, D. M. Ratner, and L. Chrostowski, “A silicon photonic

- biosensor using phase-shifted Bragg gratings in slot waveguide,” *J. Biophotonics*, vol. 6, no. 10, pp. 821-828, 2013.
4. W. Shi, H. Yun, C. Lin, M. Greenburg, X. Wang, Y. Wang, S. T. Fard, J. Fluckekiger, N. A. F. Jaeger, and L. Chrostowski, “Ultra-compact, flat-top demultiplexer using anti-reflection contra-directional couplers for CWDM networks on silicon,” *Opt. Express*, vol. 21, no. 6, pp. 6733-6738, 2013.
 5. W. Shi, X. Wang, C. Lin, H. Yun, Y. Liu, T. Baehr-Jones, M. Hochberg, N. A. F. Jaeger, and L. Chrostowski, “Silicon photonic grating-assisted, contra-directional couplers,” *Opt. Express*, vol. 21, no. 3, pp. 3633-3650, 2013.
 6. X. Wang, W. Shi, H. Yun, S. Grist, N. A. F. Jaeger, and L. Chrostowski, “Narrow-band waveguide Bragg gratings on SOI wafers with CMOS-compatible fabrication process,” *Optics Express*, vol. 20, no. 14, pp. 15547-15558, 2012.
 7. W. Shi, X. Wang, W. Zhang, H. Yun, C. Lin, L. Chrostowski, and N. A. F. Jaeger, “Grating-coupled silicon microring resonators,” *Applied Physics Letters*, vol. 100, no. 12, pp. 121118, 2012.
 8. X. Wang and L. Chrostowski, “High-speed Q-modulation of injection-locked semiconductor lasers,” *IEEE Photonics Journal*, vol. 3, no. 5, pp. 936-945, 2011.
 9. W. Shi, X. Wang, W. Zhang, L. Chrostowski, and N. A. F. Jaeger, “Contra-directional couplers in silicon-on-insulator rib waveguides,” *Optics Letters*, vol. 36, no. 5, pp. 3999-4001, 2011.
 10. X. Wang, W. Shi, R. Vafaei, N. A. F. Jaeger, and L. Chrostowski, “Uniform and sampled Bragg gratings in SOI strip waveguides with sidewall corrugations,” *IEEE Photonics Technology Letters*, vol. 23, no. 5, pp. 290-292, 2011.

A.3 Conference Proceedings

1. L. Chrostowski, X. Wang, J. Flueckiger, Y. Wu, Y. Wang, and S. Talebi Fard, "Impact of fabrication non-uniformity on chip-scale silicon photonic integrated circuits," in *Optical Fiber Communication Conference*, San Francisco, CA, March 2014, paper Th2A.37.
2. M. Burla, L. R. Cortes, M. Li, X. Wang, L. Chrostowski, and J. Azana, "On-chip ultra-wideband microwave photonic phase shifter and true time delay line based on phase-shifted waveguide Bragg gratings," in *International Topical Meeting on Microwave Photonics (MWP)*, Alexandria, VA, October 2013, paper W2-3.
3. X. Wang, H. Yun, N. A. F. Jaeger, and L. Chrostowski, "Multi-period Bragg gratings in silicon waveguides," in *IEEE Photonics Conference 2013*, Bellevue, WA, September 2013, paper WD2.5.
4. M. Burla, M. Li, L. R. Cortes, X. Wang, L. Chrostowski, and J. Azana, "2.5 THz bandwidth on-chip photonic fractional Hilbert transformer based on a phase-shifted waveguide Bragg grating," in *IEEE Photonics Conference 2013*, Bellevue, WA, September 2013, paper WD2.2.
5. X. Wang, H. Yun, and L. Chrostowski, "Integrated Bragg gratings in spiral waveguides," in *CLEO 2013*, San Jose, CA, June 2013, paper CTh4F.8.
6. W. Shi, H. Yun, C. Lin, X. Wang, J. Flueckiger, N. Jaeger, and L. Chrostowski, "Silicon CWDM demultiplexers using contra-directional couplers," in *CLEO 2013*, San Jose, CA, June 2013, paper CTu3F.5.
7. Y. Wang, W. Shi, X. Wang, J. Flueckiger, H. Yun, N. A. F. Jaeger, and L. Chrostowski, "Fully etched grating coupler with low back reflection," in *SPIE Photonics North*, Ottawa, ON, June 2013, paper 89150U.
8. S. T. Fard, S. M. Grist, V. Donzella, S. A. Schmidt, J. Flueckiger, X. Wang, W. Shi, A. Millspaugh, M. Webb, D. M. Ratner, K. C. Cheung, and L. Chrostowski, "Label-free silicon photonic biosensors for use in clinical diagnos-

- tics,” in *SPIE Photonics West*, San Francisco, CA, February 2013, paper 862909.
9. X. Wang, W. Shi, M. Hochberg, K. Adams, E. Schelew, J. Young, N. A. F. Jaeger, and L. Chrostowski, “Lithography simulation for the fabrication of silicon photonic devices with deep-ultraviolet lithography,” in *Group IV Photonics*, San Diego, CA, August 2012, pp. 288-290.
 10. W. Shi, X. Wang, C. Lin, H. Yun, Y. Liu, T. Baehr-Jones, M. Hochberg, N. A. F. Jaeger, and L. Chrostowski, “Electrically tunable resonant filters in phase-shifted contra-directional couplers,” in *Group IV Photonics*, San Diego, CA, August 2012, pp. 78-80.
 11. W. Shi, M. Greenberg, X. Wang, Y. Wang, C. Lin, N. A. F. Jaeger, and L. Chrostowski, “Single-band add-drop filters using anti-reflection, contra-directional couplers,” in *Group IV Photonics*, San Diego, CA, August 2012, pp. 21-23.
 12. H. Yun, W. Shi, X. Wang, L. Chrostowski, and N. A. F. Jaeger, “Dumbbell microring reflector,” in *SPIE Photonics North*, Montreal, QC, June 2012, paper 8424-82.
 13. W. Shi, X. Wang, W. Zhang, H. Yun, N. A. F. Jaeger, and L. Chrostowski, “Integrated microring add-drop filters with contradirectional couplers,” in *Conference on Lasers and Electro-Optics*, San Jose, CA, May 2012, paper JW4A.91.
 14. W. Shi, X. Wang, H. Yun, W. Zhang, L. Chrostowski, and N. A. F. Jaeger, “Integrated silicon contradirectional couplers: modeling and experiment,” in *SPIE Photonics Europe*, Brussels, Belgium, April 2012, paper 8424-82.
 15. W. Shi, X. Wang, H. Yun, W. Zhang, L. Chrostowski, and N. A. F. Jaeger, “Add-drop filters in silicon grating-assisted asymmetric couplers,” in *Optical Fiber Communication Conference*, Los Angeles, CA, March 2012, paper OTh3D.3

16. L. Chrostowski, S. Grist, J. Flueckiger, W. Shi, X. Wang, E. Ouellet, H. Yun, M. Webb, B. Nie, Z. Liang, K. C. Cheung, S. A. Schmidt, D. M. Ratner, and N. A. F. Jaeger, "Silicon photonic resonator sensors and devices," in *SPIE Photonics West*, San Francisco, CA, Janurary 2012, paper 823620.
17. X. Wang, W. Shi, S. Grist, H. Yun, N. A. F. Jaeger, and L. Chrostowski, "Narrow-band transmission filter using phase-shifted Bragg gratings in SOI waveguide," in *IEEE Photonics Conference*, Arlington, VA, October 2011, pp. 869-870.
18. X. Wang, W. Shi, R. Vafaei, N. A. F. Jaeger, and L. Chrostowski, "Silicon-on-insulator Bragg gratings fabricated by deep UV lithography," in *Asia Communications and Photonics Conference*, Shanghai, China, December 2010, pp. 501-502.
19. X. Wang, B. Faraji, W. Hofmann, M.-C. Amann, and L. Chrostowski, "Interference effects on the frequency response of injection-locked VCSELs," in *IEEE International Semiconductor Laser Conference*, Kyoto, Japan, 2010, pp. 85-86.